Tissue Spectroscopic Characterization Based on Fluorescence, Second Harmonic Generation, and Reflected Light

By

Lily H. Laiho

B.S. Mechanical Engineering
Stanford University, 1995

M.S. Mechanical Engineering
Stanford University, 1996

Submitted to the Department of Mechanical Engineering in Partial Fulfillment of the Requirements for the Degree of

Doctor of Philosophy in Mechanical Engineering
at the
MASSACHUSETTS INSTITUTE OF TECHNOLOGY

September, 2004

© Massachusetts Institute of Technology
All Rights Reserved

Signatures of Author..
Department of Mechanical Engineering
September, 2004

Certified by.. ....
Peter T.C. So
Associate Professor Mechanical Engineering
Thesis Supervisor

Accepted by..
Ain A. Sonin
Chairman, Department Committee on Graduate Students

MASSACHUSETTS INSTITUTE
OF TECHNOLOGY
MAY 0 5 2005
LIBRARIES

BARKER

Tissue Spectroscopic Characterization Based on Fluorescence, Second Harmonic Generation, and Reflected Light

by
Lily Hsu Laiho

Submitted to the Department of Mechanical Engineering
on August 25, 2004 in partial fulfillment of the
requirements for the Degree of Doctor of Philosophy in
Mechanical Engineering

ABSTRACT

The diagnosis of many diseases often requires a histological analysis of tissues. Histology analysis compares the microscopic structure of a tissue specimen with an image database containing known physiological and pathological tissue structures. Three new microscopy technologies are developed to complement histology based on novel contrast mechanisms to better visualize and understand tissue structure and function: two-photon spectral resolved imaging, tri-modal imaging, and interferometric second harmonic imaging. First, two-photon spectral resolved microscopy utilizes the 3D localization ability of two-photon excitation to extract spectroscopic information from a femtoliter volume in tissue. The method is capable of the identification of biochemical species in tissues based on their morphological and spectral signatures. This system incorporates two new spectral analysis methods – spectral image guided analysis and multivariate curve resolution. This instrument has been applied to the study of human skin luminescence species and in a photoaging study of a skin equivalent model. Second, tri-modal microscopy combines two-photon fluorescence with second harmonic imaging and reflected light optical coherence microscopy. In this tri-modal system, fluorescence imaging maps fluorophore distribution; second harmonic imaging maps biological crystalline structures such as collagen and microtubules; reflected light optical coherence microscopy maps index of refraction heterogeneity. The ability of this tri-modal microscope has been demonstrated in the imaging of black tetra fish scale and in ex vivo human skin. Third, interferometric second harmonic microscopy has the potential for imaging deeper second harmonic active structures in tissues. This enhancement is based on phase coherent detection allowing the separation of multiple scattered light from the ballistic second harmonic signal. We have implemented interferometric second harmonic microscopy in epi-imaging mode and demonstrated coherent imaging of non-linear optical crystals.

Thesis Supervisor: Peter So

Title: Associate Professor of Mechanical Engineering

Table of Contents

List of Figures

Chapter 1

Introduction

This thesis describes the development of new technologies for non-invasive optical biopsy. Optical biopsy provides an alternative to traditional histopathological examination, which is the current clinical gold standard but is invasive. The development of non-invasive optical biopsy methods has the potential of improving patient care and lowering medical cost. In this thesis, I am developing imaging and spectroscopic optical biopsy techniques based on two-photon excitation, second harmonic generation, and reflected light to provide different contrast mechanisms to assay tissue structure and biochemistry. My thesis describes new spectroscopic methods for better identification of tissue endogenous luminescence species and new microscopic methods to map their distribution. Three instrument have been developed: a two-photon spectral resolved microscope, a tri-modal microscope incorporating two-photon fluorescence, second harmonic generation, and reflected light contrast mechanisms, and an interferometric second harmonic generation microscope. Preliminary demonstration of the capabilities of these instruments has been completed. The two-photon spectral resolved microscope has been applied to two studies: the identification of endogenous luminescence species in ex vivo human skin and the study of skin spectroscopic changes under UV irradiation using a skin equivalent model.

1.1 Motivation

The diagnosis of many diseases often requires a histological analysis of tissues. Histology analysis compares the microscopic structure of a tissue specimen with an image database containing known physiological and pathological tissue structures. As a complement to histology, new imaging modalities may be developed to non-invasively visualize and understand tissue formation, structure, and function. Optical biopsy is one of the non-invasive approaches based on the interaction of light with tissue that can obtain tissue morphological and biochemical information without the need for tissue excision and processing. Optical biopsy can complement traditional histology by allowing more informed selection of excisional biopsy sites. Typically the site for biopsy is determined by a visual inspection of the area of interest, which is based on differences in tissue surface coloring and texture. Typical biopsy involves only sampling minute volumes in order to limit the amount of tissue removed from the patient. This sparse sampling can limit the efficiency in which one can screen for disease. This difficulty in determining the optimal location for biopsy can lead to the need of follow-up excisional biopsies and may incur the risk of under diagnosis. The minimally invasive nature of optical biopsy allows many more sites to be sampled without tissue morbidity. While optical biopsy may not be able to provide as definitive a diagnosis as excisional biopsy, it allows the selection of excisional biopsy sites based on actual tissue structure and/or biochemical information. This is a significant improvement over random site biopsy. Another area of application of optical biopsy would be in the assistance of tumor removal procedures such as Mohs surgery. An optical biopsy could assist in the determination of margins of the tissue before removal. This would minimize the excess tissue removed and increase the chance that the entire lesion is eliminated. Finally, optical biopsy, given its minimally invasive nature, can lead to early diagnosis of disease. In summary, the benefits of optical biopsy are to improve traditional biopsy and surgery procedures, to provide a more accurate diagnosis of the tissue, and to reduce medical cost.

1.2 Objectives

1.2.1 Two-photon spectral resolved microscopy

Fluorescence spectroscopy has been used extensively to study the pathological state of tissues. Differences in the spectroscopic signatures can be used to differentiate between normal and pathological tissues. These differences may result from a change in tissue scattering due to a change in tissue morphology, a change in tissue absorption due to a change in the distribution and concentration of tissue absorbers, such as hemoglobin, or a change in the distribution and concentration of endogenous fluorescence species such as NAD(P)H. By studying these differences, researchers may detect diseases in their earlier stages.

Today, most tissue fluorescence spectroscopic measurement samples the overall spectrum from a macroscopic sample volume. This spectrum is a mixture of the different fluorophores present in the tissue, and it can be difficult to interpret the spectrum as it is not trivial to decompose the "mixed" spectra into individual biochemical components. In addition, the spectral differences between normal and diseased tissue is often small, and site-to-site and person-to-person variations due to tissue morphological differences often overwhelm the underlying spectroscopic differences. These morphological variations have been a major obstacle in applying fluorescence spectroscopy for definitive clinical diagnosis of tissue pathology.

To address these limitations, we use two-photon spectral resolved microscopy to extract spectroscopic information from microscopic volumes in tissue. The localization of the sampling region to femtoliter volume ensures the presence of few fluorophore species and allows easier identification of the biochemical species contributing to the overall spectrum. We have further developed new analysis methods to extract the spectrum of individual biochemical components. We applied this method to identify autofluorescence species present in ex vivo human skin and to study photoaging in skin equivalent models.

1.2.2 Development of tri-modal microscope instrumentation

From the work on two-photon tissue spectroscopy, it is apparent that both fluorescence and second harmonic generation are important and both can provide good contrast mechanisms with which to study tissue. In addition, it has been shown that reflected light from samples can be used to study tissue morphology based on structures that have index of refraction differences. The combination of these three contrast mechanisms into a single instrument that can perform simultaneous detection of the three processes provides powerful complementary morphological and spectral information. This tri-modal microscope combines two-photon microscopy with second harmonic generation microscopy and optical coherence microscopy. Initial demonstration of this system has been performed on black tetra fish scale and ex vivo human skin.

1.2.3. Interferometric second harmonic generation microscopy

In spectroscopic resolved tissue studies, it has been determined that there is often a strong second harmonic signal due to collagen in the extracellular matrix. Realizing that second harmonic signal is coherent, it is possible to develop a new instrument that can potentially extend the imaging depth for collagen distribution based on coherent heterodyne detection techniques similar to optical coherence tomography. The main goal of this instrument is to demonstrate the feasibility of microscopic imaging based on coherent detection of second harmonic light. We have implemented an interferometric second harmonic generation microscope in an epi-detection mode. Coherent imaging of this instrumentation is validated by imaging barium borate crystals.

1.3 Outline

This thesis is divided into eight chapters:

Chapter 1 – Introduction

Chapter 2 – Background: This chapter provides background information about histology, the gold standard of clinical tissue diagnosis. The interactions of light with tissue are discussed. In addition, this chapter also introduces the three different contrast mechanisms: fluorescence, reflected light, and second harmonic generation. A review of literature on the imaging techniques to detect these contrast mechanisms is presented. The techniques that are described are fluorescence spectroscopy and microscopy, confocal microscopy, two-photon microscopy, optical ranging, low coherence interferometry, optical coherence tomography, optical coherence microscopy, and second harmonic generation microscopy. Previous work in each of these areas is detailed.

Chapter 3 – Instrumentation and analysis methods: This chapter discusses the three different instruments that were developed in this thesis. The first is two-photon spectral-resolved microscopy. In addition to a description of the instrumentation hardware, we describe two different analysis methods developed – image guided spectral analysis and multivariate curve resolution. The second instrument described is a tri-modal microscope incorporating two-photon microscopy, second harmonic generation microscopy, and optical coherence microscopy. The third instrument described introduces a microscope capable of interferometric detection of second harmonic generation.

Chapter 4 – Sample preparation: This chapter describes the samples used in these studies and their preparation. The samples include ex vivo human skin, skin equivalent tissue constructs, fluorescent microspheres, black tetra fish scales, and barium borate crystals.

Chapter 5 – Two-photon spectral resolved microscopy results: We describe three different experiments. The first section describes experiments performed on ex vivo human skin by varying the excitation wavelength and extracting the endogenous species using multivariate curve resolution. The second section describes experiments performed on ex vivo human skin by studying the emission spectrum from different depth and also structures within the tissue. In these experiments, image guided spectral analysis was performed. The third section describes photoaging experiments performed on a skin equivalent model.

Chapter 6 – Tri-modal microscopy results: We describe the validation of the use of tri-modal microscope in the study of fluorescent microspheres, black tetra fish scale, and ex vivo human skin.

Chapter 7 – Interferometric second harmonic generation microscopy results: We demonstrated that coherent imaging with second harmonic signal is possible in barium borate optical crystals. We also demonstrated that polarization resolved imaging of coherent second harmonic signal may further provide crystal subdomain orientation information.

Chapter 8 – Conclusions: The accomplishments achieved in this thesis research are summarized and future directions and areas of application are discussed.

Chapter 2

Background

2.1 Overview

Optical biopsy provides an alternative to traditional histopathological examination, which is the current clinical gold standard but is invasive. The development of non-invasive optical biopsy has the potential of improving patient care and lowering medical cost. Optical biopsy may allow for earlier disease detection and more accurate diagnosis resulting in more effective therapy and increased survival rates.

This chapter discusses non-invasive optical microscopic techniques based on three contrast mechanisms: fluorescence, reflected light, and second harmonic generation. The basic histopathology approach is reviewed. Subsequently, we cover the basic light tissue interactions. Finally, we will describe the basic principles of fluorescence 3D microscopy, optical coherence microscopy, and second harmonic microscopy.

2.2 Histology

The diagnosis of many diseases often requires a histopathological analysis of tissues. Histology analysis compares the microscopic structure of a tissue specimen with an image database containing known physiological and pathological tissue structures. In order to obtain the tissue to be studied, a procedure called a biopsy is performed in which a sample of tissue from a patient is surgically removed for histopathological examination. An extensive tissue preparation procedure is required prior to microscopic examination of the excised tissue. The tissue first has to be treated with fixative such as Paraformaldehyde or formalin, to cross link protein structure and to prevent decomposition. The sample is subsequently either frozen or embedded in paraffin to facilitate slicing into sections using a microtome. Typical histological sections are between 1 – 150 microns thick[1]. The sections can then be stained for the particular biochemical species of interest and mounted on a glass slide in order to be viewed through a microscope. The resolution of histological examination is on the order of 1 micron.

Histology is the current clinical diagnosis procedure used to detect and diagnose most tissue diseases. Although it is the clinical gold standard, there are some limitations with this technique. One obvious drawback is that histology requires an invasive biopsy procedure where the sample is physically removed from the tissue to be examined. It is sometimes difficult to determine the optimal location for biopsy. This limits the sensitivity of disease detection because it can only sample a small volume to minimize tissue morbidity. Histopathology is also used to determine surgical margin in procedures such as tumor removal. Histopathological analysis is further needed to ensure the tumor mass and its extensions are eliminated. Traditional excisional biopsy and histopathological analysis is slow, labor intensive, and often cannot cover the whole perimeter of the surgical wound. Another limitation is that histology also requires preparation of the tissue through fixation and staining of the tissue where some tissue biochemical and metabolic information are lost. These shortcomings can limit the efficiency of histology in providing rapid, cost-effective diagnosis of disease.

2.3 Light-tissue interactions

When a photon enters a tissue, it can interact with the tissue's constituents by either absorption or scattering, Figure 2.1. In the first process, light goes into the tissue and the tissue constituents can absorb the incident light. When absorption occurs, energy is typically dissipated as heat. In the presence of fluorophores, instead of being dissipated as heat, the absorbed energy can also be re-emitted as light. In fluorescence emission, light is emitted at a lower energy corresponding to a longer wavelength, since energy is inversely proportional to wavelength.

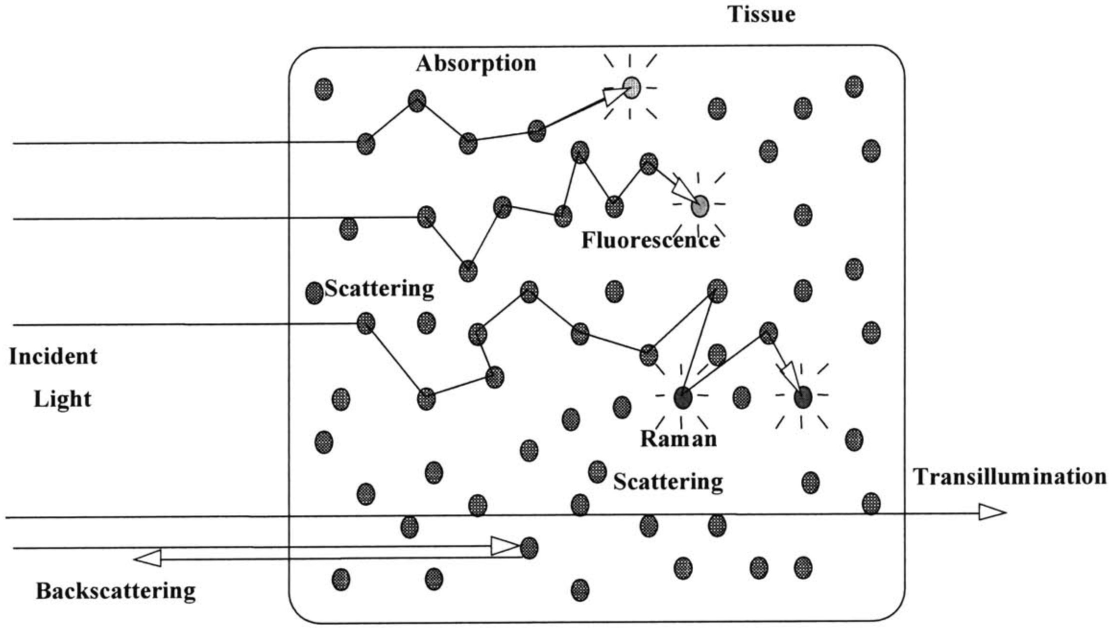

Figure 2.1. Interactions of light with tissue.

Another interaction of a photon with tissue is known as scattering. A photon can be scattered by changing its direction of travel without any changes in its energy or wavelength, this is known as Rayleigh scattering. Rayleigh scattering is an elastic process. If the light is inelastically scattered due to vibrations in a molecule, it is known as Raman scattering. Other non-linear scattering processes can also occur when the electric field amplitude of the incident light is very high. For example, second harmonic generation is produced where the scattering of two incident photons results in the generation of a single emitted photon with twice the energy at half the wavelength.

Light-tissue interaction can also be studied in two geometries. In the transillumination geometry, interaction is studied by examining light that has passed through the tissue. Light-tissue interaction can also be studied in the epi-geometry in which light emission in the backward direction of the incident light is studied.

In this chapter, we will review three specific light-tissue interactions that are used for tissue imaging in this work: fluorescence, reflected light, and second harmonic generation.

2.4 Fluorescence

2.4.1 Overview

Fluorescence is a process where molecules absorb light at a particular wavelength and emit light at a longer wavelength. More specifically, molecules are normally found at the lowest electronic energy state, which is the ground state. In the case of one-photon fluorescence excitation, when an incident photon interacts with a molecule electronically, an electron can absorb the photon energy and climb to a higher energy state. The electrons may subsequently dissipate some energy via vibrational relaxation to the lowest vibrational level of the first electronic state. The electron that returns to the ground state can be through either radiative (fluorescence) or non-radiative processes. The time it takes for the molecule to return to the ground state is known as the fluorescence lifetime of the molecule. Since some of the energy of the incident photon is always dissipated vibrationally, the emitted photon has lower energy than the incident photon. This corresponds to light emitted at a higher wavelength since energy is inversely proportional to wavelength. The Jablonski diagram, as seen in Figure 2.2 encapsulates these processes. The wavelength of both the absorbed and emitted energy is characteristic of the fluorophore, and the spectral intensity distribution is a signature of the molecule related to the quantum mechanical wave function overlap between various excited and ground vibrational states. The total fluorescence intensity is a function of both the fluorophore's intrinsic quantum yield and its concentration in the specimen..

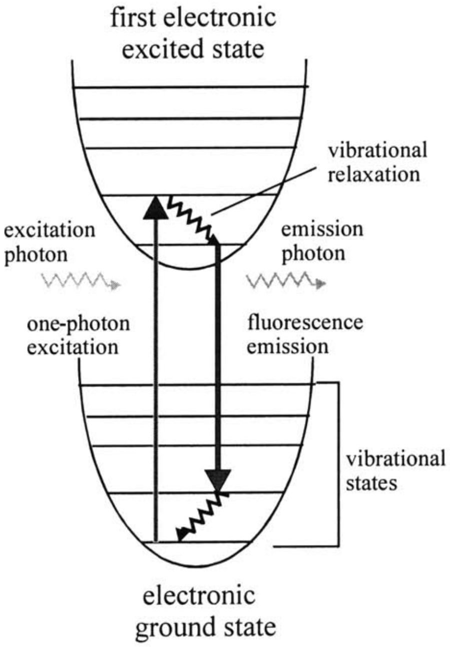

Figure 2.2. Jablonski diagram showing one-photon excitation[2].

2.4.2 Fluorescence microscopy and spectroscopy

Fluorescence microscopy is often used to study living cells and tissues. A polychromatic light source is often used, such as either mercury or xenon arc lamps. These sources produce high-intensity illumination over a broad spectrum. Using a narrow band excitation filter, a selected portion of the emitted light can be used to excite a specific fluorescent species. The emitted fluorescent light is at longer wavelengths than the incident light. The depth of field for a typical fluorescence microscope is approximately 2 – 3 microns[3] and does not have true depth discrimination. Fluorescence microscopy can be used to study both native autofluorescence and also fluorescent labeled molecules.

Endogenous fluorophores are responsible for tissue autofluorescence. Microscopic imaging of autofluorescence can provide useful tissue structural and biochemical information without fixation and staining procedures offering the opportunity to develop non-invasive optical biopsy based on fluorescence contrast.

In addition to structural imaging of tissue, fluorescence spectroscopy provides complementary tissue functional information. Tissue spectroscopy is a powerful method to identify endogenous fluorescence species. The relative abundance of these species is related to tissue physiological and pathological states. Fluorescence spectroscopy has been used to characterize different tissue types such as colon, lung, cervix, and skin[4,5]. It has been used to study normal and malignant laryngeal tissue[6], cervical tissue[7,8,9], oral tissue[10],[11], colonic mucosa[12], epithelial precancerous changes[13], lung cancer[14], skin cancer[15], head and neck cancer[16], in addition to other areas.

In addition to tissue type characterization, spectroscopy has been used to monitor the physiological state of a tissue[17,18,19]. The differences in tissue excitation spectra have been used for disease diagnosis such as distinguishing between malignant and normal tissues[20,21,22,23]. Tissue spectroscopy has also been used to study the effects of aging and photoaging[24].

2.4.3. Confocal microscopy

Confocal microscopy is a three-dimensional imaging technique that enables high resolution, depth-resolved imaging of biological samples. Light from a laser is focused into a specimen through a microscope objective and is scanned across the sample via mechanical scanners. Both reflected light and fluorescence can be generated using this method and is often detected in epi-geometry. The reflected light or fluorescence comes back from the sample and is separated from the incident light by a dichroic mirror. The beam is "de-scanned" when it retraces its path through the mechanical scanners. A pinhole aperture is placed in a conjugate position of the object plane. Light that comes from the focal plane from within the specimen goes through the pinhole. Light that is out of focus or is multiple scattered does not make it through the pinhole and is thus rejected. Detection of both the reflected light and/or fluorescence is often achieved through the use of a photomultiplier. By placing different filters in front of the photomultiplier, specific wavelength ranges can be studied. This gives rise to several advantages that confocal microscopy has over conventional fluorescence microscopy. As this system creates a diffraction limited spot with the objective, it can achieve higher resolution than conventionally. The resolution is typically on the order of 0.15 to 0.30 microns laterally and 0.50 to 1.0 microns axially[25]. It allows for optical sectioning of thick samples that are larger than the focus plane. In addition, out of focus light is rejected and there is true 3D resolution. One disadvantage is that there can be increased photobleaching in confocal microscopy due to the higher excitation energy needed to image the fluorescence as confocal microscopy only collects a portion of the total fluorescence.

The methodology of confocal microscopy is well established, and this technique has been used to study a large number of applications. In addition to extensive work in cell biology, tissue specimens have been studied. Notably, work has been done in oral tissue[26], skin[27], normal and precancerous cervical tissue[28], normal and malignant colonic tissue[29], and bladder[30].

2.4.4 Two-photon microscopy

Another way to obtain 3D resolved fluorescence imaging is through the use of two-photon microscopy, which is similar to confocal fluorescence microscopy. The principles for two-photon excitation were developed by Maria Goppert-Mayer[31]. Two-photon excitation occurs when an electron is excited to a higher energy electronic state by the simultaneous absorption of two photons in the infrared wavelength. The two photons have half the energy of the single photon necessary in conventional fluorescence imaging. In this case, two photons can be simultaneously absorbed at high photon densities by combining their energies to excite the molecule to the excited state. Because the energy of a photon is inversely proportional to its wavelength, the two photons should have a wavelength about twice that is required for single-photon excitation. When the excited electron returns to the ground state, it emits a single fluorescence photon. This means that longer wavelengths in the infrared region can be used to excite these molecules, Figure 2.3.

Since the cross-section of two-photon processes is significantly less than in the one-photon case and the two-photon fluorescence has a quadratic dependence upon excitation power, the two-photon excitation only takes place in a localized sub-femtoliter excitation volume at the focal point of an objective lens where there is a high concentration of photons. This localization of excitation provides depth discrimination and allows us to obtain three-dimensional images in a laser-scanning microscope system as was first demonstrated by Denk, et. al.[32]

Two-photon excitation has several important advantages over one-photon techniques, such as confocal microscopy, for the imaging tissue autofluorescence. Since fluorescence excitation only occurs in a small region, this reduces out-of-focus photodamage and photobleaching allowing the study of living specimens. Furthermore, tissue endogenous fluorophores have absorption in the ultraviolet (UV) spectral range. Since UV radiation is strongly absorbed and scattered by the tissue, UV microscopic imaging of tissue typically has a very short penetration depth. The use of two-photon methods allows the excitation of UV fluorophores in the infrared wavelength region where the tissue scattering and absorption of light are greatly reduced and tissue penetration depth is significantly enhanced. The depth discrimination created with two-photon excitation, allows for the generation of three-dimensional images through scanning. Two-photon excitation also simplifies experiments due to the large separation between the excitation and emission wavelengths. These strengths give rise to the increase in the use of two-photon microscopy for deep tissue imaging.

Two-photon microscopy has been applied to many different areas in biology and medicine. Several areas of particular interest are in studying tissue physiology, optical biopsy, and photodynamic therapy[33,34]. Notably, two-photon microscopy has been applied to studying human[35,36,37] and mouse[38] skin structures, neurobiology[39,40,41,42,43,44,45], in vitro skin equivalent models[46], normal and malignant breast cell lines[47], liver culture[48], engineered lung tissue[49], and embryonic tissue[50].

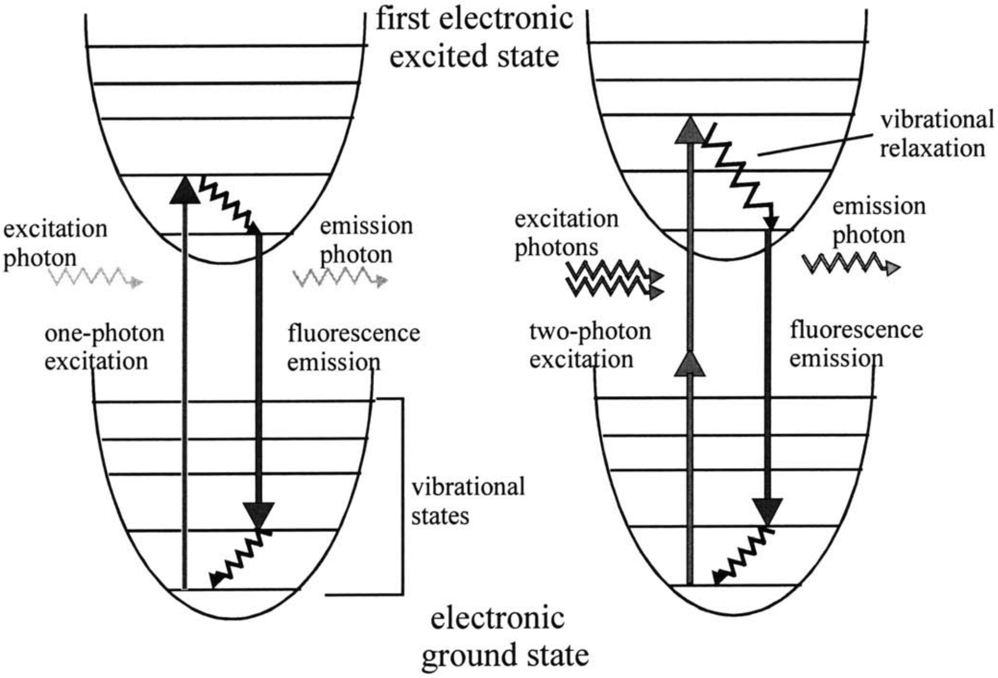

Figure 2.3. Jablonski diagram showing one-photon and two-photon excitation[2].

Wavelengths in the near-infrared are particularly attractive for deep tissue imaging. Figure 2.4 shows some of the components of human tissue and their absorption coefficients. The absorption coefficients of the different components are a function of wavelength. There is an "optical window" that exists in the 700 – 950 nm region in which the photon processes are dominated by scattering rather than absorption. In this region, human blood and tissue minimally absorbs. Thus, more fluorescence signal can be detected from a sample and photodamage is also minimized. Using near infrared light also allows for deeper penetration into the tissue due to less scattering. Light in this wavelength range has a scattering length on the order of a few hundred microns. Two-photon excitation, which uses infrared excitation, is very suitable for the study of tissue optical properties.

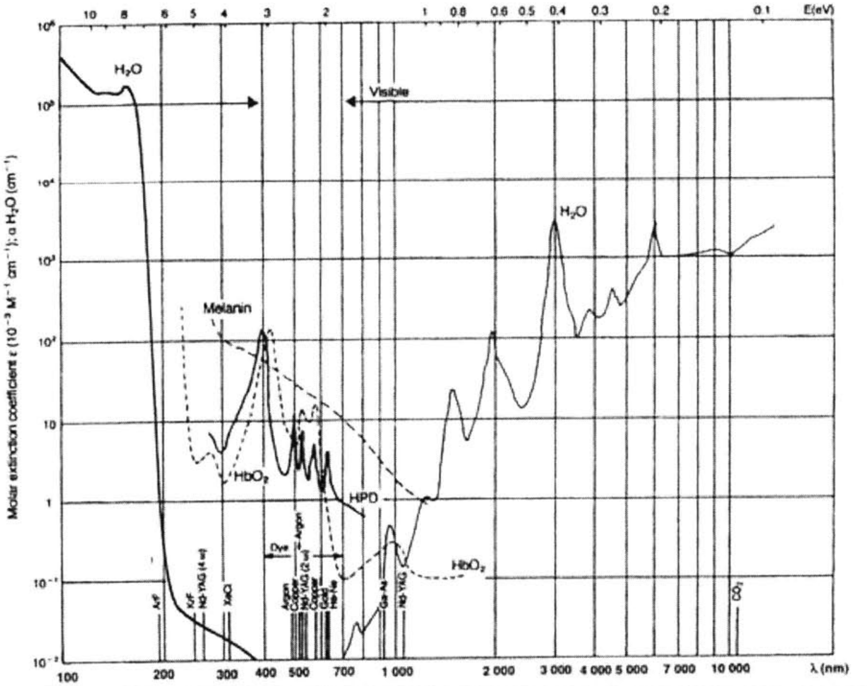

Figure 2.4. Optical window for tissues[51].

Two-photon microscopy can also be combined with spectroscopy in order to obtain additional information about the biochemical species present within tissue. The analysis of tissue spectroscopic information with 3-D microscopic resolution has major advantages compared with typical bulk tissue spectroscopy approaches[52,53,54]. Previous works often examine the overall spectrum from a macroscopic sample. This overall spectrum results from a mixture of many different fluorophores. The decomposition of this "mixed" spectra into individual components based on numerical methods such as principle component analysis is often a difficult task in complex tissues[55,56,57]. Performing spectroscopic analysis on two-photon microscopy data allows us to obtain structural information that provides additional a priori information for spectral decomposition. Specifically, 3-D resolved spectroscopy isolates fluorescence signal that originates from microscopic volumes that typically contain fewer independent fluorescent species. By reducing the mixing of different fluorescence species, the identity and distributions of each pure biochemical species can be more easily assayed. Spectroscopy information can be extracted from the entire volume, from a two-dimensional section, or even from a specific morphological structure in the sample.

2.5. Reflected Light Imaging

2.5.1. Optical Ranging

Reflected light is coherent. Optical ranging is one method that can be used to detect coherent signals. This is the optical analog to ultrasound. This method works by directing excitation light into an object and measuring the light reflected back from different structures within the sample. Different layers within a volume of tissue will give different optical reflections. The distance between these optical reflections can be measured by using a detector to measure the time delay between the arrivals of reflections from the different structures within the tissue, Figure 2.5. In order to achieve high resolution optical ranging, the detector measuring the delay of pulses has to be able to detect pulses with femtosecond resolution. This is because we are interested in obtaining depth resolution on the micron scale. The time between pulses is equal to the desired resolution divided by the speed of light. This translates into the time delay between these pulses being on the order of femtoseconds. Femtosecond electronic detectors are not technologically feasible; thus, another method is needed in order to measure this time delay. One way to do this is through the use of interferometric techniques.

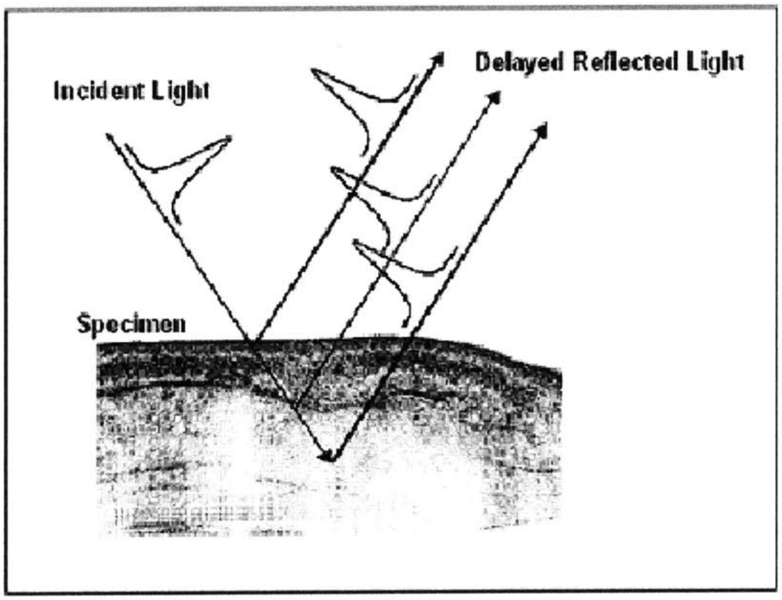

Figure 2.5. Optical ranging within tissue[58].

2.5.2. Low-coherence interferometry

Low-coherence interferometry is based on a Michelson interferometer in which the interferometer is illuminated using a low coherence source. The interferometer measures the time delay of pulses by interfering the light that is backscattered from a sample with light that has traveled a known reference path length and thus a known time delay. A schematic of this system can be seen in Figure 2.6.

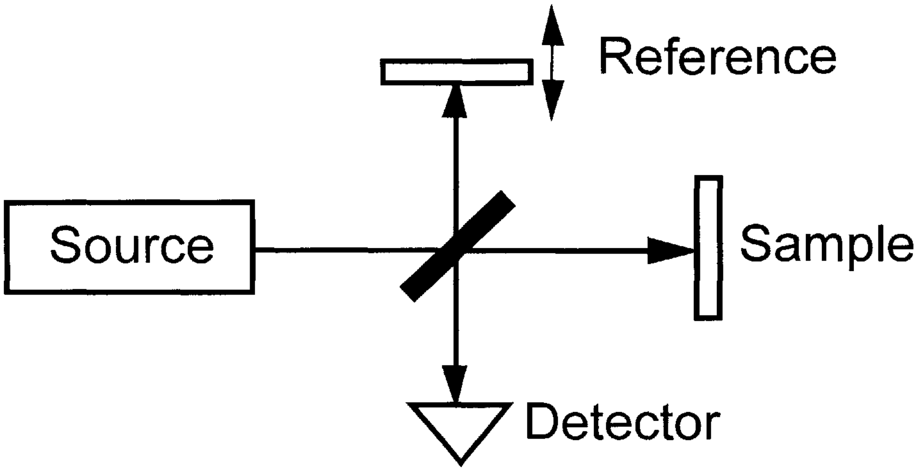

Figure 2.6. Schematic of a Michelson Interferometer

In this interferometer, the light from a source is divided into two paths by a beamsplitter. These two different paths can be referred to as the sample and reference arms. Light is retro-reflected from both the sample and the reference arms and is recombined by the same beamsplitter and directed into an optical detector. Interference is generated only if the distances the waves traveled along the two arms are approximately the same, and their path length difference is within the coherence length of the light source. The coherence length of a light source is the distance over which the phase of the light wave remains predictable. The coherence length can be described by the following equation:

$$l_c = \frac{2\ln 2}{\pi} \frac{\lambda_0^2}{\Delta\lambda}$$

where l_c is the coherence length of the source, λ_0 is the wavelength of the incident light, and $\Delta\lambda$ is the bandwidth of the light. A mirror is placed at the end of the reference arm, and the length of the reference arm can be adjusted by moving the reference mirror back and forth along the axis of the beam. As the reference mirror moves, the reference path length can lengthen and shorten to match the optical path length in the sample arm.

If the light source that is used is coherent with a narrow bandwidth, then the coherence length will be relatively long. Upon motion of the reference arm, the detector will detect an interference pattern even for large path length differences between the sample and reference arms, as seen in Figure 2.7.

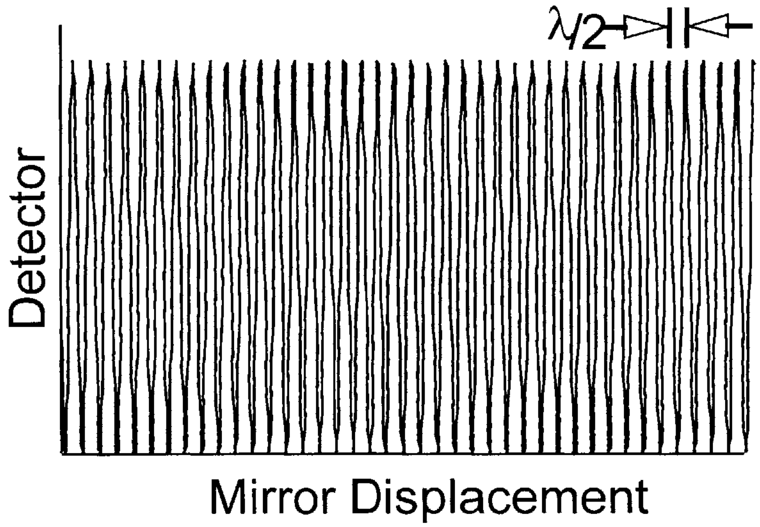

Figure 2.7. Detection of interference from a coherent light source.

However, for a low coherence length source in which the bandwidth is relatively large, the motion of the reference arm produces an interference pattern only when the path lengths of the interferometer arms are matched to within the coherence length of the source, as seen in Figure 2.8. This is referred to as a coherence gate. Light that is not coherent will be rejected, thus ignoring the contribution from fluorescence or out of focus light.

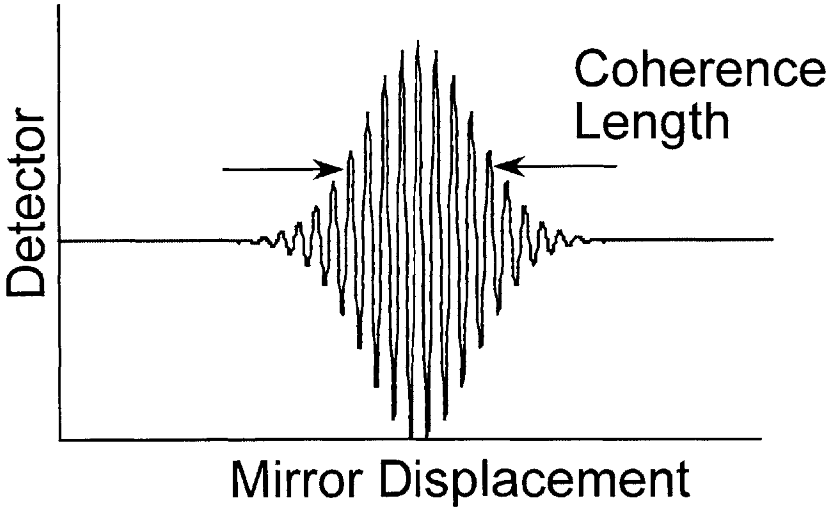

Figure 2.8. Detection of interference from a low-coherent light source.

The resulting detected interference does not have a constant amplitude as in the case of the long coherent length source. In the case of the low-coherence source, as the mirror moves back and forth, the interference comes in packets that will appear and disappear as the reference and sample arms go in and out of path length matching.

2.5.3. Optical coherence tomography

Low-coherence interferometry is the basis for an imaging technique called optical coherence tomography (OCT). OCT is a noninvasive structural imaging technique that produces high-resolution cross-sectional images in biological samples[59]. This system measures backscattered light from tissue by oscillating the mirror in the reference arm and looking for interference patterns. If a reflective interface in the sample arm is at the exact same distance as the path length in the reference arm, an interference pattern can be detected, Figure 2.9. In addition, the sample arm distance can be adjusted to focus on different depths within the sample, and the reference arm can be scanned accordingly. The reflectivity from different internal structures at different depths within a sample can be determined by studying the envelope of the interference fringes as a function of reference mirror displacement. The presence of an interference fringe pattern implies the presence of a reflective surface at a given depth. The amplitude of the interference packet is a measure of the reflectivity of the object. Optical ranging in combination of either beam or sample scanning can be used to create a sagittal image of the sample.

OCT makes use of coherence gating and gives way to 3D resolution because it rejects signal outside of the coherence gate. The resolution of OCT systems is typically a few microns in both the axial and lateral direction and is determined by the coherence length of the laser source and the low NA, long focal depth lens used for imaging. The low numerical aperture enables the system to have a larger field of view. OCT systems are reported to be capable of imaging depths of up to 1 - 2mm in skin[60,61] depending on the location. This is limited due to the scattering nature of tissue.

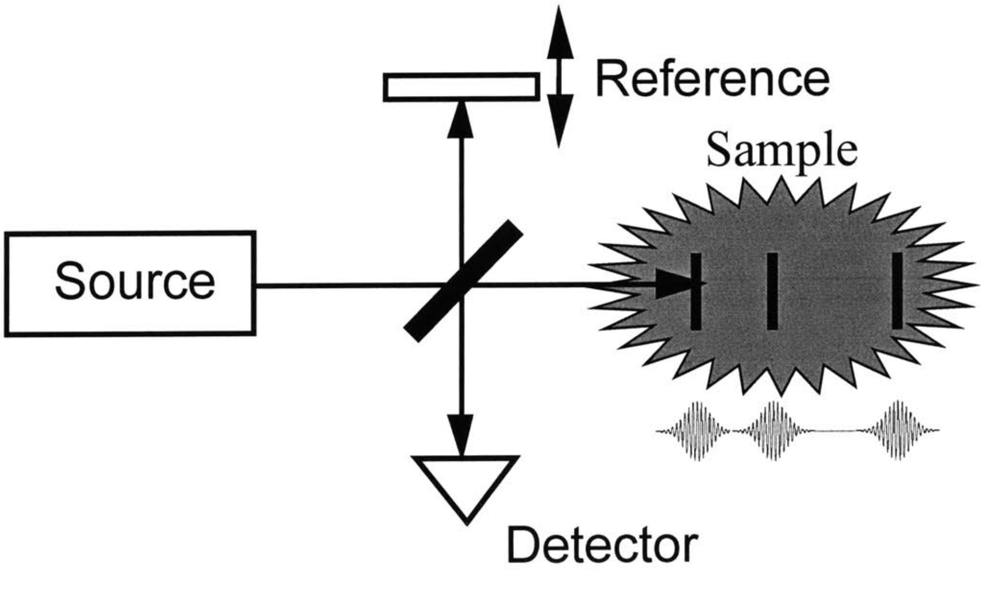

Figure 2.9. Schematic of OCT system.

Optical coherence tomography has been used in clinical studies already and has primarily been used to study the human eye[62,63.64,65,66,67] which has a low scattering medium. In addition, work has been done to study other areas such as skin[68,69,70], gastrointestinal tract [71,72], middle ear[73], prostate gland,[74] retinal flow dynamics[75], breast tissue[76], arterial tissue[77], gynecologic tissue[78].

2.5.4 Optical coherence microscopy

A very similar interferometric technique to OCT is optical coherence microscopy (OCM) that uses a high numerical aperture objective to improve lateral resolution while using coherence gating to obtain depth discrimination. OCM often incorporates a confocal pinhole in the detection path to take advantage of both coherence and confocal gating to reject out of focus light. To achieve the higher resolution of OCM (3 to 10 mm versus 10 to 30 mm), special effort is made to keep the focal plane of the beam coincident with the equal path length position of the OCM interferometer. Thus, the axial resolution is a product of the confocal and coherence point spread function. The point spread function of OCM, which is the impulse response of the system, drops off in a Gaussian manner far from the focal plane and much more rapidly than that of confocal microscopy[79], as seen in Figure 2.10. In OCM, scanning is performed en face, meaning in the x-y direction as with two-photon microscopy. OCM can be more difficult than OCT due to the x-y scanning. OCM has higher resolution due to the high numerical aperture focusing, but the tradeoff is that it requires interferometric stability thus preserving the lateral resolution throughout the depth of the sample.

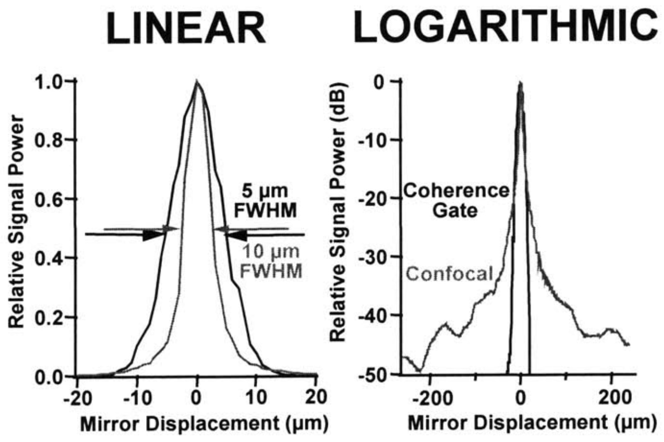

Figure 2.10. Confocal and coherence gate in optical coherence microscopy[79].

2.6. *Second harmonic imaging microscopy*

Second harmonic imaging microscopy is a powerful contrast mechanism that has been used to characterize surfaces and interfaces and has recently been used as a contrast mechanism to study cell and tissue physiology and functions. Second harmonic imaging microscopy studies the second harmonic generation (SHG) that is generated from a specimen using intense laser light. The second harmonic signal is the scattered light that occurs at exactly twice the incident frequency, which is half the incident wavelength. Using high intensity radiation, SHG results from an induced nonlinear polarization and requires a non-centrosymmetric medium. The basic principles of SHG will be covered in the following section. Biological structures that produce significant SHG include collagen, muscle myosin, and microtubules[80].

The same conditions that generate two-photon excitation also give rise to second harmonic generation. However, two-photon excitation is an absorption process while second harmonic generation is a scattering process. The setup for this type of microscopy is similar to the setup for two-photon microscopy except that it requires a different filter set before the detectors. Recently, second harmonic imaging microscopy has been used to study skin[81,82,83], endogenous structural proteins in tissue[84], living cells[85], collagen[86,87,88,89,90], membrane potentials[91,92,93], and lipid bilayers[94,95].

2.6.1. Second harmonic generation basic principles

Second harmonic generation is a second order nonlinear optical process, which can be represented by the following equation, which describes the nonlinear polarization of a material

$$P = \chi^{(1)}E^1 + \chi^{(2)}E^2 + \chi^{(3)}E^3 + \ldots..$$

where P is the induced polarization for a material, $\chi^{(n)}$ is the nth order nonlinear susceptibility and is a material property, and E is the electric field vector. The first term describes the normal absorption and reflectance of light. The second term describes the second harmonic generation process, and the third term describes processes such as two-photon excitation, third harmonic generation, and light scattering Raman processes. Normally, the higher order susceptibilities are pretty small, thus their effects are negligible. However, under the illumination of ultra-fast lasers with high electric field strength, their effects are no longer negligible and one can detect these non-linear processes.

In second harmonic generation, there is a coherent scattering of light that is twice the incident frequency. Second harmonic generation is a scattering process unlike two-photon excitation, which is an absorption process and produces incoherent light. The scattering is virtually instantaneous, so the phases of the excitation and emission photons are in phase and coherent. This means that there is a known phase relationship relative to the incident light, and the resulting light is a coherent sum of the scattering.

To better understand this process, we can start by looking at this process at the molecular level. The discussion in this section is based on Dr. Jerome Mertz's website (Department of Physics, Boston University). In the case of a symmetric molecule, when the molecule is excited sinusoidally by light at frequency ω, the resulting light will be generated at frequency ω. This process in which the excitation and emission light are at the same frequency, which is known as Rayleigh scattering, Figure 2.11.

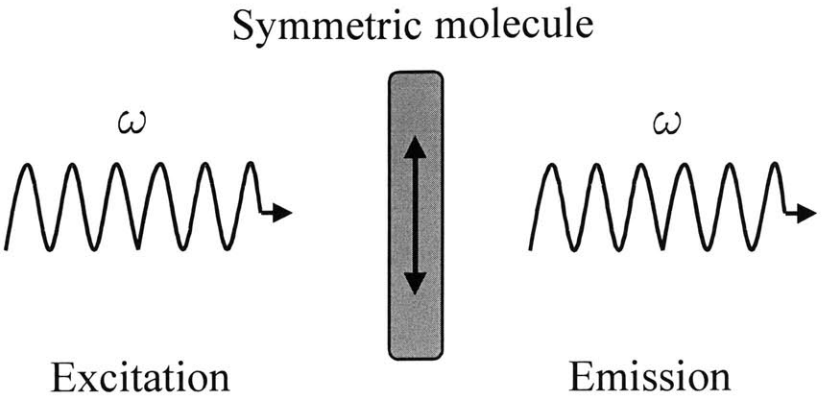

Figure 2.11. Rayleigh Scattering

For an asymmetric molecule, when the molecule is excited by the same excitation light, the motion of its electronic cloud is not symmetric and contains frequency components at both ω.and 2ω, Figure 2.12. The 2ω frequency component is called hyper-Rayleigh scattering (HRS). This is the radiation that comprises second harmonic generation.

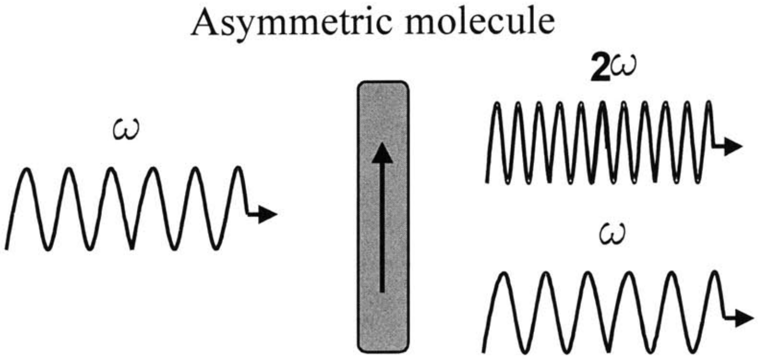

Figure 2.12. Hyper-Rayleigh scattering.

The emission intensity depends on the orientation of the molecules. This is illustrated in Figure 2.13. In the first case, there are two asymmetric molecules that are located closely together and are separated by a distance that is much smaller than an optical wavelength. The two molecules are oriented in the same direction and are parallel to one another. When these molecules are excited the resultant HRS from both molecules will be in phase and constructive interference results. Their amplitude will be doubled which means that the net power will be quadrupled compared to power obtained from a single molecule as it is a non-linear process.

If the two molecules are oriented in opposite directions then there is a very different result. This means that their respective HRS amplitudes are out-of-phase and exactly cancel. Thus, there is destructive interference. The net power produced by the molecules is zero. In this case, the molecules are effectively symmetric.

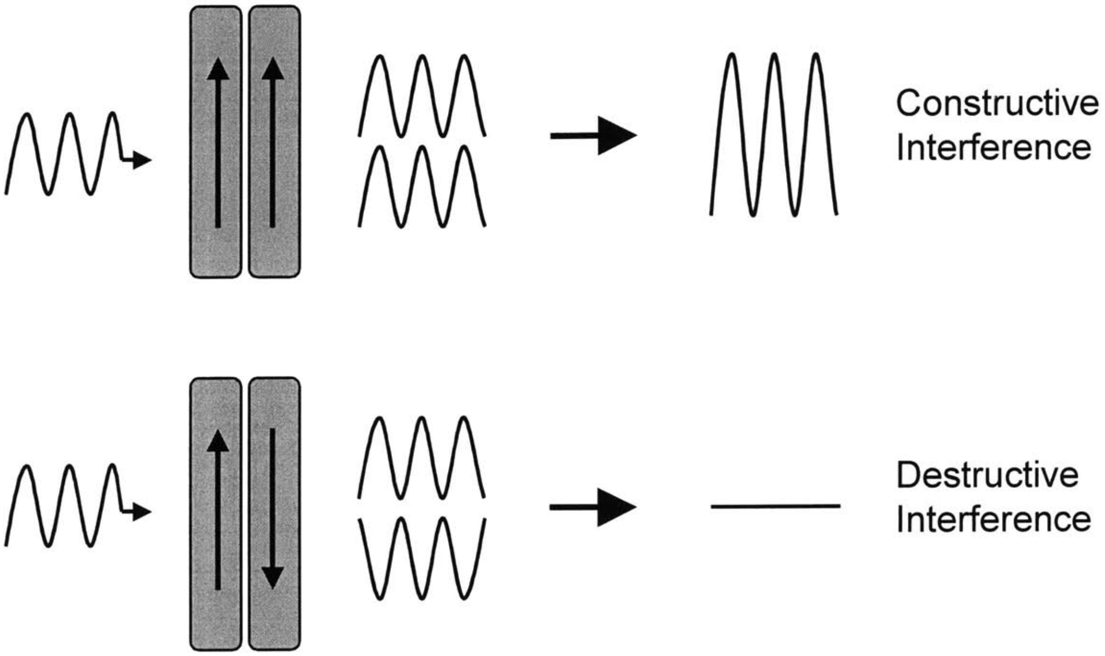

Figure 2.13. Orientation and interference dependence of emission intensity

In second harmonic imaging microscopy, we are interested in looking at not just two molecules but an entire population of molecules, Figure 2.14. Look at this first configuration where there are N number of molecules in solution. In this case, the orientations of the molecules are random. This means that the phases of their individual HRS signals are also random, and the signal is incoherent. In this case, the total power is proportional to the number of molecules, and this is the same scaling law that applies to fluorescence.

In the case where the molecules are aligned along the same direction, the phases of the emission signal from each molecule are no longer random and are in phase with one another. This creates a coherent signal and is known as second harmonic generation. Second harmonic generation is the coherent summation of the HRS light. The total SHG power is proportional to the number of radiating molecules squared.

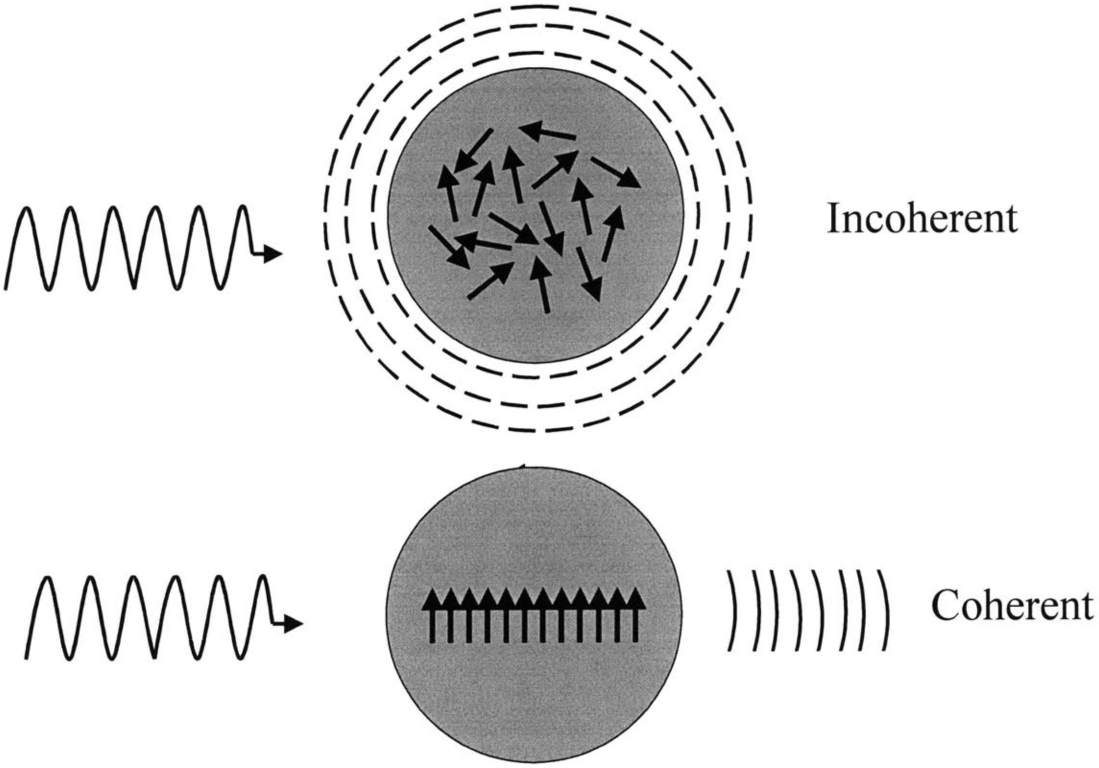

Figure 2.14. Incoherent and coherent summation of hyper-Rayleigh scattering.

They are several advantages to studying second harmonic generation. As mentioned previously, second harmonic generation requires non-linear optical interaction of the sample with high intensity excitation. Therefore, SHG image has the same 3D resolution as two-photon microscopy. In fact, SHG and two-photon fluorescence are often observed simultaneously in the same instrument. Similar to two-photon microscopy, out-of-plane photo-interaction is greatly reduced. Unlike two-photon microscopy, in-plane photobleaching and photodamage do not result from second harmonic generation, which is a scattering process with no energy absorption. In addition, SHG propagates along the same direction as the incident field. Because of this directionality, the signal can be collected more efficiently. Another advantage is that matching of the excitation wavelength of a fluorophore is not necessary as the emission wavelength is always exactly half the excitation wavelength. Finally, the second harmonic signal is coherent and this provides an opportunity for using coherent gating to reject out of focal plane signal.

Chapter 3

Instrumentation and spectral analysis algorithms

3.1 Instrumentation

3.1.1 Two-photon spectral resolved microscopy

A schematic of a typical two-photon scanning instrumentation that was used in these experiments is shown in Figure 3.1. A femtosecond mode-locked Ti:Sapphire laser (Tsunami, Spectra Physics, Palo Alto, CA) generates the excitation light. This Ti:Sapphire laser features a broad-spectrum mirror set that allow the system to be conveniently tuned from 690 to 1000 nm. A galvanometer-driven x-y scanner (Cambridge Technology, Watertown, MA) is used to scan the beam through the objective and across the sample generating 256 x 256 pixel images. The light enters a Zeiss Axiovert 110 microscope (Zeiss Inc., Thornwood, NY) and is reflected into the objective through a dichroic mirror (Chroma, Brattleboro, VT). A piezoelectric objective translator (Physik Instrumente, Waldbronn, Germany) moves the objective in the z-direction allowing for imaging at different depths. The fluorescence signal is collected by a photomultiplier tube (R7400P, Hamamatsu Corporation, Bridgewater, NJ) at each pixel, and a computer collects information about the number of photons at each pixel. Customized software is used to generate three-dimensional images.

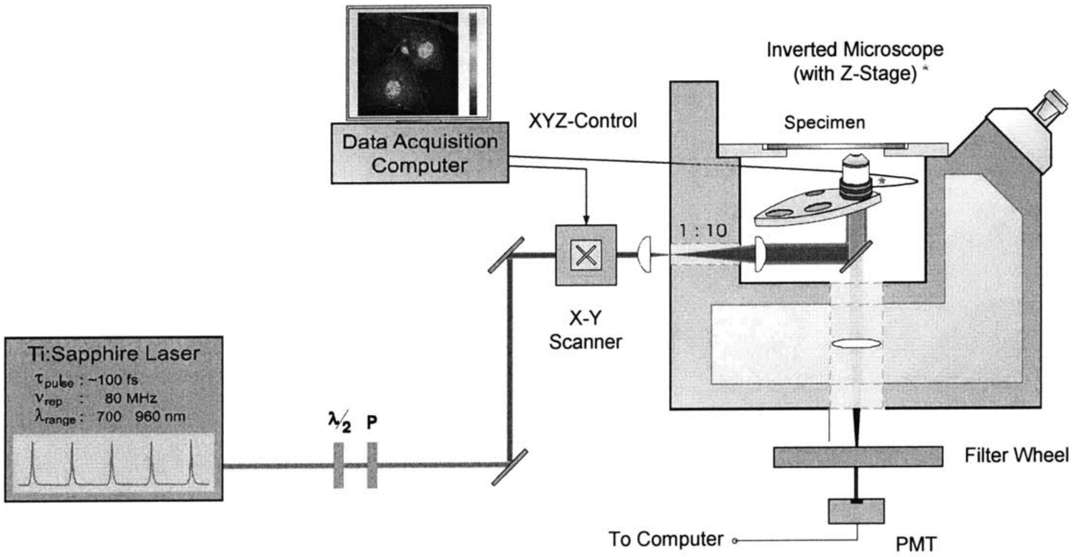

Figure 3.1. Schematic of two-photon scanning microscope[96].

3.1.1.1. Excitation and emission spectroscopy devices

Spectroscopy involves the collection and analysis of a spectrum. This is typically done by the insertion of a dispersive element into a path of light that will separate the light into its components wavelengths, and these wavelengths can then be sensed using a detector. Different devices can be used in conjunction with two-photon instrumentation in order to generate the emission spectra of a specimen. The following are several different devices that have been implemented with the two-photon microscope in this thesis to generate emission spectra.

3.1.1.1.1. Filter wheel

A filter wheel is a mechanical device with moving parts that contains a number of bandpass filters within it, as seen in Figure 3.2. These filters are rotated around the center of the filter wheel and are mechanically indexed for precise positioning. A filter wheel was designed and implemented into the microscope. The filter wheel was inserted at the microscope's bottom detection port. The filter wheel can rotate, and the filter of choice is placed in front of the PMT. The filters range from 400 to 625 nm in 25 nm increments. The bandwidth of each bandpass filter (Chroma, Brattleboro, VT) is approximately +/-10 nm, although the bandpass shape is slightly different for each filter. The efficiency of each filter is on average 80%. In order to create the emission spectrum, an image is taken through a single filter in front of the PMT in the beam path. Then the filter wheel is rotated and an image is taken through the next filter, etc. In this case, most of the out-of-band emitted light is rejected and wasted since only a small portion is actually collected. Although the efficiency of each filter is quite high, this is a slow technique due to the low light collection efficiency. Further, there is significant temporal delay in stepping the filter wheel sequentially that is on the order of seconds. However, this problem can be circumvented in the future by motorizing the filter wheel. Typically the scanning rate of a 256 x 256 pixel section containing tissue autofluorescence using the filter wheel is 5kHz, which is approximately 14 seconds per each frame. The time to obtain an entire emission spectrum for a single 2-dimensional image is approximately 158 seconds, including the time to index the filter wheel.

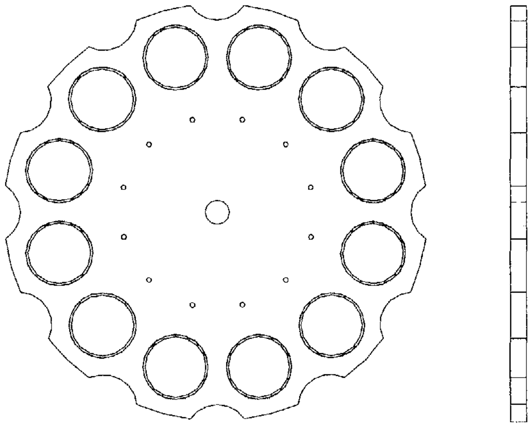

Figure 3.2. Schematic of filter wheel

3.1.1.1.2. Liquid crystal tunable filter

Another sequential spectroscopic device is a liquid crystal tunable filter (LCTF). A LCTF is a type of bandpass filter that can be quickly tuned through in order to create a sequence of wavelengths[97,98] and generate a spectrum. This allows for sequential emission wavelength scanning of images. The switching of filters is done on the order of milliseconds. A LCTF consists of a birefringent liquid crystal sandwiched between polarizers and waveplates. The retardance of the liquid crystal solution can be adjusted electronically to tune the pass band of the device. The liquid crystal tunable filter can be placed directly in front of the PMT as with the filter wheel. Some advantages to the LCTF are that it does not have any moving parts, and switching time is relatively quick. However, the transmission efficiency of these filters is approximately 40% across the VIS and near-IR spectral range but can be as low as a few percent in the near-UV range[96]. We have tested a state-of-the-art LCTF (CRI, Woburn, MA) for skin imaging. Due to the low efficiency of the filters, each image of skin autofluorescence was summed over 5 repetitive scans in order to increase the number of photons detected. This is approximately 70 seconds per each frame, and the time to take an entire emission spectrum for a single image is approximately 700 seconds, ignoring the time to switch to different emission wavelengths. It was determined that due to this slow data acquisition time, the liquid crystal tunable filter was not a viable option for studying autofluorescence in tissue.

3.1.1.1.3. Spectrograph with Multi-Anode PMT

Another device that can allow for the study of spectrum is a spectrograph. A spectrograph is a device that separates the different wavelengths of light in order to create a spectrum. This is done through the use of a grating, which is a system of parallel lines or grooves on a polished surface that create a spectrum through diffraction. The input is a single beam while the output is an entire spectrum. The spectral resolution of gratings can be below 0.1 nm, and the efficiency of the grating can be up to 80% at the peak wavelength[96].

In order to detect the spectrum, the two-photon instrumentation was reconfigured, as in Figure 3.3. A dichroic was placed before the x-y scanner to reflect the incident light and transmit fluorescence. The dichroic in Figure 3.3 that directed the light into the objective was replaced with a silver mirror (Chroma, Brattleboro, VT). A spectrograph (MS125, Oriel, Stratford, CT) was positioned after the dichroic and disperses the fluorescence light spectrally. The spectrum is detected using a multi-anode photomultiplier tube (MA-PMT), and a calibrated micrometer drive is used to tune the wavelength range detected by the MA-PMT. The MA-PMT used (R59000U-00-L16, Hamamatsu, Bridgewater, NY), is a linear array of 16 anodes, which can simultaneously detect photons in each of its channels. In-house electronics[96] are used to simultaneously acquire photon counts in each channel. While the traditional spectrographs are often read out using linear charge coupled device (CCD) arrays, we found that MA-PMT is a superior choice for three reasons. First, MA-PMT is single photon sensitive whereas most non-intensified CCDs are not. Second, MA-PMT has relatively few pixels (16 or 32) whereas CCD typically has 512 to 1024 pixels. Since the typical fluorescence spectra are broad, which are about 30-50 nm in bandwidth, the use of high-resolution detectors do not provide better spectral resolution and may decrease detection signal to noise level. Third, the CCD arrays are significantly more costly than the MA-PMT system.

This method of generating a spectrum is more efficient than both the filter wheel and the LCTF. In this device, the collection is done simultaneously while in the filter wheel and LCTF, the emission wavelengths are studied sequentially. With the spectrograph and MA-PMT, the entire spectrum is obtained with a minimal loss of photons, while the other methods throw away photons that are not within the pass band of the filters. In the spectral range relevant to our studies (400-625 nm), the efficiency of the spectrograph system ranges from approximately 30% to 68%. Due to the lower efficiency of the spectrograph system compared to the filter wheel, a slower scanning speed is needed in order to obtain similar photon counts from the same sample. Thus, in the case of the spectrograph, the skin was scanned at a rate of 2 kHz. This is approximately 33 seconds per frame. However, since the full spectrum is collected at once, this result in a net 5 times imaging speed improvement as compare with the filter wheel system, and more than 21 times faster than with a LCTF! This makes the spectrograph system highly desirable for two-photon spectroscopic imaging.

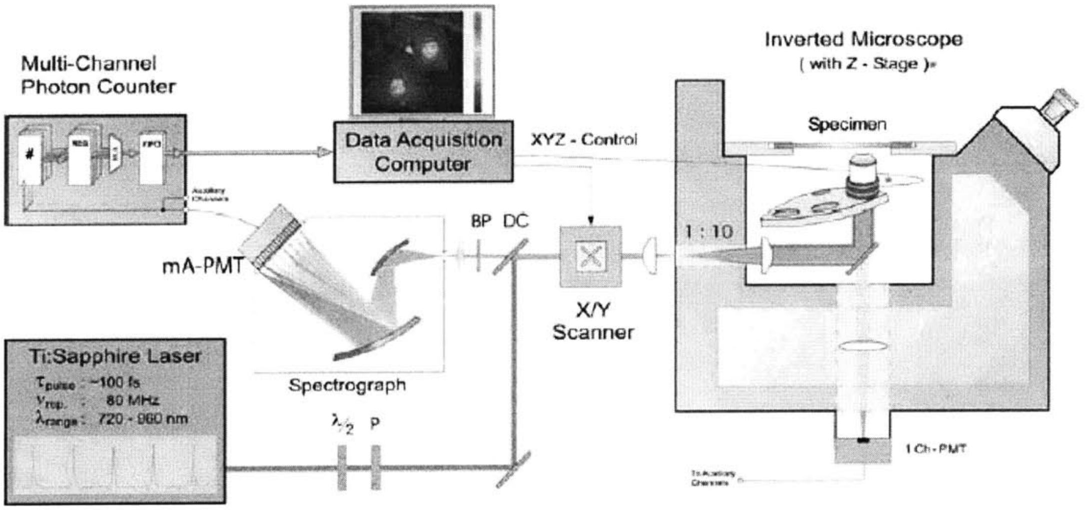

Figure 3.3. Schematic of 16-channel two-photon scanning instrumentation[96].

3.1.1.2. Fluorescence lifetime-resolved imaging

Fluorescent lifetime measurements were performed where the luminescence signal is detected by a photon counting PMT (R7400P, Hamamatsu, Bridgewater, NJ). The signal from the PMT was analyzed using a time correlated single photon counting card (SPC-730, Becker-Hickl[99], Berlin, Germany) to build a histogram of the time of arrival of the photons at the detector. Each image contained 256x256 pixels and each pixel contains 64 time channels spread from 0 to 17 ns. Image size and resolution parameters are the same as emission spectral resolved images.

The lifetime data were fitted by iterative convolution[100] using a double exponential decay convoluted with a 350 ps Gaussian (FWHM) representing the instrument response. A global fitting algorithm[101] based on a least-square optimization procedure from Matlab (The Mathworks, inc. Natick, MA) was used to extract two time constants from a whole image, each decay curve at every pixel containing a variable proportion of those two time constants. Further description of the fitting algorithm and segmentation method that significantly improves the convergence speed and accuracy of the fit will be described elsewhere[102].

3.1.1.3. Spectrally resolved image data format

It is informative to further describe the data matrix obtained from the spectral resolved microscope as describe above. Contained in the two-photon data is information concerning the excitation, emission, and lifetime spectra of a sample. The excitation spectra can be studied by varying the wavelengths that the sample is excited by. The emission spectra can be studied by exciting the tissue at a constant excitation wavelength and measuring the different emission wavelengths. Finally, the lifetime measurements can be determined by studying the residence time of each molecule in its excited state.

To better understand the data format, let us first look at a two-dimensional image, Figure 3.4. In the middle of the section is the sample that is being imaged. The gray circles across the image represent each pixel that is imaged. As the sample is excited by a single wavelength, such as 780nm, there is fluorescence generated within each pixel. As the two-photon beam is scanned across the sample, the fluorescence intensity at each pixel is captured. Imaging provides intensity information at each of the pixels for a single wavelength, and a two-dimensional image can be reconstructed from this information.

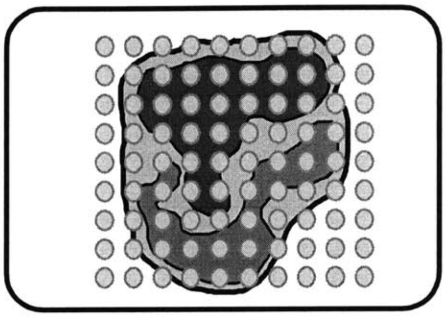

Figure 3.4. Two-dimensional representation of two-photon image.

In order to obtain spectral information, one method is to excite the same sample at different wavelengths, such as from 700 – 920 nm in my case. Each of the different excitation wavelengths is represented by λ_a, λ_b, λ_c, etc. Fluorescence intensity information is obtained at each pixel for each of these wavelengths. This results in spectral information at each of the pixels, and each pixel in the dataset contains a full spectrum of information that is spatially distinct, Figure 3.5. This representation of data can be used to also describe the emission and lifetime spectra.

Typical samples in these experiments are excited at wavelengths ranging from approximately 700 to 920nm. The emission wavelengths are in the visible range with wavelengths ranging from 400 to 625 nm. Lifetime measurement data contains the femtosecond pulse response of the specimen up to about 10 ns. The size of each image is 256 x 256 pixels.

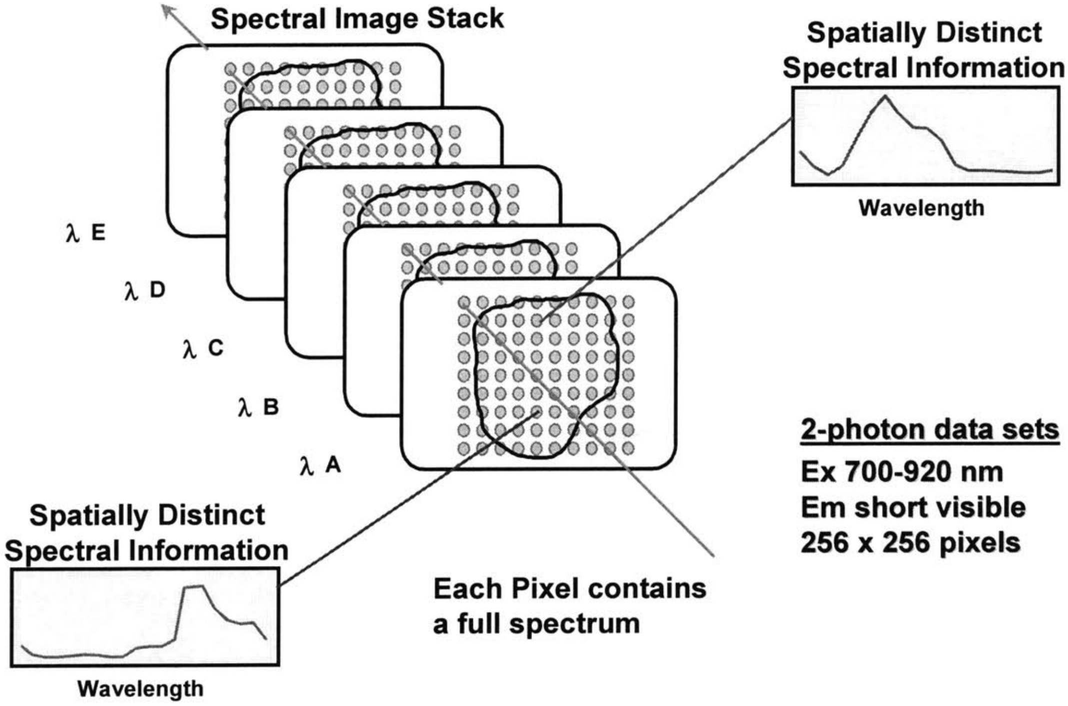

Figure 3.5. Representative spectral data.

3.1.2. Tri-modal microscopy

The merging of different imaging techniques can create new instrumentation that combines the advantages of the different imaging modalities. This system can provide complementary spectral information to allow more accurate interpretation of tissue microscope images. Previous work has already been done joining two different modalities including the combination of optical coherence microscopy and two-photon microscopy[103], the combination of second harmonic microscopy and two photon microscopy[104,105,106,107], and the combination of optical coherence microscopy and confocal fluorescence imaging[108]. This section describes work I have done to construct and implement a multi-modal instrument.

3.1.2.1. Instrument design

Previous work by other research groups has combined two modalities to study tissue. In this thesis, I have built new instrumentation that combines three different imaging modalities. This tri-modal system combines imaging systems studying fluorescence using two-photon microscopy, second harmonic generation using SHG microscopy, and reflectance using optical coherence microscopy. A schematic of this system can be seen in Figure 3.6.

The beam is generated by a femtosecond mode-locked Ti:Sapphire laser (Tsunami, Spectra Physics, Palo Alto, CA) and is directed on to a vibration isolation table (Newport Corporation, Irvine, CA) on which this instrumentation is placed. The repetition rate of the laser is approximately 80 MHz with a 150 fs pulse train, and the center wavelength of the light is 800 nm with a bandwidth of approximately 10 nm. The separation of the laser and the microscope allow isolation of the microscope from the mechanical vibration generated from the laser cooling system. Once the beam is directed on to the vibration isolation table, the beam is split using a 50/50 beam splitter (BS). Half of the light is going to a piezo-mounted reference mirror, and the other half is going towards the sample. In the sample arm, there is a dichroic mirror (D1 – Chroma, Brattleboro, VT) that reflects light above 650 nm and transmits light below 650 nm. It is placed in the beam path through which the incident light reflects. The light enters into an objective and is focused into the sample. A Fluar 20X, 0.75 N.A. air objective (Zeiss, Thornwood, NY) was used in this setup. Through this process fluorescence, second harmonic generation, and reflected light are generated.

The fluorescence and SHG that is propagating in the backwards direction is then separated from the reflected light. Dichroic D1 transmits the reflected light and reflects both the fluorescence and SHG. As the second harmonic wavelength is exactly half of the incident light ($\square_{incident} = 800$ nm, $\square_{SHG} = 400$ nm), it can easily be separated from the fluorescence signal. A second dichroic (D2) is placed in the beam path to separate the SHG signal. Each signal can then be detected using a photomultiplier tube (PMT - Hamamatsu Corporation, Bridgewater, NJ) and is amplified using a transimpedence amplifier (Stanford Research Systems, Sunnyvale, CA). Bandpass filters selected to match the wavelengths of interest can be placed before the PMTs. The signals from the detectors are collected using a 16-bit analog-to-digital converter (A/D) card (National Instruments). As this is all performed for a single point, an image can be formed by scanning a sample using a mechanical translation stage controlled through a computer.

In addition, OCM is accomplished by interfering the reflected light in the sample arm with backscattered light from the piezo-mounted mirror in the reference arm. The path length of each arm must be within the coherence length of the source (~30um) of each other. The piezo-mounted mirror is scanned a distance of 5 microns at a frequency of 100 Hz creating a heterodyne frequency of 2.5 kHz. The light is interfered and detected at a silicon photodiode (PD, Thorlabs, Newton, NJ). The signal from the photodiode is amplified using a transimpedance amplifier and is collected using a 16-bit A/D card. Special care is taken to ensure that the focal plane of the two-photon system matches the focal plane of the OCM system. This is accomplished by placing a silver mirror in the sample arm and adjusting the objective to create an image plane at the surface of the detector. Once this path length of the sample arm is determined, the path length of the OCM reference arm is adjusted to match. Detection of path length matching is accomplished by looking for an interference pattern at the detector. This ensures that the path length of each arm is the same and thus the focal planes of each system are the same. Any signal detected in either the two-photon, SHG, or OCM detectors will be from the same structure. This gives rise to simultaneous detection of all three imaging modalities at the same time.

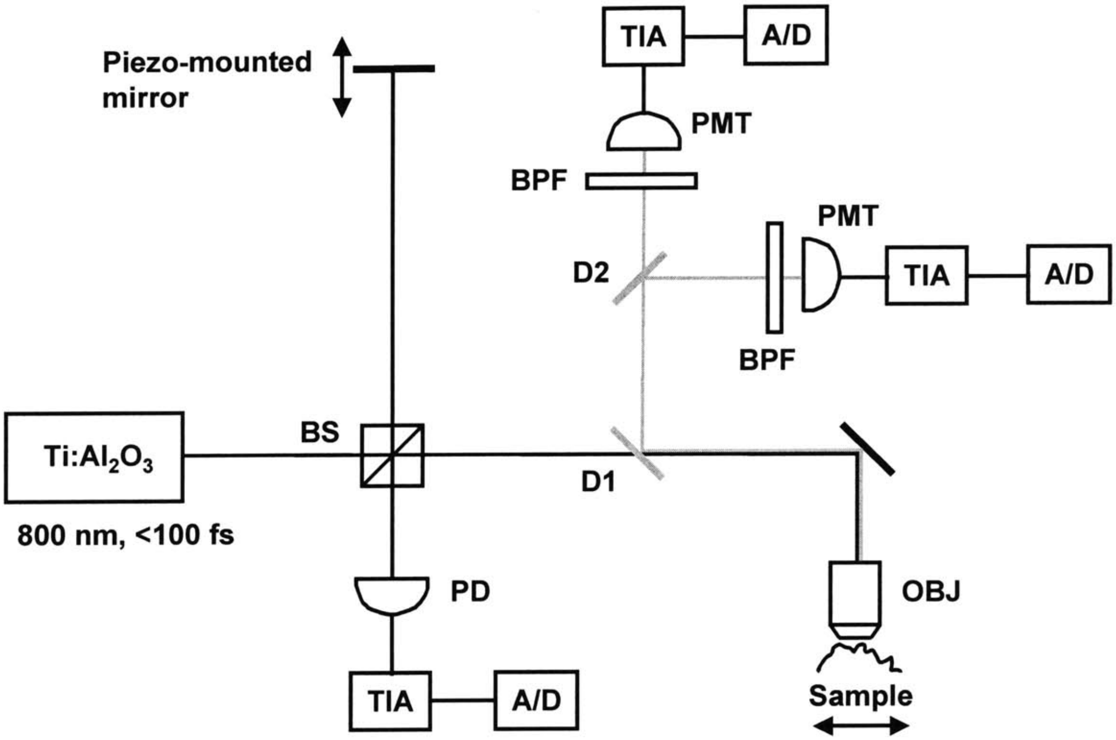

Figure 3.6. Schematic of tri-modal microscope.

3.1.3. Interferometric second harmonic generation microscopy

Improving penetration depth is critical for deep tissue imaging. Due to multiple scattering of photons, the depth discrimination capability of two-photon or second harmonic generation microscopes degrades as one images deeper into turbid specimens. A significant reduction in image contrast is observed as evident from a significant increase in the amount of signal far from the central region of the point spread function (PSF), as illustrated in Figure 3.7. This work, done by Ki Hean Kim at MIT, demonstrates that although the resolution of the PSF measured at the full-width-half-maximum does not change as one images deeper into a scattering sample, the contrast of the PSF decreases . As more signal photons are scattered into the background region, the peak intensity of the PSF decays exponentially with increasing imaging depth and scattering coefficient.

Interferometric detection produces an additional coherence gate that allows better rejection of background signal. Since the coherent gate sharply rejects signal from all but the plane of interest, this reduces background and enhances the signal to noise ratio. Many thick tissues contain collagen, which produces a strong second harmonic signal. Using interferometric detection of the SHG from the collagen may allow us to detect collagen distribution deeper into tissue, which is important in a number of studies such as cancer detector or wound healing. In addition, this can provide complementary information to fluorescence and reflectance microscopy.

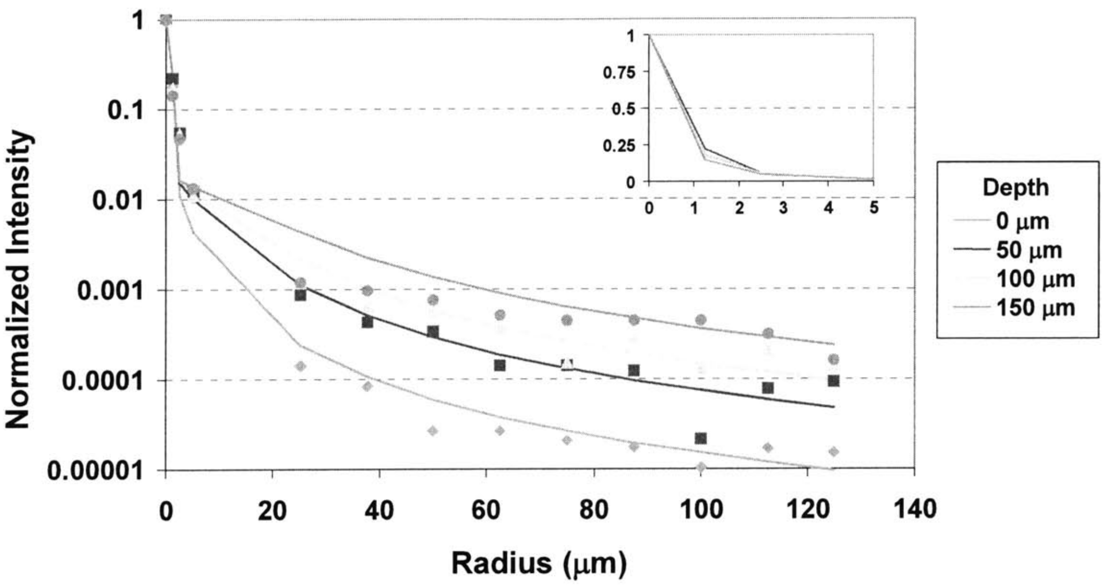

Figure 3.7 Two-photon fluorescence point-spread-function in 2% intralipid[109].

3.1.3.1. Instrument design

SHG signal is coherent. Therefore, interference detection of SHG can be performed in conjunction with standard OCM. Interferometric second harmonic generation microscopy (ISHGM) was implemented by modifying the tri-modal system, as seen in Figure 3.8. In order to have interferometric detection of the SHG signal, a reference arm for the SHG interference had to be created. A second 50/50 beamsplitter (BS2) was placed in the reference arm in order to split the backscattered light from the reference mirror. Half of this light continued straight through the beamsplitter to interfere at the photodiode for conventional OCM. The other half was frequency doubled using a lithium triborate (LBO) crystal through type I phase matching. A half-waveplate (Newport Corporation, Irvine, CA) was placed before the LBO crystal to optimize the SHG from the crystal, and a half-waveplate was also placed after the LBO crystal and rotation of the half-waveplate allows for matching of the phase of the SHG signal from the sample. Dichroic D2 is now replaced with a 50/50 beamsplitter (BS3) that recombines the SHG reference and sample arms and interferes this signal at a PMT. Bandpass filters can be placed in front of each PMT to study the particular wavelengths of interest and reduce background.

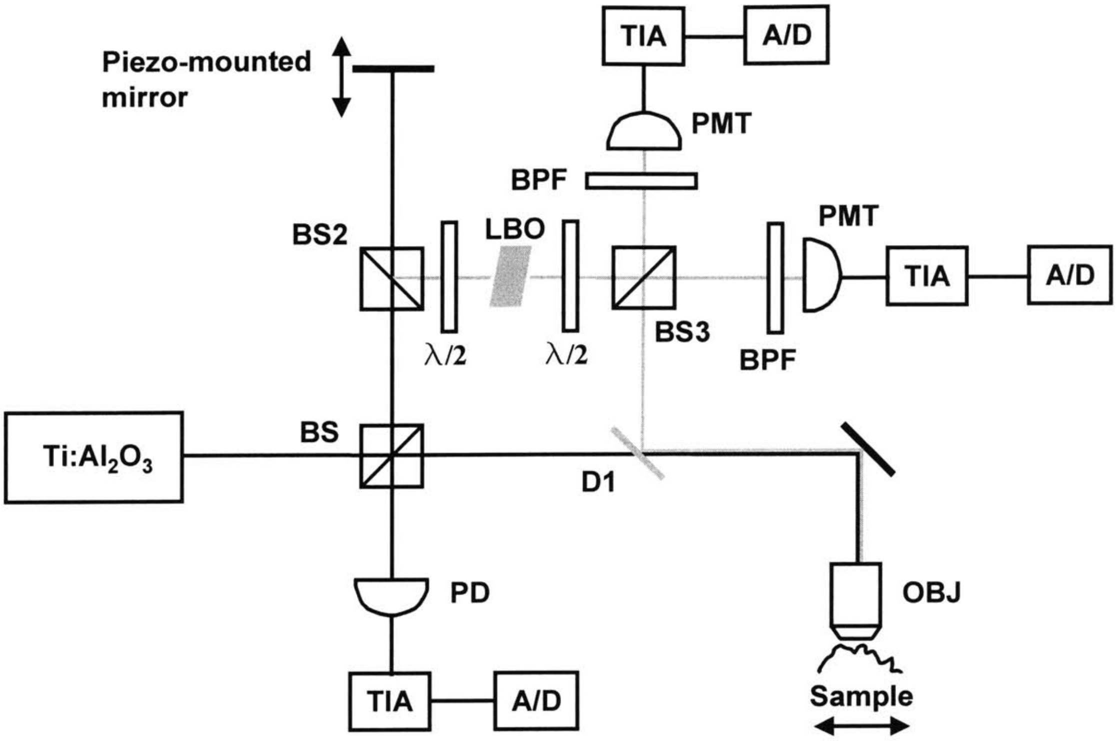

Figure 3.8. Schematic of interferometric second harmonic generation microscope.

3.1.3.2. Limitations of the current ISHGM system

Several problems arose during the implementation of the ISGHM section of the instrumentation. First, this was a difficult system to setup and align. As the path lengths of both the OCM and ISHGM modalities have to be within the coherence length of the laser (~30 um), using bulk optics in the system made this quite difficult. In addition, due to the use of bulk optics, the system was not very interferometrically stable. The addition of numerous bulk optics in the ISHGM increased the interferometric instability of the system and made the instrument more susceptible to mechanical vibrations from the environment. This instability increased the background signal and thus reduced the overall signal to noise ratio of the ISHGM system. However, with care to minimize mechanical instability in the ISHGM system, we are successful in imaging specimens such as fragments of non-linear optical crystals. We are currently not successful in the imaging of biological specimen with high collagen content, such as fish scale or human dermis, using this coherent gated instrument. There are a number of problems associated with the imaging of biological specimen. Firstly, the typical second harmonic efficiencies of these specimens are lower than solid state specimens. However, while the total second harmonic signal from these biological specimens is lower, the signal level should still be within the detection limit of our instrument. We postulate that our difficulty in detecting coherent SHG in biological specimen is due to the fact that SHG is primarily generated in the forward direction. However, we detected the coherent second harmonic signal in the epi-geometry. In the solid state, non-linear optical crystal case, the reflected light comes from the forward going light reflected off a crystal facet surface. Since the crystal facet surface is spatially localized, the optical coherency of the backward reflected signal is guaranteed. In the biological specimen, the origin of the backward going signal is less well understood as there is no well defined reflecting surface. A likely problem in detecting coherent second harmonic signal in the epi-direction may be due to the fact that the backward scattered signal is generated after multiple scattering within the thick specimen. If the backward going photons are a result of multiple scattering in a turbid medium, their optical path lengths may have a very broad distribution that may be significantly wider than the coherent gate. This may result in the majority of these backscattered photons being rejected by the coherence gate. We are currently investigating the possibility of implementing a ISHGM system that allows the simultaneous detection of forward and backward going SHG to investigate this issue.

3.2. Spectral analysis algorithms

Spectral signature provides insight into tissue biochemistry and metabolism. The relative abundance of endogenous fluorescent species is related to tissue physiological and pathological states. Spectrally resolved two-photon fluorescence, SHG, and reflected light images can contain rich information. Our goal is to correlate biochemical spectral information with morphological images, which should allow better understanding of tissue physiological and pathological states. However, it is often difficult to interpret these spectra due to the complex nature of tissue. As there are multiple species present within the tissue, the spectral signatures and the distributions of these components can be difficult to measure when there is significant spectral overlap. We are developing two novel image analysis approaches to study two-photon and SHG images.

First, by combining spectroscopic analysis with two-photon microscopy, structural information from the image can provide additional a priori information for spectral decomposition can be obtained. In addition, this three-dimensional resolved spectroscopy can reduce the amount of mixing of spectra by enabling the study of signal from microscopic volumes within which fewer independent fluorescent species reside. This way, the identity and distributions of each pure biochemical species can be more easily determined.

Second, we apply a quantitative algorithm to decompose this mixture of spectra into individual components based on numerical multivariate curve resolution. We demonstrate identification of individual endogenous fluorescence species based on excitation and emission spectrally resolved images.

3.2.1. Imaged guided spectral resolved analysis

Image guided spectral analysis is a technique to study the spectrum of biochemical species in 3D two-photon and SHG images. The two-photon images consist of a mixture of pure component responses. In order to extract chemically significant information from these images, we studied spatially resolved spectra from different structural levels – (1) the overall bulk emission spectra from the whole tissue, (2) the emission spectra at individual stratified epithelial cellular layers and the stromal layer within the tissue, and (3) the emission spectra from specific tissue structures based on image segmentation, Figure 3.9. We applied this imaged based spectral analysis method to study human epidermal and dermal structures.

3.2.1.1. Bulk spectrum

In order to obtain the bulk emission spectrum for each excitation wavelength, the measured intensity was acquired over the entire volume. This was accomplished using two different methods. The "weighted" method takes the intensity data at each pixel in the volume and sums the intensity over all pixels. This was repeated for the data imaged through each emission filter to result in the emission spectra. These steps were repeated for each of the different excitation wavelengths. The resultant spectra were then normalized. The "non-weighted" method takes the emission spectra at each pixel in the volume and normalizes each spectrum at every pixel. These normalized intensities were then summed for each emission wavelength, which results in a single emission spectrum that is then normalized. These steps were repeated for each of the different excitation wavelengths.

3.2.1.2. Layer resolved spectrum

The emission spectra for individual depths were obtained from the distinct epithelial layers and from the stromal layer. In the skin specimen of our study, we obtained the emission spectrum for four different depths that were representative of the following structures: stratum corneum, stratum spinosum, basal layer, and dermis. The individual layers were identified by morphological comparison with known histology of skin. The emission spectrum for each layer was obtained by taking the image of each layer and averaging the intensity from each pixel within the image. This imaging procedure was repeated for each emission filter to obtain the emission spectra. The emission spectra of surgically exposed dermis were also studied. This enabled us to further investigate the components of the dermal layer. We were also able to reconstruct the different components present in the dermis by reconstructing the overall image from each filter. This was done by imaging a 10 um section of dermis in 0.5 um increments at an excitation wavelength of 780 nm through each emission filter. Three-dimensional images were then reconstructed for these emission filters.

3.2.1.3. Feature resolved spectrum

The emission spectra of different skin morphological structures can be determined. As a first demonstration of this approach, an intensity segmentation was performed on the images to resolve major structures in the skin. We select individual structures within an image and obtain the average intensity of the structure at each emission wavelength to obtain the emission spectra. In the dermis, we can isolate elastin-rich structure from collagen-rich structure based on intensity segmentation. By doing this, we can isolate the emission spectra associated with a particular structure and separate it from the emission spectra of the entire image.

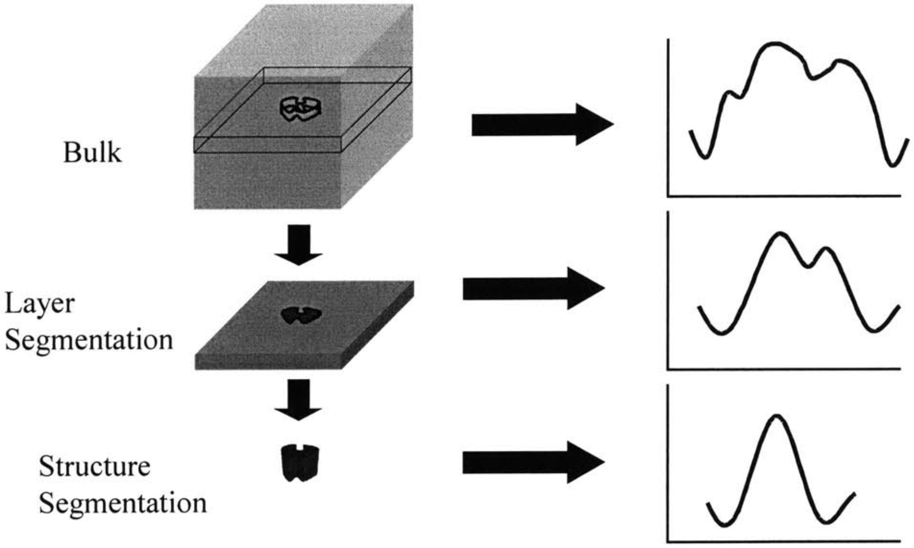

Figure 3.9. Schematic of analysis methods of extracting spectral information

3.2.2. Multivariate curve resolution

3.2.2.1. Overview

Multivariate curve resolution (MCR) is process to reduce a multi-dimensional, heterogeneous data set in terms of a relatively few number of variables which represent most of the information in the original dataset. A flow chart of this process can be seen in Figure 3.10. A multivariate data set that comes from spectral imaging of a specimen is a mixture of many different chemical components. In order to reduce this large amount of data, a principal component analysis (PCA) is performed to reduce the data to capture the primary independent spectral components. In the specific case of studying the components that comprise most of the autofluorescence seen in skin, the number of factors produced is the number of autofluorescent species present. This case will be further discussed in Chapter 5.

PCA does not provide an unique decomposition of the data set as there are a number of models that can satisfy the initial data. In order to limit these solutions to something that will reflect the true properties of tissue, constraints have to be imposed. The standard way to do this is through ALS (alternating least-squares regression). ALS imposes realistic boundary constraints that will force our results to conform to what is known a priori about the data structure. The typical constraints that are imposed on fluorescence spectral data are non-negativity or positivity, and unimodalness. Positivity is always satisfied with intensity based data. Unimodalness implies the spectrum has a single peak. Although it is not always straightly correct, this condition often represents the spectrum of many common fluorophores.

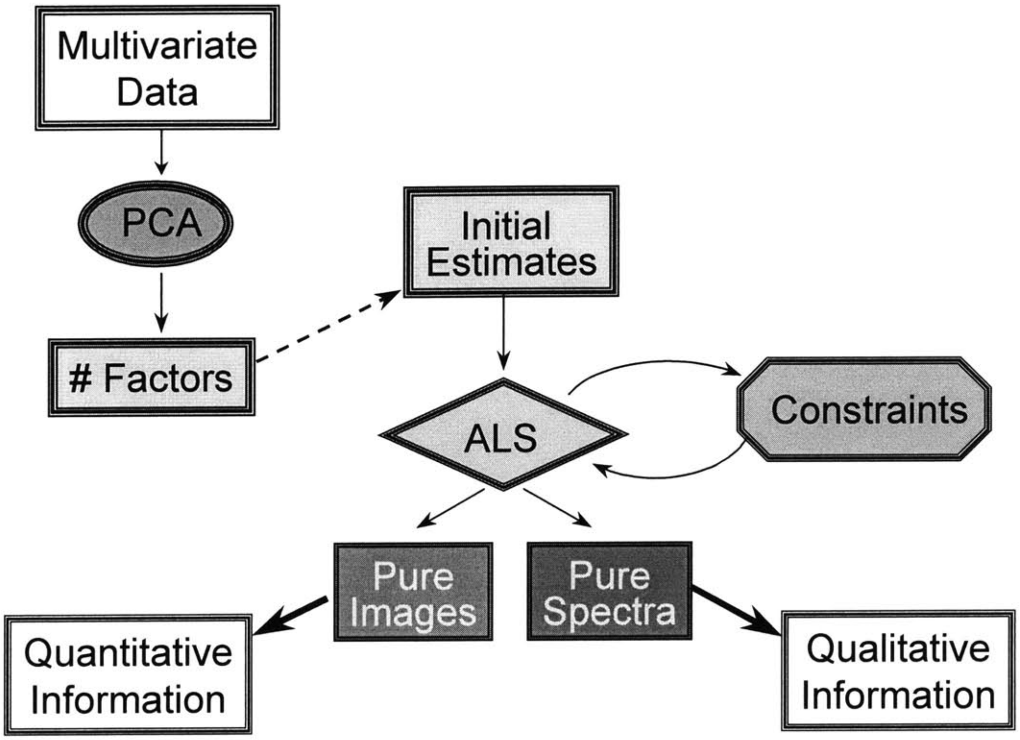

Figure 3.10. Flow chart of multivariate curve resolution process.

The ALS algorithm takes the factors from the PCA as initial estimates and imposes the constraints. The results of the ALS are the pure spectra and pure images. The pure spectra are the real spectra of distinct endogenous fluorescent species. The pure images map the concentration distribution of these individual species in 3D.

3.2.2.2. Theory

With MCR, each voxel in the three-dimensional image contains a full spectrum. This technique assumes no correlation between individual pixels, so reconstructed structural images of individual chemical species, along with their distribution in the sample can be compared with known tissue physiology previously determined by histological and biochemical methods. The comparison provides an independent verification of the accuracy of the multivariate curve resolution algorithm.

The data to be analyzed are four-dimensional data sets that include three spatial dimensions and an excitation wavelength dimension (x, y, z, λ). . Ignoring the possible correlation between pixels, the four dimensional data set is converted into two dimensions (n, λ) for further analysis (two-way factor analysis) where n is the index of the voxels in a 3-dimensional data set.

Two-way factor analysis assumes a bilinear data structure and attempts to separate the original data matrix of spectra, **D**, into two sub-matrices, **C** and **S**:

$$\mathbf{D} = \mathbf{C}\,\mathbf{S}^{\mathbf{T}} + \mathbf{E}$$

where, **C** is a matrix of coefficients related to the real image or concentration profiles (scores), **S** is a matrix of vectors related to the real spectra (factors), and **E** is a matrix of spectral residuals.

The equation above describes the standard PCA solution. Since this is in general an ill-posed problem, there are many possible solutions that satisfy the equation. **C** and **S** are composed of linear combinations of the real concentration profiles, and linear combinations of real spectral profiles of the pure chemical species present in the original data set. In other words, there is no unique solution to the equation; many possible solutions exist that will fit the model equally well.

Since the objective is to produce pure factors and scores, the number of possible solutions has to be restricted in some chemically or physically meaningful way that will force the resulting concentration and spectral profiles to reflect those of the real components in the data. The standard way to achieve this is through a process called constrained alternating least-squares regression (ALS). ALS is also sometimes referred to as simply alternating regression (AR) The idea behind ALS is to impose realistic boundary constraints on the least-squares solution that will force the spectral profiles and concentration profiles to conform to what is known *a priori* about chemically significant aspects of the data structure. One of the most commonly imposed constraints is positivity, which states that spectral profiles and concentration profiles cannot be less than zero. This and sometimes other constraints are imposed on the data structure during the least-squares optimization process.

Usually ALS takes the abstract scores and factors from the PCA as input at the start of the process. A way to help the optimization process along, giving it a head start, is to rotate the abstract vectors in a self-modeling way taking advantage of the basic underlying structure of the data. Varimax rotation is such a vector rotation method and is applied to the abstract factors in MCR in order to segregate the more significant factors from the least significant ones. This is done as the name suggests by rotating the factors such that the total variance of the squared vectors is maximized while keeping all vectors orthogonal to each other. This often, but not always, makes it easier for the ALS process to extract pure variables and results in a smaller number of necessary iterations and better resolution of chemical information.

The ALS process is then initiated either after the varimax rotation step, or after the PCA step. Non-negativity constraints are imposed sequentially on the scores and factors with a least-squares regression step performed before proceeding to the next step. Starting with the score matrix, all negative values are set equal to zero, or forced toward zero in some way. The exact nature of the non-negativity constraint greatly depends on the method chosen. Then new factors are generated in a least-squares sense from the original data matrix via some form of a generalized inverse. Again, the exact method of performing the inverse step depends on the form of the least-squares regression equation.

$$\mathbf{S} = \mathbf{C}^{+}\,\mathbf{D}^{*}; \qquad \mathbf{c}_{i,j} \geq 0 \text{ for all i,j}$$

where $\mathbf{C}^{+} = [\mathbf{C}^{\mathbf{T}}\mathbf{C}]^{-1}\mathbf{C}^{\mathbf{T}}$ is the left pseudo-inverse of **C** and $\mathbf{c}_{i,j}$ are the elements **of** $\mathbf{C}^{+}$.

The factor matrix is then constrained in the same way as before, and new scores are generated in a similar manner. An additional constraint applied to the factors only is an equality/closure constraint that normalizes all factors to unit vector length. This step is necessary if quantitative or semi-quantitative image information is required as a final result. This factor normalization step forces all the variance into the intensity submatrix that provides a consistent scaling between the voxels in these images.

$$\mathbf{C} = \mathbf{D}^* \mathbf{S}^+ \qquad s_{i,j} \geq 0 \text{ for all i,j and } \mathbf{S}^T\mathbf{S} = 1$$

where $\mathbf{S}^+ = \mathbf{S}^T[\mathbf{S}\mathbf{S}^T]^{-1}$ is the right pseudo-inverse of **S** and $s_{i,j}$ are the elements of $\mathbf{S}^+$. The original data matrix, **D**, can be used in the above equations, but, **D***, the reduced rank matrix (data reconstructed from only the chemically significant factors determined from PFA) is preferred since it will lend stability to the computations. The entire process starts over again and continues until the solution converges according to a predefined convergence criterion. In this case, the convergence criterion is based on the minimization of the sum-of-squares of the residuals of the reconstructed data set compared to the original data set, C_r.

$$Cr = \sqrt{\frac{\sum_i \sum_j \left(d_{i,j} - \hat{d}_{i,j}\right)^2}{\sum_i \sum_j \left(d_{i,j}\right)^2}}$$

where $d_{i,j}$ and $\hat{d}_{i,j}$ are the matrix elements of the reconstructed data set and the original data set respectively. Other stopping criteria may be used as well depending on the nature of the data being analyzed. The application of MCR to resolving skin autofluorescence components can be found in Chapter 5.

Chapter 4

Sample preparation and experimental procedures

4.1 Ex vivo human skin

The basic physiology of human skin is seen in Figure 4.1[110]. Skin is comprised of two overall sections, the epidermis and dermis. The epidermis is the outermost portion of the skin and forms a protective layer to prevent loss of moisture from the body. The epidermis is comprised primarily of keratinocytes. The keratinocytes differentiate in the basal layer and migrate towards the surface of the skin. The outermost layer of the skin is the stratum corneum and is composed of dead, cornified keratinocytes. The epidermis is located above the dermis. The dermis provides structural support for the epidermis and is primarily composed of collagen and elastin matrix with a sparse population of cells such as fibroblasts.

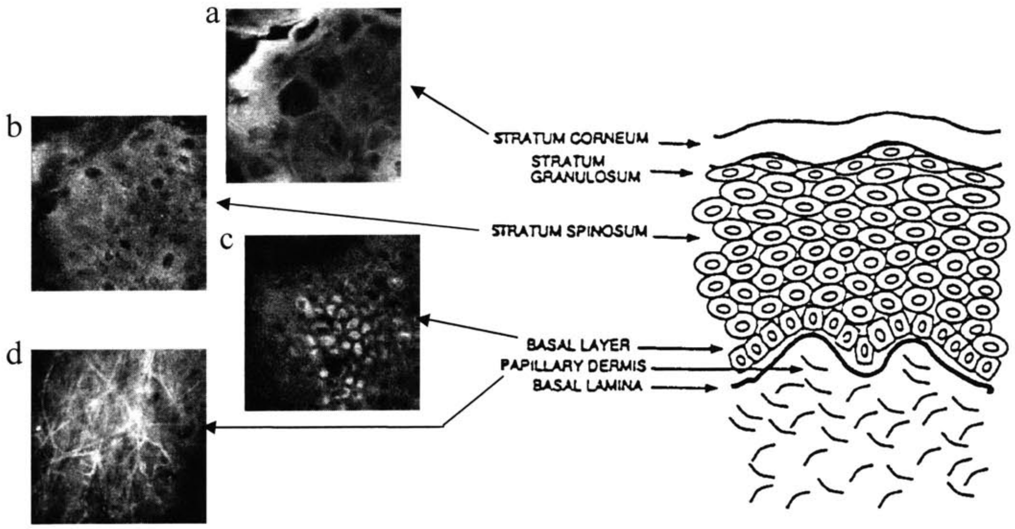

Figure 4.1. Basic physiology of human skin and corresponding two-photon images of several layers: (a) stratum corneum, (b) stratum spinosum, (c) basal layer, and (d) dermis.

The ex-vivo human skin was obtained from the expired stock of a skin bank. The specimen was stored at -3°C before use. One specimen, 1 cm by 1 cm, from the skin of a Caucasian subject was studied. The sample of skin was prepared by placing it in a hanging drop microscope slide containing a piece of damp sponge. The specimen was sandwiched between the coverslip and the damp sponge in order to maintain its moisture.

Two types of samples were examined. The first type of sample was imaged in the normal orientation with the stratum corneum placed closest to the coverslip. The second type of sample was surgically exposed skin where the exposed dermis was placed closest to the coverslip. The typical excitation power was 20 mW on the specimen.

4.2.1. Two-photon spectroscopy experiments using multivariate curve resolution

A Fluar 40X oil objective (Zeiss, Thornwood, NY) was used to image the sample. The image volume was a 116 um x 116 um x 100 um deep volume of skin with a frame rate of 32 seconds per frame. The skin was imaged at fifteen different depths within the volume in increments of 5 um and each section was imaged at twelve different excitation wavelengths ranging from 700 nm to 920 nm in increments of 20 nm.

4.2.2. Two-photon spectroscopy experiments using image guided spectral analysis

A Fluar 40X oil objective (Zeiss, Thornwood, NY) was used to image the sample. The size of each image acquired was 116 um x 116 um with a frame rate of 32 seconds per frame. In the axial direction, an 80 um thick section of skin was imaged in 5 um step increments. The sample of skin was imaged at three different excitation wavelengths – 730, 780, and 830 nm – in three dimensions. For each depth within the skin, emission information was obtained by rotating the filter wheel and imaging through the various filters. This was repeated for all depths within the sample. The emission spectrum of fluorescein[111] and POPOP[112] were acquired with this system, and these spectra were used as calibration.

4.3. Skin equivalent model

A skin equivalent model is a three-dimensional engineered tissue construct, which is an *in vitro* model of the skin. This tissue model provides an alternative to traditional animal testing and is conducive to research that is not feasible with traditional animal, monolayer cell culture, or clinical test procedures. The skin equivalent models (EpiDermFT-312, Mattek Corporation, Ashland, MA) used in these experiments have both an epidermis and dermis. The epidermis is approximately 100-120 microns thick while the dermis is approximately 1 mm thick. The diameter of the tissue is approximately 8mm^2.

The skin equivalent model is comprised of normal, human-derived epidermal keratinocytes (NHEK) and normal, human-derived dermal fibroblasts (NHFB). The NHFB were embedded in a collagen I gel, and the NHEK were seeded on top of the collagen gel. The tissue constructs are cultured for up to 21 days in serum-free culture medium, and the constructs maintain an air/liquid interface and are fed only through the basolateral (bottom) surface. These systems result in a stratified, differentiated full-thickness model of the human dermis and epidermis.

4.3.1. Photoaging

The skin equivalent model was exposed to two different UV doses. The UV light was situated so that it only enters through the stratum corneum. An 8-Watt ultraviolet lamp (Model FB-UVLS-80, Fisher Scientific, Pittsburgh, PA) was used in order to irradiate the skin with UV light. The lamp was operated at a wavelength of 365 nm, which is in the UVB range. The intensity of the lamp at a distance of 15 cm was 470 uW/cm^2. A dose of 10mJ/cm^2, Dose 1, was applied to three samples, and a dose of 40 mJ/cm^2, Dose 2, was applied to three other samples. Dose 1 is equivalent to half of the minimum erythema dose (MED)[113], which is the minimal single dose of UVR that is required to produce erythema in exposed skin, and Dose 2 is equivalent to twice the MED. These two dosages were chosen because Dose 2 will definitely create erythema in human skin, and Dose 1 should be sufficiently below the MED so as not cause erythema.

An Achroplan 40X water objective (Zeiss, Thornwood, NY) was used to image the sample using the 16-channel spectrograph instrumentation. Each volume of skin was approximately 116 um x 116 um x 180 um deep and imaged at a frame rate of 32 seconds. Each sample was imaged in two separate volumes due to the fact that the piezo being used only had a travel of 100 microns. A microscope stage height is repositioned to image the deeper volume. Each 100 um volume was imaged at 41 different depths in 2.5 um increments. The first volume was imaged from the surface of the tissue at the stratum corneum to a depth of 100 um. The z-drive was than re-indexed so that the second volume of data was imaged from approximately 80 microns to 180 microns. This allowed for an overlap of images of approximately 20 microns allowing for registration of the two volumes. The volumes from the surface to 100 microns deep were excited by an incident power of 350 mW, and the volumes from 80 microns to 180 microns were excited by an incident power of 500 mW. A sample from each dosage was imaged 10 minutes after exposure, 24 hours after exposure, and 48 hours after exposure.

In order to image the skin equivalent model from the apical surface, the specimen had to be removed from the tissue culture insert it was contained in. The membrane with the sample on top was removed from the insert. The sample was then placed on a glass bottom dish with the stratum corneum placed directly on the glass coverslip.

4.4 Fluorescent microspheres

Fluorescent microspheres were imaged using the tri-modal microscope. A mixture of 1.0 um yellow-green fluorescent microspheres (515 nm emission peak, Molecular Probes, Eugene, OR), and 2.0 um blue spheres (415 nm emission peak, Molecular Probes, Eugene, OR) were imaged.

4.5 Black tetra fish scale

A black tetra fish was obtained from a local pet store. The specimen was stored at -3°C before use. A 3 mm x 3 mm section of fish scale was removed from the specimen and placed on a glass microscope slide. The specimen was sandwiched between the coverslip and the glass slide, and the edges of the coverslip were sealed.

4.6 Barium borate crystal (BBO).

A 3 mm x 3 mm x 1 mm thick barium borate crystal (United Crystals, Flushing, NY) was used as a sample to generate a strong second harmonic signal. The crystal was placed in a specially machined holder to contain it. The crystal was held in place along its edges using tape for ease of removal from the container, and no coverslip was used.

In addition, BBO crystal particles approximately 30 um in diameter were studied. The crystal particles were created by taking a 3 mm x 3 mm x 2 mm crystal and crushing the crystal in a hydraulic press using 5,000 PSI. Further grinding of the crystal particles was accomplished by placing the particles between two glass microscope slides and rubbing the slides together to create smaller, more uniform particles.

Chapter 5

Two-photon spectral resolved microscopy results

The ability to quantify tissue morphology and endogenous luminescence species distribution is useful for physiological and pathological studies. Our studies using the two-photon spectral resolved microscope focus on skin physiology and pathology. Autofluorescence has been used as an assay for skin cancer[114] and can be used as an indicator of the natural aging and photoaging[115] processes of skin. The basic microscopic structure and bulk spectroscopic properties of human skin have been studied previously[116]. This basic knowledge of the dermal system provides a firm basis for more in depth spectroscopic analysis presented in this chapter. We present two spectroscopic studies with the aim of identifying dermal endogenous luminescence species. The first study is based on excitation spectral resolved imaging and multivariate curve resolution analysis. The second study is based on emission spectral resolved imaging and structural resolved analysis. Finally, we applied the two-photon spectral resolved microscope to study skin photoaging process in a dermal equivalent system.

5.1. Two-photon 3-D mapping of tissue endogenous fluorescence species based on fluorescence excitation spectra using multivariate curve resolution (MCR)

5.1.1. Overview

Endogenous fluorescence species in the tissue have their unique excitation and emission spectra. In this study, we vary the excitation wavelength in the study and collect the fluorescence from 350 to 600 nm. The excitation wavelength is varied between 700 - 920 nm. The range of fluorescence excitation wavelength is chosen based on the bandwidth of the Ti-Sapphire laser (from 700-1000 nm) and the expected fluorescence excitation spectra of common tissue fluorophores. For the emission band, the lower band limit is set by the transmittance of the glass objective and the upper band limit is set by the dichroic filter and the barrier filter. This pass band captures most of the fluorescence signal generated. We further apply MCR approach to identify unique fluorescence species in the tissue. Our choice of multivariate curve resolution is based on two rationales. First, the two-photon excitation spectra of most endogenous fluorophores are unknown and have not been previously measured. Therefore, spectral decomposition techniques that are based on simple projection onto known basis sets cannot be applied here with little knowledge of the basis set. Second, the MCR approach allows a mathematically rigorous approach to identify the number of independent luminescence factors corresponding to independent biochemical species in the tissue with minimal a priori assumptions. MCR is a powerful technique to identify the presence of unknown luminescence species in tissues.

5.1.2. Results and discussion

From the MCR analysis, it was determined that seven factors (biochemical components with distinct excitation signatures) contribute to most of the autofluorescence that was observed in human skin. The MCR analysis provides two pieces of information about each chemical component. Each piece of information alone is not sufficient to identify the different chemical components that are present. First, MCR provides the excitation spectrum of the individual component. Second, MCR provides the 3D distribution of the specific component. The 3D distribution can be further analyzed to generate a depth profile of the component. The depth profile shows us the distribution of each component within the volume of skin as a function of depth. Thus, we can understand the location and concentration of each component within the skin. From all of this information, we can reconstruct each section of skin due to each individual component. This allows us to study the structure of a particular chemical component and eventually compare it to known structures obtained by more traditional techniques such as histopathology.

As mentioned previously, there are many possible solutions for the MCR analysis. In order to limit the results, there are non-negative constraints that are placed on the spectrum and their contributions to the autofluorescence intensity. As of now, the two-photon excitation spectra of most endogenous fluorescent components in skin have not been studied. Although the one-photon excitation spectra of many endogenous fluorophores are known, there can be significant differences between one- and two-photon excitation spectra due to the different quantum mechanical selection rules in the excitation process. Thus, there are not many existing studies with which to compare our excitation spectra results. Therefore, the depth profiles and reconstructed morphological images are essential. By comparing this distribution information with known tissue physiology, it allows us to associate the spectral components with known biochemical species. Figure 5.1 shows the results of the MCR analysis by displaying each factor with the excitation spectrum, associated depth profile, and reconstructed image. For example, the distribution of melanin in the skin is known. When comparing this to our results, we can see that Factor #4 is the familiar structure of melanin cap above the basal cells and is concentrated at a depth of approximately 30 – 40 um deep corresponding to the epidermal-dermal junction. This is consistent with previous studies[117].

In addition to Factor #4 at the epidermal-dermal junction, there are three factors observed in the dermis (#5, #6, and #3) and three factors observed in the epidermis (#7, #1, and #2). Factors #5 and #6 both have the well-defined structure of elastin fibers that exist in the dermis. Again we see that the depth profile follows what we know about elastin. It is concentrated in our sample at approximately 35-60 um deep but also existing in high concentrations even deeper, which corresponds to dermis in the skin. One can see that factor #5 and #6 have similar spectra and morphological distributions. It is certainly possible that they correspond to the same species as it is known that MCR process can sometimes overestimate the number of independent factors.

Factor #3 has a very similar depth profile to the elastin fibers but has a different structure. From studying the reconstructed image, the component is seen to have a more mesh-like structure. The most consistent identification of this component is the collagen mesh in the skin. It is interesting to note that the collagen signal is mostly due to SHG. Since we are detecting luminescence signal over a broad bandwidth from about 350-600 nm, one would expect the excitation spectrum for SHG to be also broad. The relatively narrow excitation peak at about 900 nm may be due a combination of two effects. The first effect corresponds to the lower tissue scattering for light at longer wavelengths that results in a stronger SHG transmitted at longer wavelength. The second effect is that the detector has high quantum yield at shorter wavelength and favors detecting SHG generated at shorter wavelengths. The interplay between these two opposing effects is consistent with the narrower excitation peak observed for collagen SHG.

Factor #7 also exists in the stratum corneum and extends throughout the epidermis. Morphologically, this factor appears to distribute throughout the cytosol of the keratinocytes. Further, an excitation maximum of 740 nm is observed. Both the morphology and the spectral profile are consistent with assigning this factor to NAD(P)H, which occurs throughout the epidermis. NAD(P)H fluorescence is further related to cellular metabolic rates[118].

In both Factors #1 and #2, we see that the reconstructed images have the typical structure of the stratum corneum, consisting of flattened keratinocytes. From the depth profiles we see that the concentration of these two factors is within the first 10 um of skin, which is where the stratum corneum occurs. Given that the stratum corneum is exposed to outside environmental contaminants and consists of cornified cells, the exact biochemical factors responsible for its fluorescence can be difficult to be ascertained. Today, we cannot assign the biochemical origins of Factor #1 and Factor #2 with certainty. Potentially, these factors originate from NAD(P)H and proteins (tryptophan) retained in the cornified cells[119].

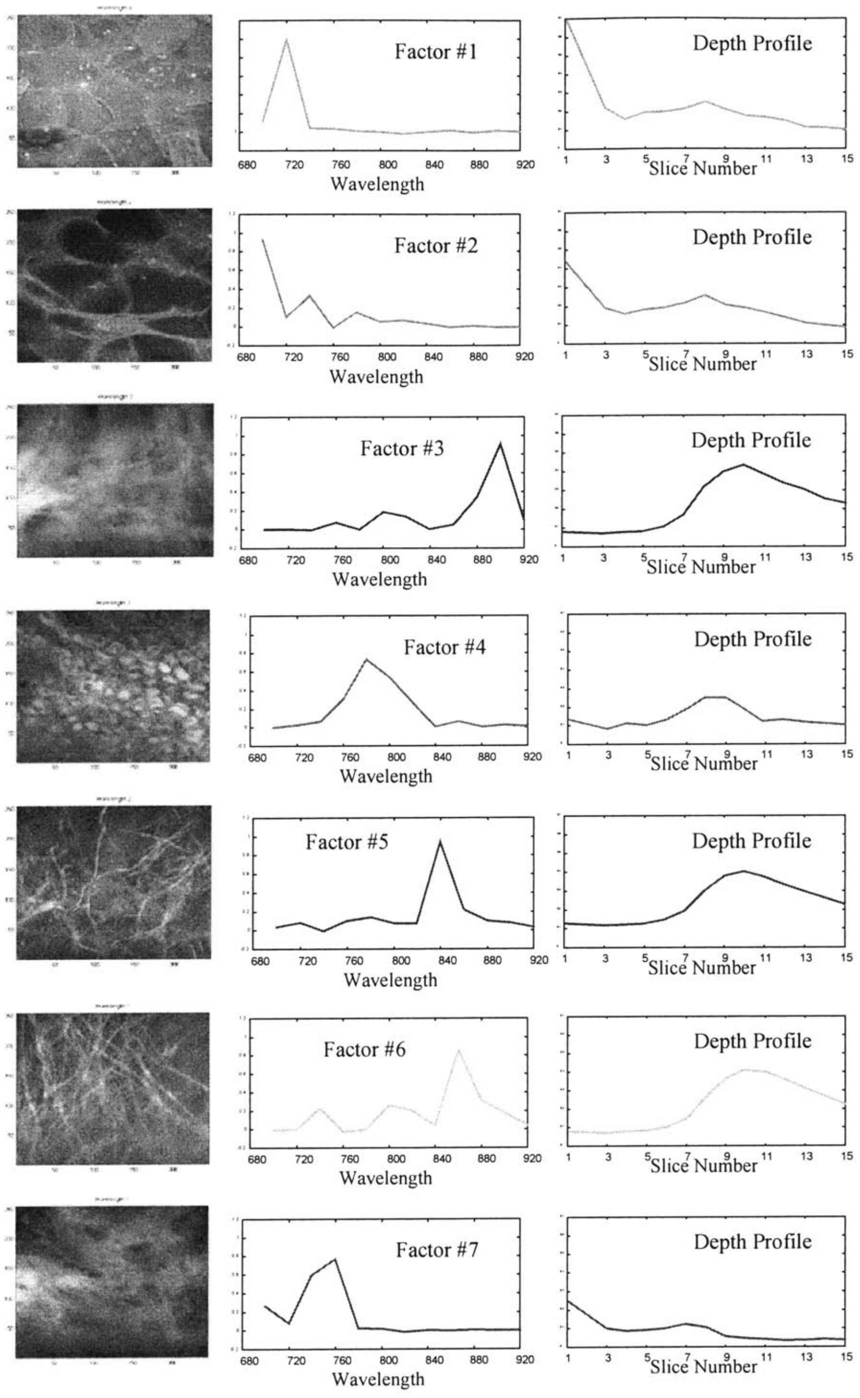

Figure 5.1. Results from MCR analysis.

5.1.3. Conclusions

We have created a new technique that incorporates both two-photon excitation for deep tissue imaging and multivariate curve resolution in order to extract the chemical components within the skin. This new method will enable us to eventually identify each chemical component that comprises the autofluorescence in skin. It also enables us to quantify the distribution of each chemical component in 3D within the tissue. Further, by knowing the excitation spectrum of each endogenous fluorescent species, we can optimize the wavelength with which to study the different dermal endogenous fluorescence species. In addition, autofluorescence studies allow tissue structure, biochemistry, and metabolism to be imaged without the use of exogenous dyes that opens the door for future clinical studies. In the future, we will combine the emission spectrum study in addition to the excitation spectrum study to provide additional information to better constrain the MRC analysis.

5.2 Two-photon 3-D mapping of tissue endogenous fluorescence species based on fluorescence emission spectra using image guided spectral analysis

5.2.1. Overview

Realizing that the tissue morphology provides powerful a priori information to constraint spectroscopic analysis, emission spectroscopic study of ex vivo human will be combined with high resolution imaging based on two-photon microscopy. We demonstrate the ability of using tissue morphological information to guide spectral analysis. Further, we choose to focus on the emission spectrum. Unlike excitation spectra, emission spectra are the same for one- and two-photon excitation processes and the emission spectra for most typical tissue luminescence species are known.

5.2.2. Results

The overall emission spectrum for the entire volume of skin was obtained for three different excitation wavelengths - 730 nm, 780 nm, and 830 nm. These results can be seen in Figures 5.2 (a) and (b), which compare the "weighted" and "non-weighted" methods of generating the bulk spectrum. In the "weighted" method, Figure 5.2(a), the bulk spectra is obtained by a photon count from each point within this tissue and averaging them. In the "non-weighted" method, Figure 5.2(b), the bulk spectra are obtained by weighing the different depths equally.

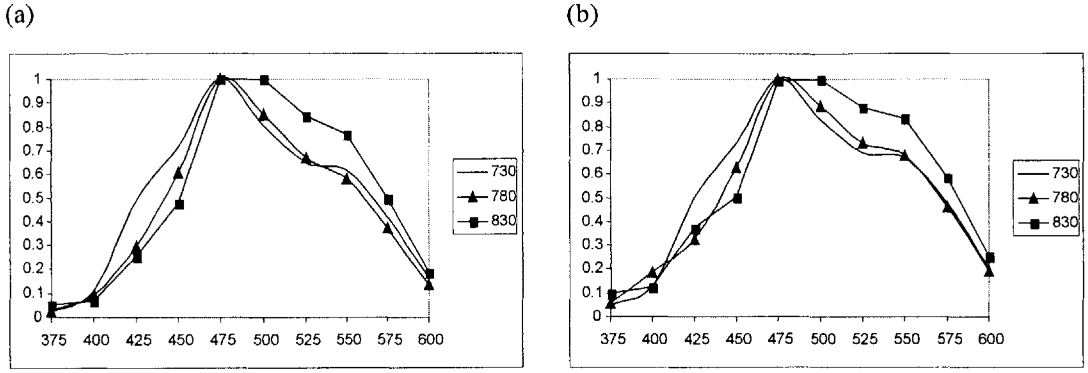

Figure 5.2. Bulk emission spectra of human skin at three excitation wavelengths: 730 (——), 780 (—▲—), and 830 (—■—) nm by the (a) "weighted" and (b) "non-weighted" methods.

The emission spectrum was obtained for four different layers within the skin that were representative of the following structures: stratum corneum, stratum spinosum, basal layer, and dermis. Representative spectral data and the resulting emission spectra can be seen in Figure 5.3. The emission spectra were obtained for three different excitation wavelengths – 730, 780, and 830 nm. Figures 5.3(a) – (d) show the same area in each layer excited at 780 nm and imaged using different emission filters. In each emission spectra, there are peaks at 475 nm and 550 nm. When exciting at 780 and 830 nm, one observes the appearance of two new peaks centered at 400 and 425 respectively that grow in intensity as one images deeper into the skin.

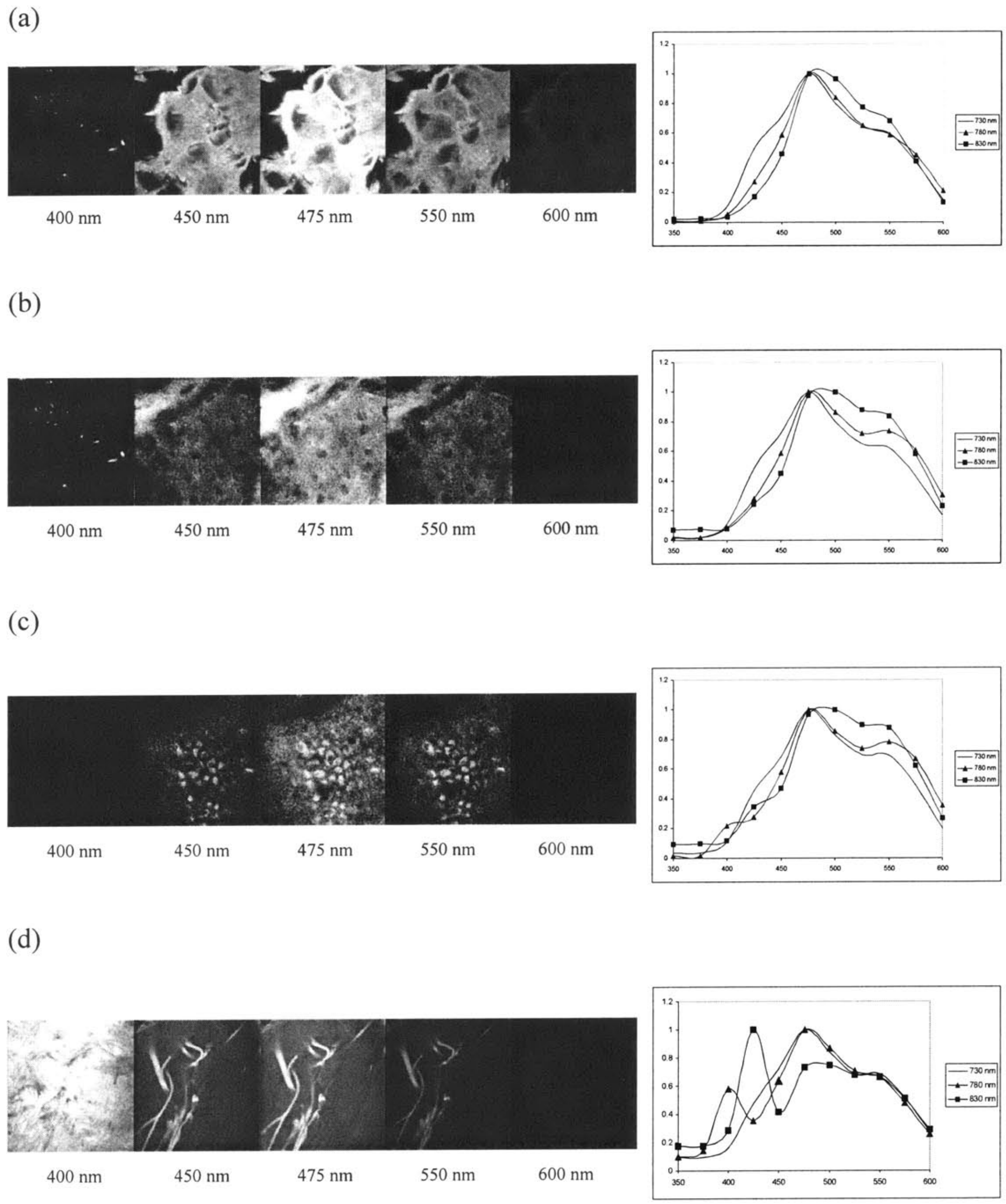

Figure 5.3. Two-photon images of various skin layers obtained after excitation at 780 nm and observed through different emission filters. The emission spectra of each layer for different excitation wavelength are also shown (a) stratum corneum, (b) stratum spinosum, (c) basal layer, and (d) dermis. Each layer is excited at three different excitation wavelengths: 730 (——), 780 (—▲—), and 830 (—■—) nm.

To better isolate the spectral contribution from dermal components without epidermal contribution, we further imaged and measured the emission spectrum from the deep dermal layer in surgically exposed skin. Emission spectrum in the deep dermis has two emission peaks at 400 and 475 nm at 780 nm excitation. Using feature resolved analysis, we found that these emission peaks correspond to two morphologically distinct structures. Figure 5.4 presents a three-dimensional reconstruction of these structures with distinct spectra. The structure with a 400 nm emission maximum has a fine-mesh morphology whereas the structure with a 475 nm emission maximum has the morphology of thick fibers. We further studied the spectrum with the emission peak at 475 nm. In the epidermis, a spectral component with emission maxima at 475 nm was also observed. Figure 5.5 shows that the spectral shapes are very different between the dermal and the epidermal components although both components have emission maximum close to 475 nm; we can conclude that different biochemical species are responsible for these emissions.

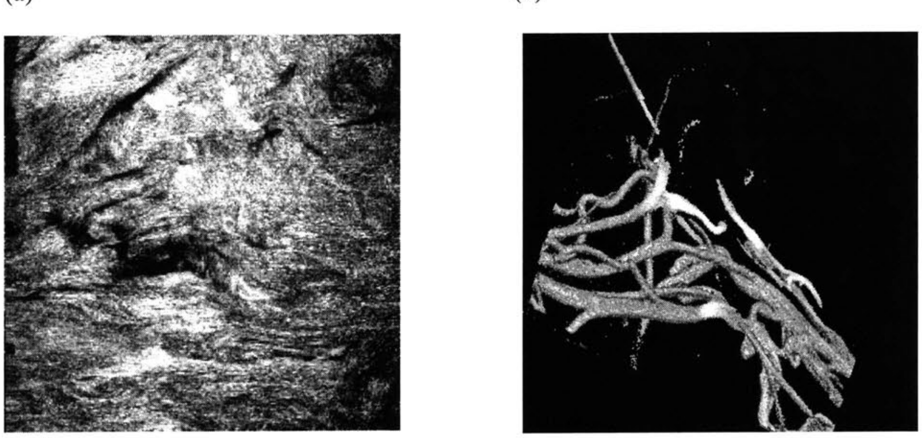

Figure 5.4. Dermis 3-D reconstruction at emission wavelengths of (a) 400 nm (b) 475 nm.

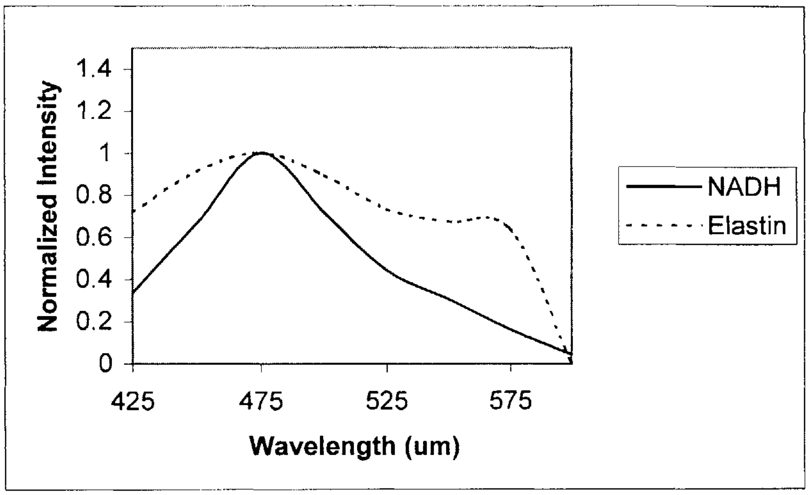

Figure 5.5. Emission spectra based on feature based segmentation. The NADH spectrum is obtained from the cytosol region of cells in the epidermal layers. The elastin spectrum is obtained from the thick fibers in the dermis layers. Both spectra are obtained with 780 nm excitation.

To better understand the biochemical species responsible for the luminescence in the dermis, we applied time-correlation single photon counting method to analyze the lifetimes of luminescence species in ex vivo surgically exposed dermis. Panel A of Figure 5.6 shows the sum of the photon counts collected using lifetime-resolved imaging. As can be seen in graph B and C of the same figure, each pixel of the image contains the fluorescence decay information collected in this pixel. These two graphs contain five decay curves representative of the areas highlighted on panel A.

The lifetime image has been fitted using the following equation, where I_i is the intensity as a function of time in pixel i and G(t) the Gaussian instrument response:

$$I_i(t) = \int_0^t G(t-T)\cdot c_{2i+1}\left(c_{2i+2}\exp\left(-\frac{T}{c_1}\right) + (1-c_{2i+2})\exp\left(-\frac{T}{c_2}\right)\right)dT$$

The coefficients c_1 and c_2 are the two time constants extracted from the image and were obtained as 47 ps and 2.6 ns. The coefficient c_{2i+1} represents the initial intensity in each pixel i while c_{2i+2} corresponds to the ratio of the two decays in this same pixel. Panel A in Figure 5.7 is a map of the value of these coefficient c_{2i+2} obtained from the global curve fitting. Panel B shows four decay curves with their corresponding fits. The insert shows the residuals (difference between fitting curve and experimental data) for those four curves. The largest error on the fits is on the order of ten percent and occurs around the time of the excitation. The use of an experimentally recorded instrument response might help to better fit the very fast growth and decay of the signal. Panel C is a complete map of the sum of the absolute value of the residuals normalized by the total intensity in each pixel. The absence of structure in this image shows that the optimization is successful both in regions of high or low autofluorescence.

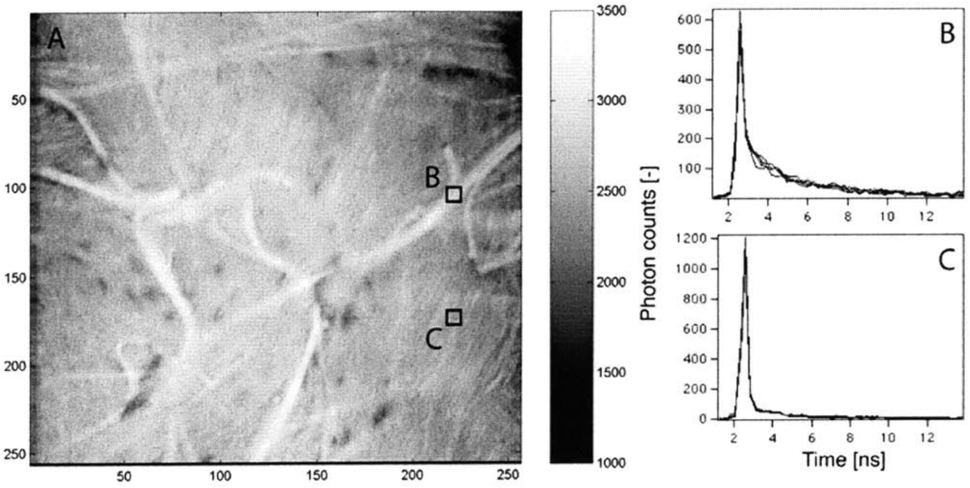

Figure 5.6. SHG and fluorescence decay collected by time correlated single photon counting. Panel A shows the total number of photon counts collected in each pixel, while panel B and C show five typical emission decays from the regions highlighted in panel A.

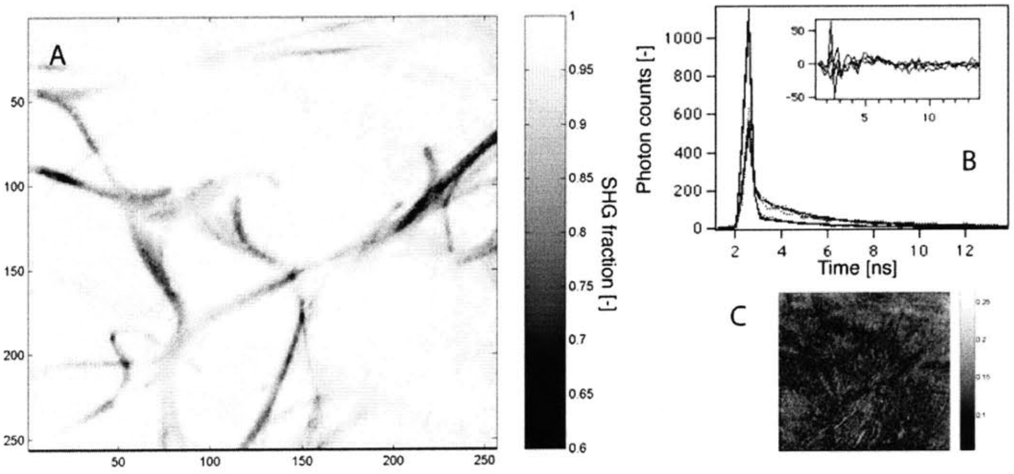

Figure 5.7. Panel A shows the ratio of SHG emission versus autofluorescence obtained by global fitting of the lifetime image. Panel B shows four experimental decays (dotted lines) and their corresponding fits (solid lines). Panel C is the image of the sum of the residuals.

5.2.3. Discussion

The bulk spectrum obtained in this experiment can be evaluated as either "weighted" or "non-weighted." In principle, the "weighted" method is more similar to traditional tissue spectroscopy in which the spectrum is modified by both the tissue scattering and absorption of the excitation light and the emission light resulting in giving the spectroscopic features from the surface of the tissue a greater contribution. The degree of weighting depends on tissue type, locale, and morphology and is, in general, not very well quantified. In contrast, the "non-weighted" method weighs the contribution from each depth more equally and can provide a better estimate of the true emission spectrum. The difference between these two methods can be seen by comparing Figures 5.2(a) and (b). We found that the weighted and non-weighted measurement is not greatly different for human skin down to 150 μm. The main observable difference is that the contribution of the fluorophore emitting at 550 nm is greater in the "non-weighted" versus the "weighted" method.

It is apparent that the interpretation of the bulk spectrum is difficult, and it is nearly impossible to identify all the chemical components present within the skin or determine their concentration. To extract that information, a layer segmentation was more successful. We were able to determine the biochemical factors that contribute to most of the autofluorescence that we see in skin. This was accomplished by analyzing the emission spectra of the different layers within the skin. The four different layers each have peaks at 475 nm and 550 nm. The 475 nm peak corresponds to known NAD(P)H emission spectra[120], and NAD(P)H is known to be present in cells and therefore is present in the top three layers.

The 550 nm peak is associated to the presence of melanin in the tissue. The peak at 550 nm is seen to be increasing as a function of depth, with the highest normalized intensity occurring within the basal layer. The increase in peak intensity as we move from the stratum corneum into the basal layer is as expected for melanin. In addition, comparison of the ratio of the peaks at 475 to 550 nm shows that the relative concentrations of the melanin are increasing as compared to NAD(P)H as we move deeper into the skin. This higher distribution of melanin in the deeper epidermal layer is also consistent with the observation that the 550 nm peak is more pronounced in the non-weighted bulk spectrum as compared with the weighted bulk spectrum.

In Figure 5.3(a) and (b), a shoulder can be seen at 425 nm. This feature only occurs within the epidermis and under excitation at 730 nm. The location of this fluorescent species is consistent with the distribution of tryptophan within the keratinocytes. Although tryptophan is typically excited at approximately 290 nm with one-photon[121,122], it is plausible that we may still pick up the tail end of the emission spectra of tryptophan. We only see a slight peak at 425 nm because our optics do not pass wavelengths below 350 nm.

Finally, we found the spectrum of the dermis to be quite interesting. There are two distinct peaks within this layer. The first peak is located at about 400 nm when excited at 780 nm and shifts to 425 nm when excited at 830 nm. There is a shift in the peak emission as the excitation wavelength shifts. Second harmonic generation is a non-linear process where two photons combine together to generate a new photon. The energy of the photon created is the sum of the energies of the incoming photons. In the present case, the observation that the emission wavelength is approximately at half of the laser frequency is consistent with the occurrence of SHG in the sample. The slight offsets of the SHG signals from the expected wavelengths are due to wavelength measurement uncertainty since relatively broad bandpass filters were used. Collagen is well known to produce SHG in biological sample[123] and is responsible for this signal in our emission spectra. The second emission peak at 475 nm is due to autofluorescence as indicated from the significantly broader spectral width. It is known from previous studies that both NAD(P)H and elastin emit into this band[120,9,124]. Therefore, the observed signal may arise from either cellular or extracellular matrix sources. To resolve this ambiguity, we performed a feature-based segmentation to better understand the emission spectra at 475 nm. A spectrum corresponding to regions of the thick fibers in the dermal layers was generated. For comparison, a second spectrum corresponding to keratinocyte cytosol in the epidermal layers was also produced; it is known that NAD(P)H is mostly responsible for the fluorescence in the cytosol. A comparison of the two spectrum was presented in Figure 5.5. These spectra indicate that the fluorescence emission from the fibers have a significantly broader spectral profile as compared with normal NAD(P)H emission. The broader spectrum indicates the presence of another fluorescent component in addition to NAD(P)H, and the spectral distribution is consistent with known elastin spectrum. It should be noted that while we have definitive evidence that elastin is responsible for a significant fraction of signal observed in these thick fibers, we cannot rule out that NAD(P)H fluorescence may partially contribute to the total signal.

We used lifetime resolved imaging to further support our identification of luminescence species in the dermis. Lifetime method further allows us to precisely determine the relative abundance of these species. The decay curve of the coarse fibrous structure observed in the intensity image of Figure 5.6 has a longer fluorescent lifetime (panel B) compared to the finer mesh background of the image, which shows a spike in the short fluorescence lifetime component but very limited long lifetime emission (panel C). The global fitting algorithm helps to further dissociate these two behaviors. The short lifetime of 47 ps (much shorter than the instrument response of 350 ps) is consistent with light arising from second harmonic generation, which is the signature of collagen in the sample. An independent control experiment further confirms that the scattered light intensity is negligible (data not shown).

The longer lifetime component of the emitted light measured is consistent with autofluorescence from elastin[125]. However, one should note that the limited photon counts collected from the autofluorescent and the presence of the strong peak due to SHG does not allow the resolution of the lifetimes of more than a single fluorescent species. Therefore, the fluorescent signal may originate from other endogenous fluorophores in addition to elastin.

The global fitting technique allows us to map the contribution from both components in the image. The distribution of SHG signal from collagen and autofluorescence signal from elastin corresponds well with the expected dermis structure as known from histology and from our emission wavelength data. It is also interesting to notice that the distribution of the SHG is dominant throughout the dermis contributing at least 60% of the total intensity. This indicates that the distribution of collagen is ubiquitous in dermis on the micron length scale. Elastin co-exists with collagen in coarse fibers with approximately equal intensity contributions.

5.2.4. Conclusions

We applied non-linear microscopic imaging and spectroscopy to study the biochemical identities of luminescence species and their distribution in ex vivo human skin. Since the distributions of chromophores in skin are not uniform and vary as a function of location, we applied morphologically guided spectral analysis method to resolve the constituent luminescence components associated with different skin morphological structures. By linking the spectroscopic information to tissue morphological structures, we successfully identified the luminescence components in human skin as summarized in Table 5.1. We found that morphologically guided spectral analysis is a very powerful general approach for tissue biochemical analysis with applications beyond dermatological studies.

Table 5.1

Peak Emission Wavelength (nm)	Excitation Wavelength (nm)		
	730	780	830
400		Collagen[#]	
425	Tryptophan		Collagen[#]
475	NADH	NADH/Elastin[&]	NADH/Elastin[&]
550	Melanin[*]	Melanin[*]	Melanin[*]

[*] Or biochemical component associated with melanin
[#] Due to second harmonics
[&] Elastin is located in the dermis

Table 5.1. Summary of autofluorescent components.

5.3. Photoaging on a skin equivalent model

5.3.1. Overview

In addition to the study of typical tissue physiology, two-photon spectral resolved microscopy can also be used to study tissue pathological processes. In this section, we focus on the use of two-photon spectral resolved microscopy to study photoaging. Photoaging refers to sun-induced premature aging of the skin. Damage to the skin is determined by the lifetime amount of radiation exposure and pigmentation of the person, and this process begins in ones youth. The chronic overexposure to the sun changes both the texture and elastic properties of the skin. The more noticeable changes include wrinkles, leathery-appearance, thickening of the epidermis, livers spots, precancerous lesions, and loss of elasticity. In addition, the collagen in the dermis breaks down at a higher rate than compared to normal aging. Photoaging can eventually lead to skin cancer; therefore, the prevention of photoaging is desirable.

Most of the changes due to photoaging are not evident until later on in life. It would be beneficial to develop a diagnosis method that is sensitive to the on-set of photoaging. We attempt to achieve this goal by using two-photon spectral resolved microscopy to monitor changes in skin morphology and spectroscopic signature upon UV exposure. In this study, the effects of erythema are studied. The erythema response is an acute inflammatory response of skin when exposed to solar radiation, and the effects of erythema begin to appear 3 to 4 hours after exposure and can last as many as 5 to 6 days depending on the intensity of the exposure[126]. Photoaging experiments are often carried out in animal models[127,128,129]. However, a promising alternative to study in animal models is the use of skin equivalent models. Skin equivalent model are tissue engineered constructed based on human keratinocytes and dermal fibroblasts cultured in collagen matrix. The use of dermal equivalent has the advantage that cellular and matrix components of the model are very well defined and are under molecular biological control. The main disadvantage of the use of dermal equivalent models for photoaging study is that many aspects of inflammatory responses that involve microcirculation changes and not be recapitulated.

5.3.2. Results and discussion

The skin equivalent models were exposed to either Dose 1 (10mJ/cm^2) or Dose 2 (40 mJ/cm^2) of UVB light. Dose 1 was chosen as it is not expected to induce significant erythema response while Dose 2 was chosen because the samples are expected to trigger a strong erythema response in animal models[130]. Figure 5.8 shows representative two-photon images of different layers in the skin equivalent model. These images are taken from a sample exposed to Dose 2 ten minutes after exposure. The layers represented are the stratum corneum, stratum spinosum, basal layer, and dermis. Below each image is its representative layer resolved spectrum obtained from the corresponding depth. These images show that skin equivalent model is similar morphologically to human skin. However, there is a notable difference in that this model does not contain melanin. Thus, the melanin caps that are typically found in ex vivo human skin are absent. In the layer resolved spectrum, there are only two peaks, one at 400 nm corresponding to second harmonic generation from collagen and a peak at 475 nm corresponding to NAD(P)H autofluorescence. The lack of melanin in this model explains the lack of a third peak in the spectrum normally located at 550 nm in ex vivo skin. It should be further noted that there appears to be a stronger second harmonic contribution in the epidermal layer as compared with ex vivo human skin that we have studied previously.

Within the epidermis and below the stratum corneum, layer resolved spectroscopy shows that the total intensity of the NAD(P)H signal is decreasing with respect to the collagen SHG signal with increasing depth. The relative intensity of the collagen peak is relatively constant across all the depths. Since tissue scattering coefficients for both collagen SHG signal and NAD(P)H signal is approximately the same, one may conclude that this decrease is due to a change in NAD(P)H intensity. NAD(P)H intensity may change due to either a change in the biochemical concentration or a change in cellular redox state. In general, more metabolically active cells with a stronger reduction potential are more fluorescent due to the presence of more fluorescent NAD(P)H vs. non-fluorescent NAD. Therefore, a consistent conclusion may be that the NAD(P)H autofluorescence is decreasing due to a decrease in cellular activity at increasing depth in the epidermis. This finding is very different from studies in human volunteers where significantly higher cellular activity is observed in the basal layer corresponding to higher metabolic activity[131]. This difference may be due to a lack of microcirculation in the dermal equivalent model.

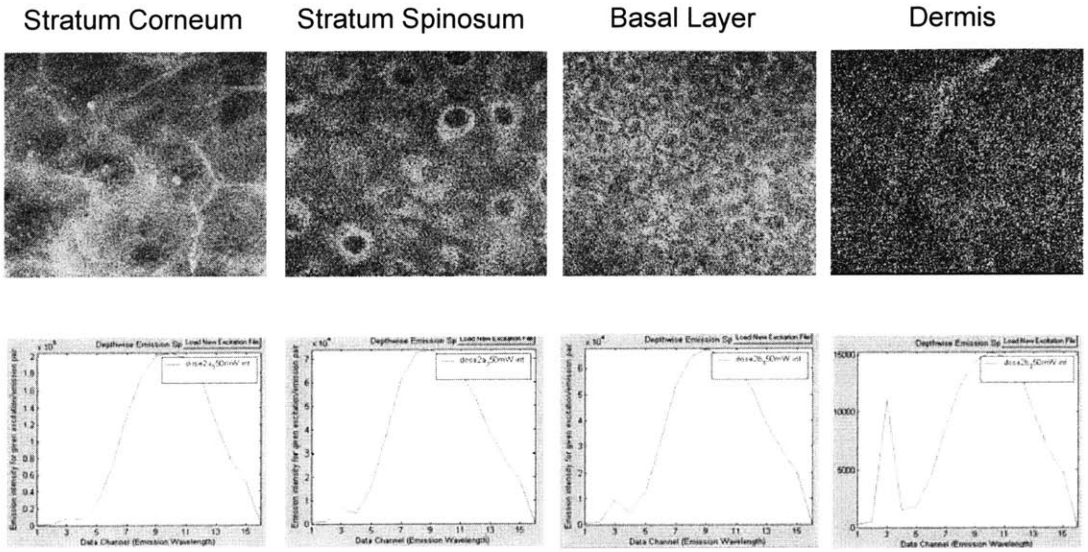

Figure 5.8. Representative images and layer resolved spectrum of stratum corneum, stratum spinosum, basal layer, and dermis.

We further examine the ratio of NAD(P)H fluorescence to collagen SHG as a function of depth at different time points after photo-exposure. The graph in Figure 5.9 compares the NADH-to-collagen ratio of samples exposed to Dose 2. The first sample was imaged at 10 minutes after exposure, the second at 24 hours after exposure, and the third at 48 hours after exposure. The same sample could not be imaged at the different time points due to sterility concerns, thus different samples for each time point were used. Examining the NADH-to-collagen ratio, the NAD(P)H/collagen ratio is maximized at the 24-hour post UV exposure. This temporal response is consistent with the typical time course of inflammatory response seen in animal models after UV exposure above the MED level. In animal models, the inflammatory response causes an increase in cellular metabolism. One may expect that this increase in metabolism results in an increase in NAD(P)H autofluorescence. At the 48-hour time point, there is a drop in the NAD(P)H-to-collagen ratio. This is consistent with previous work that has shown that the peak of the acute inflammatory response in skin exposed to UVB light declines after 24 hours[132,133].

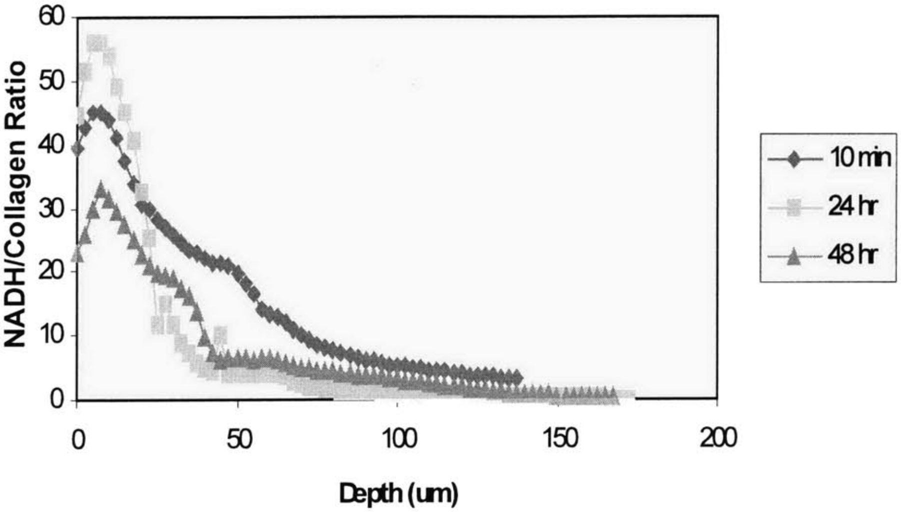

Figure 5.9. Time-dependent NADH/Collagen ratio of Dose 2 (40 mJ/cm2).

The NAD(P)H-to-collagen ratios of samples exposed to Dose 1 and Dose 2 are compared in Figure 5.10 at the 24-hour time point as a function of depth. We observe that the NAD(P)H-to-collagen ratio of Dose 2 is higher than that of Dose 1. This is not unexpected since Dose 1 is below the MED that does not cause inflammatory response in animal models and may not trigger enhanced cellular activity in the dermal equivalent model.

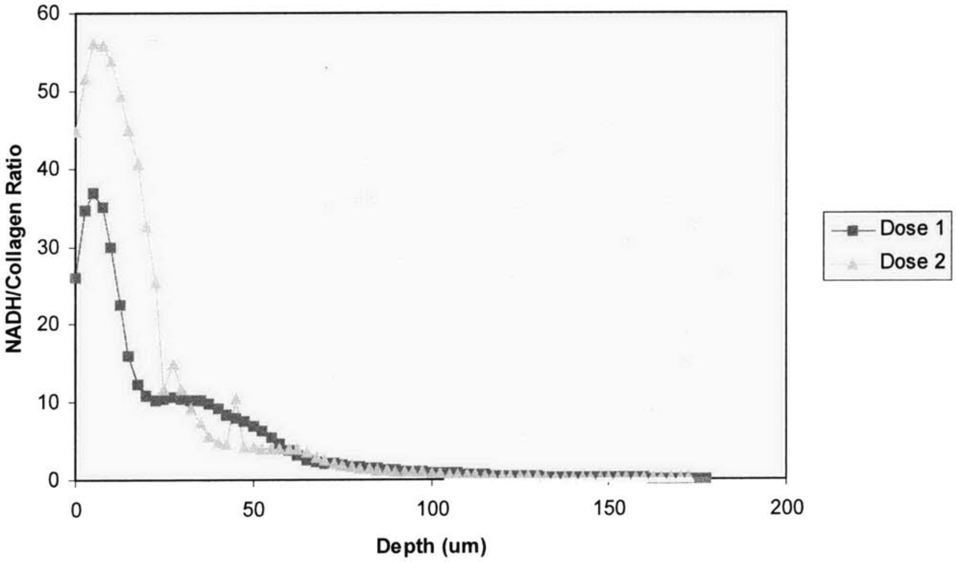

Figure 5.10. NADH/collagen ratio of Dose 1 and Dose 2 twenty-four hours after exposure.

The NAD(P)H-to-collagen ratios of samples exposed to Dose 1 and Dose 2 are compared in Figure 5.11 at the 48-hour time point as a function of depth. The NAD(P)H-to-collagen ratio is now slightly lower for the high dose than the lower dose. This is consistent with observation in animal models where inflammatory response is mostly completed by 48 hours.

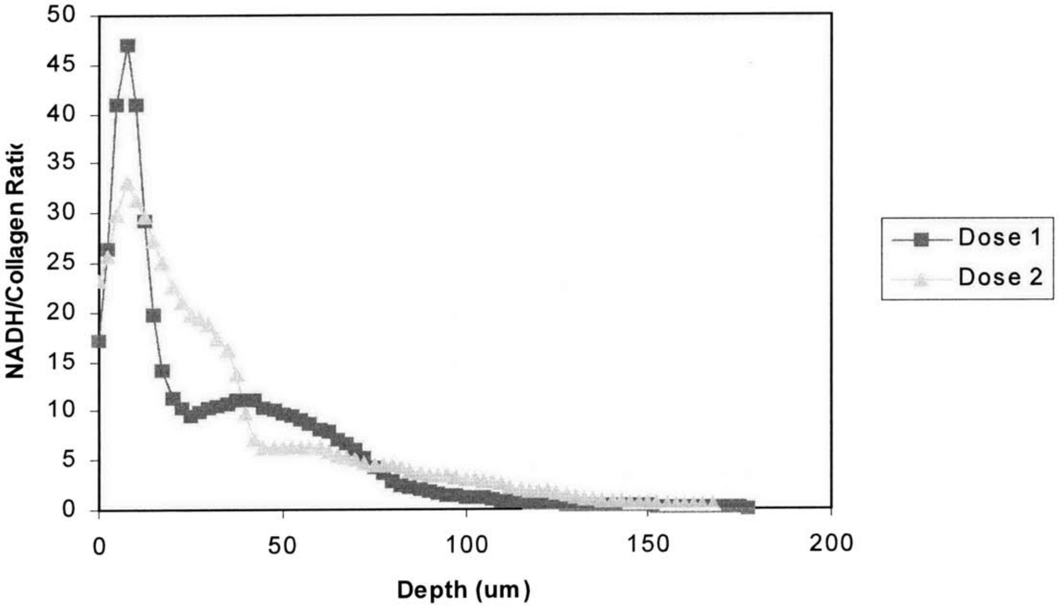

Figure 5.11. NADH/Collagen ratio of Dose 1 and Dose 2 forty-eight hours after exposure.

5.3.3. Conclusions

This experiment strongly suggests that NAD(P)H-to-collagen concentration can be detected using two-photon spectroscopy. Although we did not detect significant morphological changes in either the epidermis or the dermis, significant spectral change is observed. We found that NAD(P)H-to-collagen ratio significantly increases after 24 hours upon UVB exposure above MED. This result is consistent with acute inflammatory response observed in animal models. Further, this study can be benefit from data at longer time points post UV exposure. At longer time points, the effects of the degradation of collagen due to photoaging may be studied. In addition, it would be beneficial to image the same location in each sample at the various time points to decrease sample variability. This was not performed on this set of experiments due to issues of maintaining sample sterility, but an imaging chamber could be constructed to overcome this problem. Finally, this experiment is not intended as a comprehensive study of photoaging applied to skin equivalent models as only a single sample is obtained at each dose and time point. It is meant as a demonstration of the power of combining spectroscopic and morphological analysis. Definitive results require further experimentation. Nonetheless, this study demonstrates the sensitivity of two-photon spectral resolved microscopy in characterizing tissue states.

Chapter 6

Tri-modal microscopy results

6.1 Overview

A tri-modal microscope capable of combining two-photon fluorescence microscopy, second harmonic generation microscopy, and optical coherence microscopy has been constructed. The basics of these three imaging modalities have been discussed in Chapter 2, and the construction of this tri-modal instrumentation is described in Chapter 3.

We have performed the initial characterization and demonstration of this instrument. Three different sets of experiments were performed using the tri-modal microscope. The first experiment uses microspheres to demonstrate the ability of the instrumentation to combine two-photon fluorescence with OCM. The second experiment uses black tetra fish scale to demonstrate the ability of the microscope to combine second harmonic generation microscopy and OCM. The fish scale is a biological sample that is known to generate strong SHG signals. The third experiment combines all three modalities to study the dermis of ex vivo human skin.

The detection of the three different modalities was not performed simultaneously due to performance limitations of our analog-to-digital converter. Only two modalities could be imaged simultaneously. Because of this, OCM was always chosen to be one of the two modalities imaged in order to create a "constant" between the different data sets and to ensure proper registration of the sample.

6.2 Microspheres

To demonstrate the ability of the system to simultaneously obtain fluorescence and reflected light information from a sample, two different size fluorescent microspheres, 1 micron yellow-green fluorescent spheres and 2 micron blue spheres, were used. The microspheres were selected due to their strong fluorescent signal and that the spectral characteristics of the spheres were well known. As the microspheres do not exhibit SHG, this modality was not used in these experiments.

6.2.1. Results and discussion

In order to detect the fluorescence from the two different colored spheres, a dichroic (500dclp, Chroma, Brattleboro, VT) filter was placed in the detection path before the photomultiplier tubes. This filter reflects light below 500 nm and transmits light with a wavelength above 500 nm. Thus, the 400 nm fluorescence from the blue microspheres was reflected, and the 515 nm fluorescence from the yellow-green microspheres was transmitted. Bandpass filters were placed before the photomultiplier tubes to select the desired emission wavelength.

The first data set obtained contained both the reflected light and the fluorescence at 415 nm. The second data set contained the fluorescence at 515 nm and again the reflected light from the microspheres. Comparison of the two reflected light images establishes that the section of the sample being imaged in both data sets is identical.

Figure 6.1 shows the images obtained from this experiment. Three separate images can be seen – one of fluorescence at 515 nm using two-photon microscopy, one of reflected light using OCM, and one of fluorescence at 415 nm using two-photon microscopy. The images from each fluorescence channel can be overlaid with the OCM image. The OCM images shows all of the microspheres that are present in the imaging area while the fluorescence images shows all microspheres which fluoresce at each particular emission wavelength. These two images can then be combined to show the identification of all of the microspheres. It is clear from this image that all spheres are accounted for.

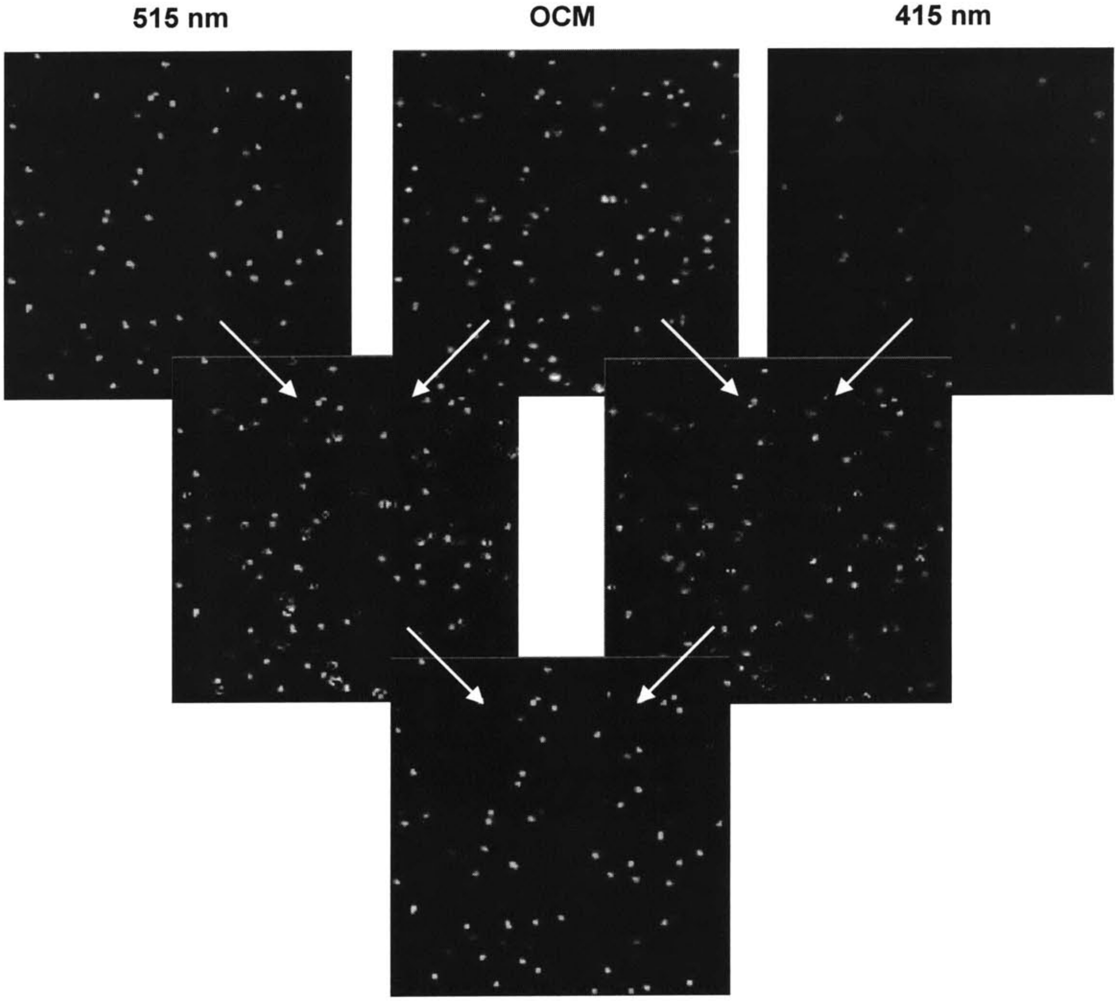

Figure 6.1. Fluorescent microspheres imaged using tri-modal microscope to visualize fluorescence at 415 and 515 nm and reflected light.

6.2.2. Summary

These experiments demonstrate that two-photon fluorescence and reflected light can be obtained simultaneously. Complementary information is obtained using these imaging modalities. From the reflected light images, we are able to determine the location and size of all microspheres; however, we are not able to determine the fluorescence identity of the microspheres. By combining the reflected light with the fluorescence images, this problem is overcome. This experiment further demonstrates the sensitivities of both fluorescence microscopy and OCM modalities in the detection of micron size objects.

6.3 Black tetra fish scale

Since the microsphere experiments did not demonstrate the ability of the tri-modal microscope to study second harmonic generation, a biological sample with known second harmonic generating structures was chosen to validate this modality. The scales from a black tetra fish are known to produce a strong SHG signal[134]. Fish scales are an essential part of the anatomy of a fish. The scales of a black tetra fish consist of two main regions. There is a rigid layer that is comprised primarily of calcium-based salts. There is also a fibrous layer that consists primarily of collagen.

6.3.1. Results and discussion

A section of black tetra fish scale was imaged using the tri-modal microscope system. Figure 6.2(a) shows the reflected light images, and Figure 6.2(b) shows the second harmonic generation images. There was no noticeable autofluorescence signal from this sample.

From Figure 6.2(a) we can see that there are there are primarily two types of structures present in these images. There are thicker more reflecting surfaces, and these thicker structures surround a thinner less reflective structure. From the reflected light image alone, it is not apparent what these two different structures are.

In Figure 6.2(b) we only see a single structure that produces SHG. Since it is known that collagen provides a strong SHG signal and that a large component of fish scale is collagen, we can ascertain that the structures seen in the SHG images are collagen. By overlaying the two images in Figure 6.3, we can visualize the overlap of the two structures. It appears that the thin structures in the reflected light image are collagen-rich region where as the thicker structures correspond to the rigid layer comprised of calcium-based salts.

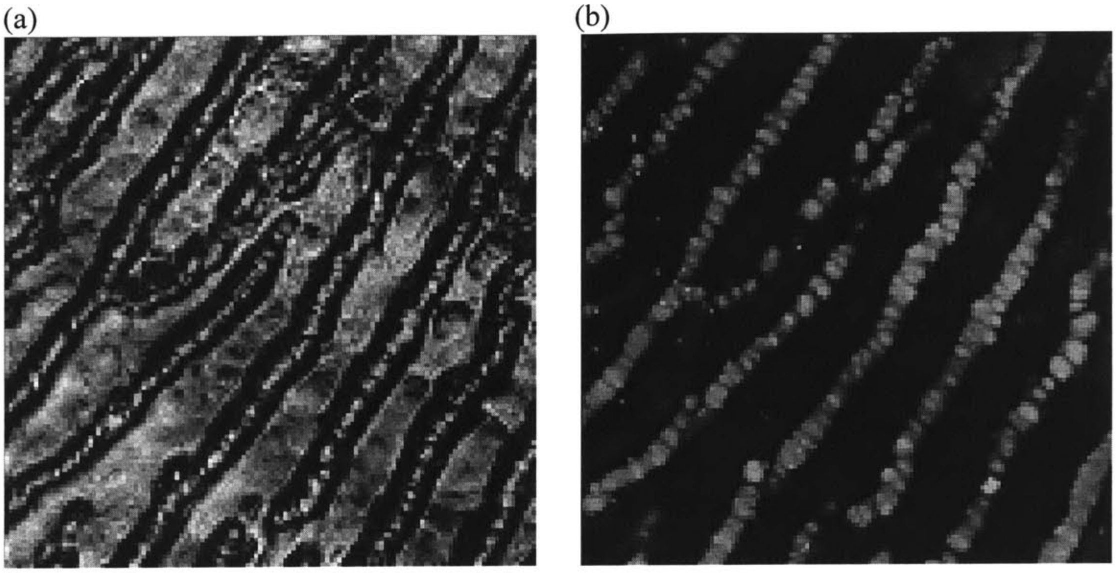

Figure 6.2. (a) Reflected light using OCM and (b) SHG using second harmonic generation microscopy images of fish scale from tri-modal microscope.

Figure 6.3. Overlaid images of reflected light and second harmonic generation images.

6.3.2. Summary

The combination of OCM and SHG clearly shows the power of these two complementary imaging techniques. OCM provides structural information whereas SHG allows the identification of crystalline, but non-fluorescent, objects such as collagen.

6.4. *Ex vivo human skin*

With the two previous experiments, only two different contrast mechanisms were imaged in each case. We further demonstrate the capability of this tri-modal microscope with a single biological specimen that is capable of generating fluorescence, SHG, and reflected light. The skin of ex vivo human skin is a sample that provides all three contrast mechanisms. There is fluorescence from NAD(P)H and elastin, SHG from collagen, and reflected light from morphological structures with different indices of refraction. .

6.4.1. Results and discussion

In order to detect the fluorescence and SHG, a 50/50 beam splitter (Newport Corporation, Irvine, CA) was placed in the detection path before the photomultiplier tubes. The SHG from collagen was detected by placing a 400 nm bandpass filter in front of the corresponding PMT, and the fluorescence from NADH and elastin was detected by placing a 475 nm bandpass filter in front of its corresponding PMT.

Figure 6.4 shows the results from this experiment on dermis of ex vivo human skin. Figure 6.4(a) shows the reflected light image, Figure 6.4(b) shows the second harmonic image, and Figure 6.4(c) shows the autofluorescence image. We see that there are two distinct structures that are present in the dermis corresponding to collagen and elastin rich regions. This is consistent with our results from the two-photon spectral resolved microscope.

Figure 6.5 shows the results from this experiment on the epidermis of ex vivo human skin. Figure 6.5(a) shows the reflected light image, and Figure 6.5(b) shows the autofluorescence image. We see that there are structures that correspond to NADH autofluorescence from cells. No SHG was detected in this section of the sample.

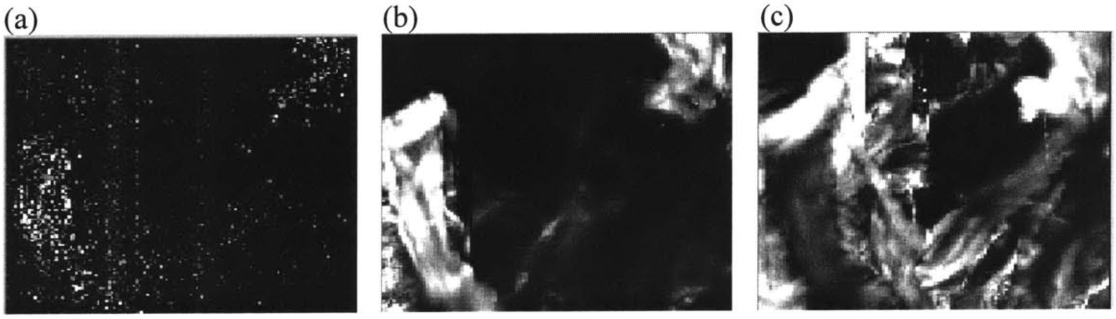

Figure 6.4. Tri-modal microscopy of dermis of ex vivo human skin using (a) reflected light, (b) second harmonic generation, and (c) autofluorescence.

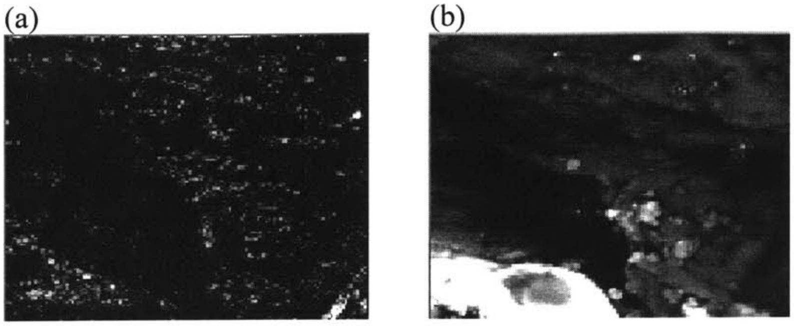

Figure 6.5. Tri-modal microscopy of epidermis of ex vivo human skin using (a) reflected light and (b) autofluorescence.

6.4.2. Summary

Validation of this imaging system was accomplished using ex vivo human skin. We demonstrate that structural differences between epidermis and dermis can be readily resolved based on the difference in the spectroscopic emission of the tissue constituents.

6.5. Conclusions

A series of experiments was performed to validate the different imaging methods used in this new tri-modal microscope. It has also been established that tri-modal microscopy can be used to provide complementary information about a specimen. This is the first demonstration of an instrument merging three different microscopic imaging techniques. By combining all of these three modalities, cross validation can be performed to better identify the biochemical components in the specimen. Many tissues have structures and biochemical composition that can be imaged based on these three contrast mechanisms. The tri-modal microscope will be a useful tool to better understand the physiology and pathology of these tissue systems.

Chapter 7

Interferometric second harmonic generation microscopy results

7.1. Overview

Strong second harmonic signal is found in the stroma of many tissues due to from the presence of collagen. Further, microtubule structures also produce SHG in cells and have been used to image mitotic spindle and neuronal processes[135,136]. A third theme of my thesis research is focused on the use of SHG for deeper imaging into tissues. In both the two-photon spectral resolved microscopy and the tri-modal microscopy, SHG signal is routinely detected. Realizing that the second harmonic signal is coherent, it is possible to develop a new instrument that can extend the imaging depth for collagen distribution based on coherent heterodyne detection techniques similar to optical coherence tomography. By measuring the time delay of second harmonic light that is generated from structures within the tissue, one can better determine the depth where this signal originates. This forms the basis for "time or coherence gating," well known in optical coherence microscopy, which allows better rejection of signals from tissue structures at different depths. Coherence gating should result in superior background reduction as compared with traditional non-linear optical microscopy such as two-photon imaging. This novel instrument further permits simultaneous detection of both reflected light and second harmonic generation signal that can provide complementary information related to tissue physiological states. Advantages of interferometric detection include an enhanced signal-to-noise ratio as compared to direct detection, which leads to an increase in the penetration depth. Phase sensitive detection can also be achieved with this system.

Chapter 3 details the construction of this instrumentation. This chapter describes experiments using a barium borate crystal to demonstrate interferometric coherent imaging with second harmonic signals in the epi-geometry. In addition, we show that polarization resolved imaging of coherent second harmonic signal might further provide crystalline orientation information.

7.2. Barium borate crystal (BBO) experiment

For the initial demonstration of interferometric second harmonic imaging, a sample with a strong SHG signal is used. A BBO crystal is known to generate strong SHG signal. The path lengths of both the ISHGM and OCM arms were adjusted to ensure that the focal point within the sample is the same in both arms.

The interference patterns generated by the BBO crystal for the ISHGM and OCM arms can be seen in Figure 7.1. The resolution of each arm is determined by the full-width-half-maximum of the interferogram. The resolution of the ISHGM arm is approximately 35 um while the resolution of the OCM arm is approximately 30 um. The non-symmetrical shape of the ISHGM interferogram is due to dispersion in the sample arm of the ISHGM section. This can be compensated for by placing dispersion compensating prisms in the beam path to create equal dispersion in each arm. The piezo mounted reference mirror was scanned a distance of 90 microns in order to capture the entire interferogram.

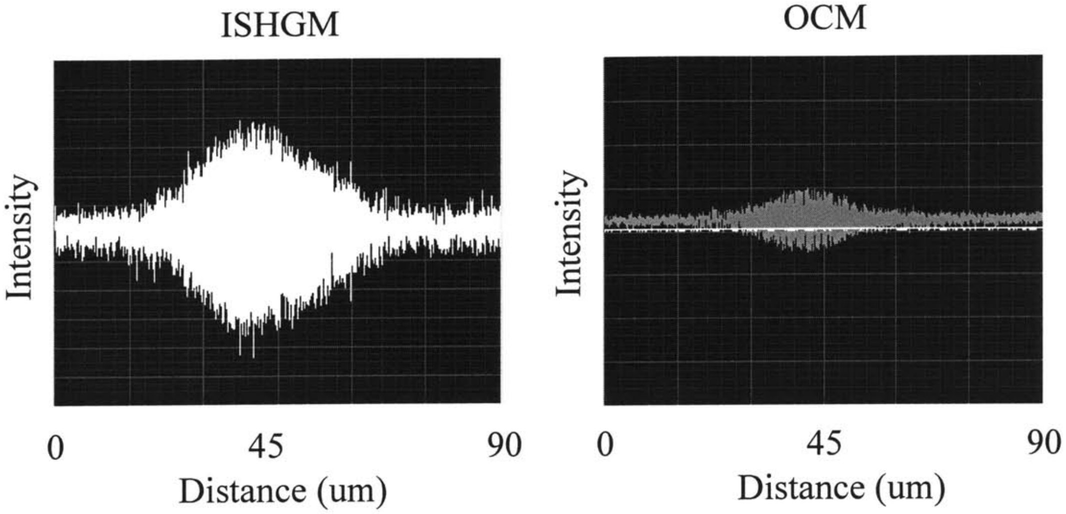

Figure 7.1. Interferogram from BBO crystal in ISHGM and OCM arms.

BBO crystal particles were further used as a sample to demonstrate the imaging capability of this system. A 100 um x 100 um area was imaged. The ISHGM arm measures second harmonic generation interferometrically while the OCM arm measures the reflected light interferometrically. The intensity at each pixel is determined by the average amplitude of a 5 um scan of the reference mirror and is demodulated at the heterodyne frequency. The ISHGM and OCM images are obtained simultaneously.

Figure 7.2 shows the (a) OCM and (b) ISHGM images from the BBO particles. As evident in Figure 7.2(a), there are a number of different sized particles in the sample. In Figure 7.2(b) most of these particles are not observed. The observation of signal in the OCM channel requires reflected light to be phase matched with the reference arm. The image observed in Figure 7.2(b) corresponds to the portion of second harmonic generation signal that is in phase with the reference arm.

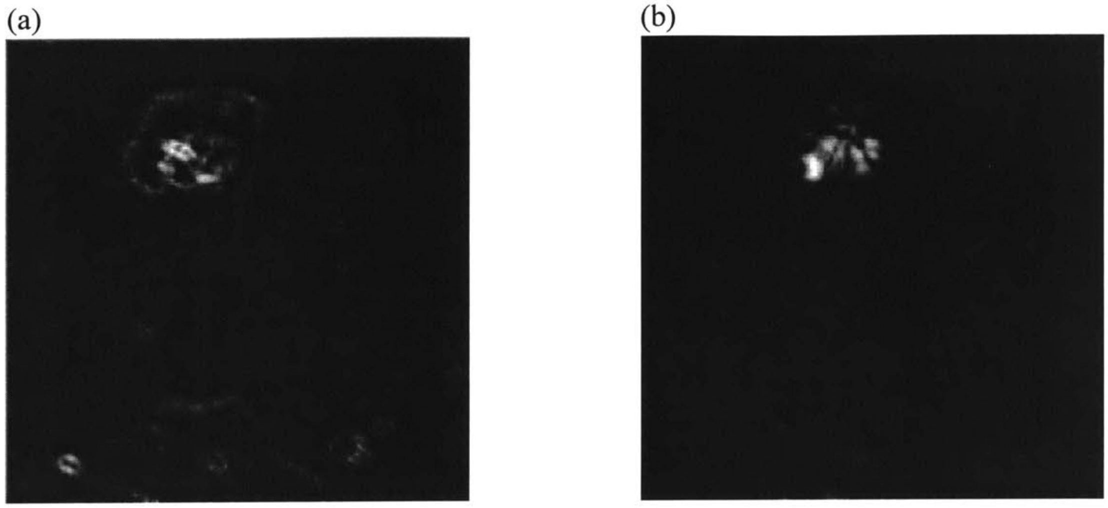

Figure 7.2. (a) OCM and (b) ISHGM images of BBO crystal particles

The sensitivity of the ISHGM system to phase matching gives rise to the possibility of polarization resolved imaging of coherent second harmonic signal. This can be implemented by creating in the reference arm a polarization state that is both parallel and perpendicular to the incident wave. This is accomplished by placing a half-waveplate in the reference arm to control the polarization state. The waveplate can be rotated to adjust the polarization to be either parallel or perpendicular to the incident wave.

Figure 7.3 shows the result from each of the orthogonal polarizations. Figure 7.3(a) shows the image when the reference arm polarization is perpendicular to the incident wave, and Figure 7.3(b) shows the image when the reference arm polarization is parallel to the incident wave. By comparing Figures 7.3(a) and (b), we see that the amplitude of corresponding pixels in the images vary across the crystal. These differences are due to microscopic variations of the orientations of the crystal domains.

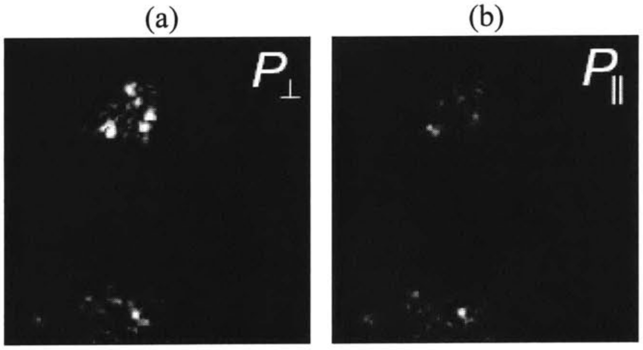

Figure 7.3. ISHGM images of BBO crystal particles with reference arm polarization states (a) perpendicular to the incident beam and (b) parallel to the incident beam.

7.3. Conclusions

A new multi-modal microscope has been developed to detect coherent signals using interferometric second harmonic generation microscopy with optical coherence microscopy. A future improvement of this system for polarization sensitive imaging involves the implementation of two independent photodetectors and a polarizing beamsplitter to detect signals from both polarization states simultaneously. Unfortunately, the current system is not able to image biological samples due to low epi-detected coherent SHG signal. Future experiments combining the coherent detection of both forward and epi-SHG signal may allow a better understanding of the origin of the low signal strength in the epi-mode. If one can successfully develop an instrument capable of detecting interferometric SHG signal in highly scattering biological specimen, one may investigate the possibility that coherent detection can allow deeper imaging into tissue specimens.

Chapter 8

Conclusion

The goal of my thesis was to develop new technologies for non-invasive optical biopsy. Three new instruments were constructed based on novel contrast mechanisms for tissue microscopic imaging and spectroscopy. The development of these instruments was detailed in Chapter 3. We created three new systems: a two-photon spectral resolved microscope, a tri-modal microscope incorporating two-photon fluorescence, second harmonic generation, and reflected light mechanisms, and an interferometric second harmonic generation microscope.

The two-photon spectral resolved microscope was applied to three different systems, as described in Chapter 5. Using both image guided spectral analysis and multivariate curve resolution, this research was able to identify autofluorescent components in ex vivo human skin based on excitation and emission spectra. The autofluorescent species identified are tryptophan, NAD(P)H, melanin, and elastin, and a collagen matrix that contributes to a second harmonic signal. The two-photon spectral resolved microscopy and the spectra recognition algorithms based on multivariate curve resolution and image guided spectral analysis methodologies should find applications in many tissues beyond the dermal system. Further, the spectral analysis algorithm developed is not limited to two-photon spectroscopy data and can be applied to other contrast mechanisms such as SHG or Raman signals.

We further demonstrated the use of the two-photon spectral resolved microscopy in the study of photoaging in a skin equivalent construct. Photoaging is becoming a more prevalent condition in the population and can lead to an increased instance of skin cancer. Changes due to photoaging are usually detected clinically by visual inspection, which is well beyond the onset of photoaging. Developing the ability to detect and treat photoaging earlier on would be an important advancement in the prevention of skin cancer. By better understanding the photoaging pathways, one can better determine strategies for alleviating photoaging conditions. Preliminary efforts in the study of photoaging have been promising. Preliminary data indicates that we can observe changes in epidermal cellular metabolic change upon high dose UVB exposure. The time course of metabolic change is consistent with the timing of inflammatory response observed in animal models.

We further performed preliminary experiments to demonstrate the capabilities and limitations of tri-modal microscopy and of interferometric second harmonic generation microscopy. The power of using complementary modalities to identify tissue structures based on their spectroscopic signatures is well demonstrated with the tri-modal instrument. Interferometric imaging using SHG has been demonstrated in solid state specimens but further research is needed to extend this technique for the imaging of biological specimen with significant multiple scattering.

In addition to photoaging, one of the most important future applications of technologies developed in my thesis may be in the distinction between healthy, precancerous, and cancerous tissues. Proliferation control of cancer cells is often compromised and cancer metastasis often starts with the encroachment upon the stroma by epidermal cancer cells with a concurrent degradation of the collagen matrix. With cellular proliferation, an increase in NAD(P)H fluorescence is expected. At the same time, collagen degradation should lead to a reduced second harmonic signal. The instrumentations that were developed in this thesis should allow for the simultaneous detection of NAD(P)H fluorescence and second harmonic generation from collagen. The quantification and ratio of each of these components to one another could lead to a powerful diagnostic tool for cancer diagnosis. In addition to photoaging and cancer diagnosis, we expect that these technologies can be applied to study the effect of irritants, drug delivery processes, and toxicology testing.

In conclusion, my thesis work has created new instrumentation that can be used by other researchers to better study and understand tissue. Once these techniques are fully developed, they can be use to characterize different pathological states of the tissue and hopefully in the future be used in conjunction with histology and other non-invasive tissue imaging modalities to improve health care procedures.

---

[1] William A Beresford, Lecture Notes On Histology, Blackwell Scientific Publishers: Oxford (1969).

[2] So, P.T.C, et. al., "Two-photon Excitation Fluorescence Microscopy," Annu. Rev. Biomed. Eng., Vol 2, pp. 399-429. 2000.

[3] Valeur, Bernard, Molecular Fluorescence: Principles and Applications, Wiley-Vch: Weinheim (2002), p. 354.

[4] A. M. K. Nilsson, D. Heinrich, J. Olajos, and S. Andersson-Engels, "Near infrared diffuse reflection and laser-induced fluorescence spectroscopy for myocardial tissue characterization," *Spectrochimica Acta Part A*, 53, 1901-1912 (1997).

[5] H. Zeng, C. MacAulay, D. I. McLean, and B. Palcic, "Spectroscopic and microscopic characteristics of human skin autofluorescence emission," *Photochemistry and Photobiology*, 61, 639-645 (1995).

[6] Palasz Z, Grobelny A, Pawlik E, Fraczek M, Zalesska-Krecicka M, Klimczak A, Krecicki T, "Investigation of normal and malignant laryngeal tissue by autofluorescence imaging technique, " Auris Nasus Larynx, 30 (4): 385-389 (2003).

[7] Drezek R, Sokolov K, Utzinger U, Boiko I, Malpica A, Follen M, Richards-Kortum R, "Understanding the contributions of NADH and collagen to cervical tissue fluorescence spectra: modeling, measurements, and implications," *Journal of Biomedical Optics*, 6 (4): 385-396 (2001).

[8] A. Mahadevan, M. F. Mitchell, E. Silve, S. Thomsen, and R. R. Richards-Kortum, ''Study of the fluorescence properties of normal and neoplastic human cervical tissue,'' *Lasers Surg. Med.* **13**, 647–665 (1993).

[9] N. Ramanujam, M. F. Mitchell, A. Mahadevan, S. Thomsen, A. Malpica, T. Wright, N. Atkinson, and R. Richards-Kortum, ''Development of a multivariate statistical algorithm to analyze human cervical tissue fluorescence spectra acquired in vivo,'' *Lasers Surg. Med.* **19**, 46–62 (1996).

[10] Leunig A, Mehlmann M, Betz C, Stepp H, Arbogast S, Grevers G, Baumgartner R, "Fluorescence staining of oral cancer using a topical application of 5-aminolevulinic acid: fluorescence microscopic studies," *Journal of Photochemistry and photobiology B-Biology*, 60 (1): 44-49 (2001).

[11] Ingrams DR, Dhingra JK, Roy K, Perrault DF, Bottrill ID, Kabani S, Rebeiz EE, Pankratov MM, Shapshay SM, Manoharan R, Itzkan I, Feld MS, "Autofluorescence characteristics of oral mucosa," *Head and Neck- Journal for the Sciences and Specialties of the Head and Neck*, 19 (1): 27-32 (1997).

---

[12] Atlamazoglou V, Yova D, Kavantzas N, Loukas S, "Microscopical examination of the localisation patterns of two novel rhodamine derivatives in normal and neoplastic colonic mucosa," *Lasers in Medical Science* 16 (4): 253-259 (2001).

[13] Georgakoudi I, Jacobson BC, Muller MG, Sheets EE, Badizadegan K, Carr-Locke DL, Crum CP, Boone CW, Dasari RR, Van Dam J, Feld MS, "NAD(P)H and collagen as in vivo quantitative fluorescent biomarkers of epithelial precancerous changes," *Cancer Research*, 62 (3): 682-687 (2002).

[14] Zeng HS, Petek M, Zorman MT, McWilliams A, Palcic B, Lam S, "Integrated endoscopy system for simultaneous imaging and spectroscopy for early lung cancer detection," *Optics Letters*, 29 (6): 587-589 (2004).

[15] Hewett J, McKechnie T, Sibbett W, "Fluorescence detection of superficial skin cancers," *Journal of Modern Optics*, 47 (11): 2021-2027 (2002).

[16] Schantz SP, Kolli V, Savage HE, Yu GP, Shah JP, Harris DE, Katz A, Alfano RR, Huvos AG, "In vivo native cellular fluorescence and histological characteristics of head and neck cancer," *Clinical Cancer Research*, 4 (5): 1177-1182 (1998).

[17] R. M. Cothren, R. Richards-Kortum, M. Sivak, M. Fitzmaurice, R. Rava, G. Boyce, M. Doxtader, R. Blackman, T. Ivanc, G. Hayes, M. S. Feld, and R. E. Petras, "Gastrointentinal tissue diagnostic by laser-induced fluorescence spectroscopy at endoscopy," *Gastrointest Endosc*, 36, 105-111 (1990).

[18] R. Richards-Kortum, R. P. Rava, M. Fitzmaurice, L. Tong, N.B. Ratliff, J. R. Kramer, and M. S. Feld, "A one-layer model of laser induced fluorescence for diagnosis of diseases in human tissue: application to human tissue," *IEEE Trans. Biomed. Eng.*, 36, 1222-1232 (1989).

[19] R. Richards-Kortum, R. P. Rava, R. E. Petras, M. Fitzmaurice, M. Sivak, and M. S. Feld, "Spectroscopic diagnosis of colonic dysplasia," *Photochem. Photobiol.*, 53, 777-786 (1991).

[20] R. Glasgold, M. Glasgold, H. Savage, J. Pinto, R. Alfano, and S. Schantz, "Tissue autofluorescence as an intermediate endpoint in NMBA-induced esophageal carcinogenesis," *Cancer Letters*, 82, 33-41 (1994).

[21] S. P. Schantz, H. E. Savage, P. Sacks, and R. R. Alfano, "Native cellular fluorescence and its application to cancer prevention," *Environmental Health Perspectives*, 105, 941-944 (1997).

[22] K. Licha, B. Riefke, V. Ntziachristos, A. Becker, B. Chance, and W. Semmler, "Hydrophilic cyanine dyes as contrast agents for near-infrared tumor imaging: Synthesis,

---

photophysical properties and spectroscopic in vivo characterization," *Photochemistry and Photobiology*, 72, 392-398 (2000).

[23] B. Beauvoit and B. Chance, "Time-resolved spectroscopy of mitochondria, cells, and tissues under normal and pathological conditions," *Molecular and Cellular Biochemistry*, 184, 445-455 (1998).

[24] N. Kollias, R, Gillies, M. Moran, I. E. Kochevar, and R. R. Anderson, "Endogenous skin fluorescence includes bands that may serve as quantitative markers of aging and photoaging," *Journal of Investigative Dermatology*, 111, 776-780 (1998).

[25] T. Wilson, *Confocal Microscopy* ~Academic, London, 1990.

[26] Muller MG, Valdez TA, Georgakoudi I, Backman V, Fuentes C, Kabani S, Laver N, Wang ZM, Boone CW, Dasari RR, Shapshay SM, Feld MS, "Spectroscopic detection and evaluation of morphologic and biochemical changes in early human oral carcinoma," *Cancer*, 97 (7): 1681-1692 (2003).

[27] Masters BR, "Reflected light confocal microscopy of human skin in vivo," *Scanning*, 21 (2): 133-134 (1999).

[28] Pavlova I, Sokolov K, Drezek R, Malpica A, Follen M, Richards-Kortum R, "Microanatomical and biochemical origins of normal and precancerous cervical autofluorescence using laser-scanning fluorescence confocal microscopy," *Photochemistry and Photobiology*, 77 (5): 550-555 (2003).

[29] Wang HW, Willis J, Canto MIF, Sivak MV, Izatt JA, "Quantitative laser scanning confocal autofluorescence microscopy of normal, premalignant, and malignant colonic tissues," *IEEE Transactions on Biomedical Engineering*, 46 (10): 1246-1252 (1999).

[30] Koenig F, Gonzalez S, White WM, Lein M, Rajadhyaksha M, "Near-infrared confocal laser scanning microscopy of bladder tissue in vivo," *Urology* 53 (4): 853-857 (1999).

[31] M. Goppert-Mayer, "Uber elementarakte mit zwei quantensprungen," Ann. Phy., 9, 273-294 (1931).

[32] W. Denk, J. H. Strickler, and W. W. Webb, "Two-photon laser scanning fluorescence microscopy," Science, 248, 73-76 (1990).

[33] Bhawalkar J.D., Kumar N.D., Zhao C.F., Prasad P.N., "Two-photon photodynamic therapy," *J. Clin. Laser Med. Surg.*, 15: 201-4 (1997).

[34] Fisher W.G., Partridge W.P., Jr., Dees C., Wachter E.A., "Simultaneous two-photon activation of type-I photodynamic therapy agents," *Photochemistry and Photobiology*, 66: 141-55 (1997).

---

[35] Masters B.R., So P.T.C., Gratton E., "Optical biopsy of in vivo human skin: multi-photon excitation microscopy," *Laser Med. Sci.*, 13: 196-203 (1998).

[36] Masters B.R., So P.T., Gratton E., "Multiphoton excitation fluorescence microscopy and spectroscopy of in vivo human skin," *Biophysical Journal*, 72: 2405-12 (1997).

[37] Malone JC, Hood AF, Conley T, Nurnberger J, Baldridge LA, Clendenon JL, Dunn KW, Phillips CL, "Three-dimensional imaging of human skin and mucosa by two-photon laser scanning microscopy," *Journal of Cutaneous Pathology*, 29 (8): 453-458 (2002).

[38] So P.T.C., Kim H., Kochevar I.E., "Two-photon deep tissue ex vivo imaging of mouse dermal and subcutaneous structures," *Optics Express*, 3: 339-50 (1998).

[39] Mizrahi A, Crowley JC, Shtoyerman E, Katz LC, "High-resolution in vivo imaging of hippocampal dendrites and spines," *Journal of Neuroscience*, 24 (13): 3147-3151 (2004).

[40] Mizrahi A, Katz LC, "Dendritic stability in the adult olfactory bulb," *Nature Neuroscience*, 6 (11): 1201-1207 (2003).

[41] Nitsch R, Pohl EE, Smorodchenko A, Infante-Duarte C, Aktas O, Zipp F, "Direct impact of T cells on neurons revealed by two-photon microscopy in living brain tissue," *Journal of Neuroscience*, 24 (10): 2458-2464 (2004).

[42] Denk W., Delaney K.R., Gelperin A., Kleinfeld D., Strowbridge B.W., Tank D. W., yuste R., "Anatomical and functional imaging of neurons using 2-photon laser scanning microscopy," *J. Neurosci. Nethods*, 54: 151-62 (1994).

[43] Svoboda K., Denk W., Kleinfeld D., Tank D.W., "In vivo dendritic calcium dynamics in neocortical pyramidal neurons," *Nature*, 385: 161-165 (1997).

[44] Oertner TG, "Functional imaging of single synapses in brain slices," *Experimental Physiology*, 87 (6): 733-736 (2002).

[45] Ruthazer ES, Cline HT, "Multiphoton imaging of neurons in living tissue: Acquisition and analysis of time-lapse morphological data," *Real-Time Imaging*, 8 (3): 175-188 (2002).

[46] Yeh AT, Kao BS, Jung WG, Chen ZP, Nelson JS, Tromberg BJ, "Imaging wound healing using optical coherence tomography and multiphoton microscopy in an in vitro skin-equivalent tissue model," *Journal of Biomedical Optics*, 9 (2): 248-253 (2004).

---

[47] Palmer GM, Keely PJ, Breslin TM, Ramanujam N, "Autofluorescence spectroscopy of normal and malignant human breast cell lines," *Photochemistry and Photobiology*, 78 (5): 462-469 (2003).

[48] Powers MJ, Domansky K, Kaazempur-Mofrad MR, Kalezi A, Capitano A, Upadhyaya A, Kurzawski P, Wack KE, Stolz DB, Kamm R, Griffith LG, "A microfabricated array bioreactor for perfused 3D liver culture," *Biotechnology and Bioengineering*, 78 (3): 257-269 (2002).

[49] Agarwal A, Coleno ML, Wallace VP, Wu WY, Sun CH, Tromberg BJ, George SC, "Two-photon laser scanning microscopy of epithelial cell-modulated collagen density in engineered human lung tissue," *Tissue Enginering*, 7 (2): 191-202 (2001).

[50] Squirrell JM, Wokosin DL, White JG, Bavister BD, "Long-term two-photon fluorescence imaging of mammalian embryos without compromising viability," *Nature Biotechnology*, 17 (8): 763-767 (1999).

[51] Boulnois, Las. Med. Sci. 1:47 (1986); Hale and Querry, Appl. Opt. 12:555 (1973).

[52] R. Na, I. M. Stender, L. Ma, and H. C. Wulf, "Autofluorescnce spectrum of skin: component bands and body site variations," *Skin Research and Technology*, 6, 112-117 (2000).

[53] H. Zeng, C. MacAulay, B. Palcic, and D. I. McLean, "A computerized autofluorescence and diffuse reflectance spectroanalyser system for *in vivo* skin studies," *Phys. Med. Biol.*, 38, 231-240 (1993).

[54] R. R. Alfano, D. Tata, J. Cordero, P. Tomashefsky, F. Longo, and M. Alfano, "Laser induced fluorescence spectroscopy from native cancerous and normal tissues," *Inst Electr Electron Eng J Quant Elect*, QE-20, 1507-1511 (1984).

[55] C. Y. Wang, C. T. Chen, C. P. Chiang, S. T. Young, S. N. Chow, and H. K. Chiang, "A probability-based multivariate statistical algorithm for autofluorescence spectroscopic identification of oral carcinogenesis," *Photochemistry and Photobiology*, 69(4), 471-477 (1999).

[56] H. Tsurui, H. Nishimura, S. Hattori, S. Hirose, and K. Okumura, "Seven-color fluorescence imaging of tissue samples based on Fourier spectroscopy and singular value decomposition," *J of Histochemistry and Cytochemistry*, 48(5), 653-662 (2000).

[57] A. J. Andrew and T. M. Hancewicz, "Rapid analysis of Raman image data using two-way multivariate curve resolution," *Applied Spectroscopy*, 52(6), 797-807 (1998).

[58] RLE Currents Volume 11, Number 2 (Fall 1999).

---

[59] Huang D., Swanson E.A., Lin C.P., Schuman J.S., Stinson W.G., Chang W., Hee M.R., Flotte T., Gregory K., Puliafito C.A., Fujimoto J.G. Optical coherence tomography, Science 254(5035): 1178-1181 (1991).

[60] Schmitt J.M., Yadlowsky M., Bonner R.F. Subsurface imaging in living skin with optical coherence tomography, Dermatology, 191: 93-98 (1995).

[61] Fujimoto J.G., Brezinski M.E., Tearney G.J., Boppart S.A., Bouma B.E., Hee M.R., Southern J.F., Swanson E.A. Optical biopsy and imaging using optical coherence tomography, Nature Medicine, 1: 970-972 (1995).

[62] Smiddy WE, Flynn HW, "Pathogenesis of macular holes and therapeutic implications," *American Journal of Ophthalmology*, 137 (3): 525-537 (2004).

[63] DiCarlo CD, Roach WP, Gagliano DA, Boppart SA, Hammer DX, Cox AB, Fujimoto JG, "Comparison of optical coherence tomography imaging of cataracts with histopathology," *Journal of Biomedical Optics*, 4 (4): 450-458 (1999).

[64] Hee MR, Puliafito CA, Duker JS, Reichel E, Coker JG, Wilkins JR, Schuman JS, Swanson EA, Fujimoto JG, "Topography of diabetic macular edema with optical coherence tomography," *Ophthalmology*, 105 (2): 360-370 (1998).

[65] Mok KH, Lee VWH, So KF, "Retinal nerve fiber loss in high- and normal-tension glaucoma by optical coherence tomography," *Optometry and Vision Science*, 81 (5): 369-372 (2004).

[66] Weinreb RN, Khaw PT, "Primary open-angle glaucoma," *Lancet*, 363 (9422): 1711-1720 (2004).

[67] Aydin A, Wollstein G, Price LL, Fujimoto JG, Schuman JS, "Optical coherence tomography assessment of retinal nerve fiber laver thickness changes after glaucoma surgery," *Ophthalmology*, 110 (8): 1506-1511 (2003).

[68] Pan YT, Farkas DL, "High-resolution imaging of living human skin with optical coherence tomography," *Scanning*, 21 (2): 134-135 (1999).

[69] Strasswimmer J, Pierce MC, Park BH, Neel V, de Boer JF, "Polarization-sensitive optical coherence tomography of invasive basal cell carcinoma," *Journal of Biomedical Optics*, 9 (2): 292-298 (2004).

[70] Welzel J, Reinhardt C, Lankenau E, Winter C, Wolff HH, "Changes in function and morphology of normal human skin: evaluation using optical coherence tomography," *British Journal of Dermatology*, 150 (2): 220-225 (2004).

---

[71] Pitris C, Jesser C, Boppart SA, Stamper D, Brezinski ME, Fujimoto JG, "Feasibility of optical coherence tomography for high-resolution imaging of human gastrointestinal tract malignancies," *Journal of Gastroenterology*, 35 (2): 87-92 (2000).

[72] Li XD, Boppart SA, Van Dam J, Mashimo H, Mutinga M, Drexler W, Klein M, Pitris C, Krinsky ML, Brezinski ME, Fujimoto JG, "Optical coherence tomography: Advanced technology for the endoscopic imaging of Barrett's esophagus," *Endoscopy*, 32 (12): 921-930 (2000).

[73] Pitris C, Saunders KT, Fujimoto JG, Brezinski ME, "High-resolution imaging of the middle ear with optical coherence tomography - A feasibility study," *Archives of Otolaryngology-Head and Neck Surgery*, 127 (6): 637-642 (2001).

[74] D'Amico AV, Weinstein M, Li XD, Richie JP, Fujimoto J, "Optical coherence tomography as a method for identifying benign and malignant microscopic structures in the prostate gland," *Urology*, 55 (5): 783-787 (2000).

[75] Yazdanfar S, Rollins AM, Izatt JA, "In vivo imaging of human retinal flow dynamics by color Doppler optical coherence tomography," *Archives of Ophthalmology*, 121 (2): 235-239 (2003).

[76] Boppart SA, Luo W, Marks DL, Singletary KW, "Optical coherence tomography: feasibility for basic research and image-guided surgery of breast cancer," *Breast Cancer Research and Treatment*, 84 (2): 85-97 (2004).

[77] Boppart SA, Bouma BE, Pitris C, Southern JF, Brezinski ME, Fujimoto JG, "Intraoperative assessment of microsurgery with three-dimensional optical coherence tomography," *Radiology*, 208 (1): 81-86 (1998).

[78] Pitris C, Goodman A, Boppart SA, Libus JJ, Fujimoto JG, Brezinski ME, "High-resolution imaging of gynecologic neoplasms using optical coherence tomography," *Obstetrics and Gynecology*, 93 (1): 135-139 (1999).

[79] Izatt et al., IEEE J. Sel. Top. Quant. Electron. 4, 1017-1028 (1996).

[80] Campagnola PJ, Loew LM, "Second-harmonic imaging microscopy for visualizing biomolecular arrays in cells, tissues and organisms," *Nature Biotechnology*, 21 (11): 1356-1360 (2003).

[81] Konig K, Riemann I, "High-resolution multiphoton tomography of human skin with subcellular spatial resolution and picosecond time resolution," *Journal of Biomedical Optics*, 8 (3): 432-439 (2003).

[82] Lin XS, Pan L, Hu JY, Ma H, Chen DY, "Backward second harmonic generation Imaging of tissues," *Progress in Biochemistry and Biophysics*, 31 (1): 83-88 (2004).

---

[83] Sun CK, Chen CC, Chu SW, Tsai TH, Chen YC, Lin BL, "Multiharmonic-generation biopsy of skin," *Optics Letters*, 28 (24): 2488-2490 (2003).

[84] Campagnola PJ, Millard AC, Terasaki M, Hoppe PE, Malone CJ, Mohler WA, "Three-dimensional high-resolution second-harmonic generation imaging of endogenous structural proteins in biological tissues" *Biophysical Journal*, 82 (1): 493-508 (2002).

[85] Campagnola PJ, Clark HA, Mohler WA, Lewis A, Loew LM, "Second-harmonic imaging microscopy of living cells," *Journal of Biomedical Optics*, 6 (3): 277-286 (2001).

[86] Freund I., Deutsch M, Sprecher A., "Connective tissue polarity. Optical second harmonic microscopy, crossed-beam summation, and small-angle scattering in rat tail tendon," *Biophysical Journal*, 50: 693-712 (1986).

[87] Yasui T, Tohno Y, Araki T, "Determination of collagen fiber orientation in human tissue by use of polarization measurement of molecular second-harmonic-generation light," *Applied Optics*, 43 (14): 2861-2867 (2004).

[88] Brown E, McKee T, diTomaso E, Pluen A, Seed B, Boucher Y, Jain RK, "Dynamic imaging of collagen and its modulation in tumors in vivo using second-harmonic generation," *Nature Medicine*, 9 (6): 796-800 (2003).

[89] Stoller P, Celliers PM, Reiser KM, Rubenchik AM, "Quantitative second-harmonic generation microscopy in collagen," *Applied Optics*, 42 (25): 5209-5219 (2003).

[90] Cox G, Kable E, Jones A, Fraser IK, Manconi F, Gorrell MD, "3-dimensional imaging of collagen using second harmonic generation," *Journal of Structural Biology*, 141 (1): 53-62 (2003).

[91] Moreaux L, Sandre O, Mertz J, "Membrane imaging by second-harmonic generation microscopy," *Journal of the Optical Society of America B-Optical Physics*, 17 (10): 1685-1694 (2000).

[92] Dombeck DA, Blanchard-Desce M, Webb WW, "Optical recording of action potentials with second-harmonic generation microscopy," *Journal of Neuroscience*, 24 (4): 999-1003 (2004).

[93] Pons T, Moreaux L, Mongin O, Blanchard-Desce M, Mertz J, "Mechanisms of membrane potential sensing with second-harmonic generation microscopy," *Journal of Biomedical Optics*, 8 (3): 428-431 (2003).

[94] Bechem M, Beutner S, Burkhardt N, Fuchs C, Kryschi C, Paffhausen W, Reiffers B, Schade A, Schlue WR, Schmid D, Schneider L, Schulte P, Wimmer T, Witzak D, Martin

---

HD, "Novel hyperpolarizable and fluorescent dyes in lipid membranes: studying membrane potentials using nonlinear optical and fluorescence," *Electrochimica Acta*, 48 (20-22): 3387-3393 (2003).

[95] Conboy JC, Kriech MA, "Measuring melittin binding to planar supported lipid bilayer by chiral second harmonic generation," *Analytica Chimica Acta*, 496 (1-2): 143-153 (2003).

[96] Christof Buehler, Ki H. Kim, Urs Greuter, Nick Schlumpf, and Peter T. C. So, "Single-Photon Counting Multi-Color Multi-Photon Fluorescence Microscope," *Journal of Fluorescence*, submitted.

[97] H. R. Morris, C. C. Hoyt, P. Miller, and P. J. Treado, (1996), Liquid crystal tunable filter Raman chemical imaging. *App. Spectrosc.* **50**(6), 805-811.

[98] E. S. Wachman, W. H. Niu, and D. L. Farkas, (1996), Imaging acousto-optic tunable filter with 0.35-micrometer spatial resolution. *App. Opt.* **35**(25), 5220-5226.

[99] Becker & Hickl GmbH, SPC-300 through SPC-730 Operating manual. www.becker-hickl.de.

[100] A. E. McKinnon, A. G. Szabo, and D. R. Miller, "The deconvolution of photoluminescence data," *J. Phys. Chem.*, 81, 1564-1570 (1977).

[101] P. J. Verveer, A. Squire, and P. I. H. Bastiaens, "Global analysis of fluorescence lifetime imaging microscopy data," *Biophys. J.*, 78, 2127-2137 (2000).

[102] S. Pelet and P. T. C. So, *in preparation.*

[103] Beaurepaire E, Moreaux L, Amblard F, Mertz J, "Combined scanning optical coherence and two-photon-excited fluorescence microscopy," *Optics Letters*, 24 (14): 969-971 (1999).

[104] Nikolenko V, Nemet B, Yuste R, "A two-photon and second-harmonic microscope," *Methods*, 30 (1): 3-15 (2003).

[105] Campagnola PJ, Millard AC, Terasaki M, Hoppe PE, Malone CJ, Mohler WA, "Three-dimensional high-resolution second-harmonic generation imaging of endogenous structural proteins in biological tissues," *Biophysical Journal*, 82 (1): 493-508 (2002).

[106] Zoumi A, Yeh A, Tromberg BJ, "Imaging cells and extracellular matrix in vivo by using second-harmonic generation and two-photon excited fluorescence," *Proceedings of the National Academy of Sciences of the United States of America*, 99 (17): 11014-11019 (2002).

---

[107] Zipfel WR, Williams RM, Christie R, Nikitin AY, Hyman BT, Webb WW, "Live tissue intrinsic emission microscopy using multiphoton-excited native fluorescence and second harmonic generation," *Proceedings of the National Academy of Sciecnes of the United States of America*, 100 (12): 7075-7080 (2003).

[108] Dunkers JP, Cicerone MT, Washburn NR, "Collinear optical coherence and confocal fluorescence microscopies for tissue engineering," *Optics Express*, 11 (23): 3074-3079 (2003).

[109] Work in preparation for thesis of Ki Hean Kim, MIT, Department of Mechanical Engineering.

[110] B. R. Masters, P. T. C. So, and E. Gratton, "Multiphoton excitation fluorescence microscopy and spectroscopy of in vivo human skin," *Biophysical Journal*, 72, 2405-2412 (1997).

[111] R. P. Haugland, *Handbook of Fluorescent Probes and Research Products, Ninth Edition*, Molecular Probes, Inc., Eugene, Oregon (2002).

[112] I. B. Berlman, *Handbook of Fluorescence Spectra of Aromatic Molecules*, Academic Press, New York (1971).

[113] Foster, J. "Sunburn," *emedicine.com, Inc.* (2004).

[114] Hewett J, McKechnie T, Sibbett W, Ferguson J, Clark C, Padgett M. Fluorescence detection of superficial skin cancers. *Journal of Modern Optics*, 47:2021-2027, 2000.

[115] N. Kollias, R, Gillies, M. Moran, I. E. Kochevar, and R. R. Anderson, "Endogenous skin fluorescence includes bands that may serve as quantitative markers of aging and photoaging," *Journal of Investigative Dermatology*, 111, 776-780 (1998).

[116] Masters BR, So PTC, Gratton E. Multiphoton excitation fluorescence microscopy and spectroscopy of in vivo human skin. *Biophysical Journal*, 72: 2405-2412, 1997.

[117] Rajadhyaksha M, Grossman M, Esterowitx D, Webb RH, Anderson RR. *In vivo* confocal scanning laser microscopy of human skin: melanin provides strong contrast. *J Invest Dermatol,* 104:946-952, 1995.

[118] Piston DW, Masters BR, Webb WW. Three-dimensionally resolved NAD(P)H cellular metabolic redox imaging of the *in situ* cornea with two-photon excitation laser scanning microscopy, *Journal of Microscopy* 178:20-27, 1994.

---

[119] Guo Y, Ho PP, Liu F, Wang QZ, Alfano RR. Noninvasive two-photon-excitation imaging of tryptophan distribution in highly scattering biological tissues. *Optics Communications*, 154: 383-389, 1998.

[120] B. Chance and B. Thorell. "Localization and kinetics of reduced pyridine nucleotide in living cells by microfluorometry," *J. Biol. Chem.*, 234, 3044-3050 (1959).

[121] S. Underfriend, *Fluorescence Assay in Biology and Medicine, Vol. 1.*, Academic Press, New York (1962).

[122] B. Brancaleon, G. Lin, and N. Kollias, "The in vivo fluorescence of tryptophan moieties in human skin increases with UV exposure and is a marker for epidermal proliferation," *J. of Investigative Dermatology*, 113, 977-982 (1999).

[123] E. Georgiou, T. Theodossiou, V. Hovhannisyan, K. Politopoulos, G. S. Rapti, and D. Yova, "Second and third optical harmonic generation in type I collagen, by nanosecond laser irradiation, over a broad spectral region," *Optics Communications*, 176, 253-260 (2000).

[124] K. Konig and I. Riemann, "High-resolution multiphoton tomography of human skin with subcellular spatial resolution and picosecond time resolution," *Journal of Biomedical Optics*, 8, 432-439 (2003).

[125] J. M. I. Maarek, L. Marcu, W. J. Snyder, and W. S. Grundfest, "Time resolved fluorescence spectra of arterial fluorescent compounds: reconstitution with the Laguerre expansion technique," *Photochem. Photobiol.*, 72, 78-187 (2000).

[126] Kligman LH & Kligman AM, "The nature of photoaging: Its prevention and repair," *Photodermatology,* 3: 215-217 (1986).

[127] Ichihashi M, Ueda M, Budiyanto A, Bito T, Oka M, Fukunaga M, Tsuru K, Horikawa T, "UV-induced skin damage," *Toxicology*, 189(1-2): 21-39 (2003).

[128] Yasui H and Sakurai H, "Age-dependent generation of reactive oxygen species in the skin of live hairless rats exposed to UVA light," *Experimental Dermatology*, 12(5): 655-661 (2003).

[129] Kligman LH, Crosby MJ, Kligman AM, "An animal model for assessing the effects of chemical peels on photoaged skin," *Journal of Dermatological Treatment*, 10(1): 37-45 (1999).

[130] Fourtanier A, Gueniche A., Compan D., Walker S.L., Young A.R. "Improved protection against solar-simulated radiation-induced immunosuppression by a sunscreen with enhanced ultraviolet A protection," *Journal of Investigative Dermatology,* 114(4): 620-627 (2000).

---

[131] Masters B.R., So P.T., Gratton E., "Multiphoton excitation fluorescence microscopy and spectroscopy of in vivo human skin," *Biophysical Journal*, 72: 2405-12 (1997).

[132] Sally H. Ibbotson and Peter M. Farr, "The Time-Course of Psoralen Ultraviolet A (PUVA) Erythema," *Journal of Investigative Dermatology*, 113(3): 346 – 349 (1999).

[133] Farr PM, Besag JE, Diffey BL: The time course of UVB and UVC erythema. *J Invest Dermatol* 91:454–457, 1988

[134] Campagnola PJ, Millard AC, Terasaki M, Hoppe PE, Malone CJ, Mohler WA, "Three-dimensional high-resolution second-harmonic generation imaging of endogenous structural proteins in biological tissues" *Biophysical Journal*, 82 (1): 493-508 (2002).

[135] Campagnola PJ, Millard AC, Terasaki M, Hoppe PE, Malone CJ, Mohler WA, "Three-dimensional high-resolution second-harmonic generation imaging of endogenous structural proteins in biological tissues," *Biophysical Journal*, 82(1): 493-508 (2002).

[136] Dombeck DA, Kasischke KA, Vishwasrao HD, Ingelsson M, Hyman BT, Webb WW, "Uniform polarity microtubule assemblies imaged in native brain tissue by second-harmonic generation microscopy," *Proceedings of the National Academy of Sciences of the United States of America,* 100(12): 7081-7086 (2003).